

NASA Contractor Report 172597

NASA-CR-172597
19850024029

Measurement and Analysis of Critical Crack Tip Processes During Fatigue Crack Growth

D. L. Davidson, S. J. Hudak, and R. J. Dexter
Southwest Research Institute
San Antonio, Texas

Contract NAS1-17641

June 1985

LIBRARY COPY

AUG 27 1985

LANGLEY RESEARCH CENTER
LIBRARY, NASA
HAMPTON, VIRGINIA



National Aeronautics and
Space Administration

Langley Research Center
Hampton, Virginia 23665

NASA Contractor Report 172597

Measurement and Analysis of Critical Crack Tip Processes During Fatigue Crack Growth

D. L. Davidson, S. J. Hudak, and R. J. Dexter
Southwest Research Institute
San Antonio, Texas

Contract NAS1-17641

June 1985



National Aeronautics and
Space Administration

Langley Research Center
Hampton, Virginia 23665

N85-32342 #

TABLE OF CONTENTS

		<u>Page</u>
1.0	INTRODUCTION	1
2.0	CRACK CLOSURE MEASUREMENTS FOR CONSTANT-AMPLITUDE FATIGUE CRACK GROWTH	3
2.1	Local Crack-Tip Opening Load as a Function of ΔK and K_{max}	3
2.2	Comparison of Compliance and Stereoimaging Measurements of Crack Opening Load	9
3.0	CRACK-TIP STRAIN AND STRESS FIELDS DURING CONSTANT- AMPLITUDE AND VARIABLE-AMPLITUDE FATIGUE CRACK GROWTH	13
3.1	Analysis of Experiment 1: $OLR^* = 2.15$, $ULR^* = 1$, $R = 0.16$, $\Delta K = 6.2 \text{ MN/m}^{3/2}$	13
3.2	Comparative Analysis of the Load Excursions	32
4.0	ANALYSIS OF SELECTED EXPERIMENTS WITH THE PLASTIC WAKE MODEL (FAST-2)	59
4.1	Influence of Crack Growth Rate Properties on Analytical Predictions	60
4.2	Influence of Constraint Factor on Analytical Predictions	67
4.3	Summary	73
5.0	DISCUSSION	77
6.0	CONCLUSIONS AND RECOMMENDATIONS	81
7.0	REFERENCES	85
	APPENDIX A - DEFINITION OF LOADING VARIABLES AND DELAY CYCLES FOR VARIABLE AMPLITUDE FATIGUE CRACK GROWTH	89
	APPENDIX B - ADDITIONAL ANALYTICAL RESULTS OBTAINED USING THE FAST-2 MODEL	95

LIST OF FIGURES

<u>Figure</u>		<u>Page</u>
1	Specimen Designs Used	4
2	Crack Opening Location Relative to the Crack Tip as Load P is Increased to P_O^I	5
3	Relation between Normalized Effective Stress Intensity Factor and K_{max} , as Determined from Local Measurements and Opening Load in Mode I	7
4	Comparison of Measured and Predicted Normalized Effective Crack-Tip Stress Intensity Ranges ($\Delta K_{eff}/\Delta K$) as a Function of Load Ratio (R) for Constant-Amplitude Fatigue Crack Growth	8
5	Comparison of the Opening Load to Maximum Load Ratio as Determined Remotely (Compliance) and Locally (Optical Microscopy with Stereoimaging) for (a) 2024 Panels Supplied by NASA, and (b) 7091	10
6	Definition of Loading Parameters and Summary of Sequences for which Residual Stresses were Determined	14
7	Crack Growth Rate and Effective Stress Intensity Factor Histories of the Three Load Excursions Analyzed Using Stereoimaging	15
8	Loading History for the Three load Excursions Analyzed	16
9	Displacements Caused by the Presence of the Crack	19
10	Mohrs Circles of Strain as Derived from the Displacements Shown in Figure 9	20
11	Displacements for the Cyclic Crack Just Prior to the Overload Cycle	21
12	Distribution of the Maximum Shear Strain for the Cyclic Crack Just Prior to the Overload Cycle	22
13	Displacements Caused by the Crack Being Loaded to Maximum Value during the Overload Cycle	23
14	Displacements Caused by the Unloading Portion of the Overload Cycle	24

LIST OF FIGURES (CONT.)

<u>Figure</u>		<u>Page</u>
15	Distribution of the Stresses Resulting from the Overload	26
16	Mohrs Circles of Stress for the Cyclic Crack Prior to the Overload	29
17	Cyclic Stresses as Determined from the Model and Extrapolated to Cover the Same Field as the Overload Cycle Analyses	30
18	Partitioning of the Cyclic Stress Range Prior to the Overload	31
19	The Residual Stress in the Direction of Loading which Resulted from Application of the Overload	33
20	The Residual Effective Stress Resulting from the Overload	34
21	A Cross Section Through the Residual Stress Field of Figure 19 Showing the Stresses Directly Ahead of the Crack Tip Caused by the Application of the Overload Cycle	35
22	Comparison of the Maximum Shear Strains Resulting from Each of the Overload Cycles Analyzed	36
23	Comparison of the Effective Strain at the Crack Tip Caused by the Overload Cycle with the Strain Caused by Monotonically Loading a Crack from $\Delta K = 5 \text{ MN/m}^{3/2}$	37
24	Overload Cycle Effective Strains Ahead of the Crack Tip, as Normalized by the Crack Tip Strain	38
25	Monotonic Loading Normalized Effective Strain Vs Adjusted Distance Parameter	40
26	Comparison of the Effective Strain Distributions Before and After the Overload Cycle for the Three Overloads Analyzed	41
27	Crack Tip Opening Displacement Compared with Crack Tip Effective Strain for Cyclic, Overload Cycle and Monotonic Loading	42

LIST OF FIGURES (CONT.)

<u>Figure</u>		<u>Page</u>
28	Correlation of Crack Tip Strain with Crack Growth Rate	45
29	(a) Stresses on the Loading Portion of the Overload Cycle and (b) on the Unloading Portion of the Overload Cycle in the Axis of the Load Application, $OLR^* = 2.15$	46
30	(a) Stresses on the Loading Portion of the Overload Cycle and (b) on the Unloading Portion of the Overload Cycle in the Axis of the Load Application, $OLR^* = 2.85$	47
31	(a) Stresses on the Loading Portion of the Overload Cycle and (b) on the Unloading Portion of the Overload Cycle	48
31	(c) Stresses on the Reloading Portion of the Underload Cycle and (d) on the Reloading Portion of the Underload Cycle	49
32	Residual Stress Field in the Direction of Loading Caused by the $OLR^* = 2.85$	50
33	Residual Stress Field in the Direction of Loading Caused by the $OLR^* = 3.0$	51
34	Residual Stress Field in the Direction of Loading Caused by the $OLR^* = 3.0$ Followed by the $ULR^* = 2.0$	52
35	Residual Stress Distribution within Half of the Crack Tip Plastic Zone for $OLR^* = 3.0$ and $R = 0.5$	53
36	Residual Effective Stress Field for $OLR^* = 2.85$	55
37	Residual Effective Stress Field for $OLR^* = 3.0$	56
38	Residual Effective Stress Field for $OLR^* = 3.0$ and $ULR^* = 2.0$	57
39	Comparison of Crack Growth Rate Curves Used in Analytical Predictions Versus Measured Crack Growth Rate Data on 7091-T7E69 from Several Extrusions and Load Ratios	61
40	Comparisons of Experimental Results and Model Predictions for Various Crack Growth Rate Curves	63

LIST OF FIGURES (CONT.)

<u>Figure</u>		<u>Page</u>
41	Comparison of Experimental Results and Model Predictions for Various Crack Growth Rate Curves	64
42	Comparison of Experimental Results and Model Predictions for Various Crack Growth Rate Curves	65
43	Comparison of Experimental Results and Model Predictions for Various Crack Growth Rate Curves	66
44	Comparison of Experimental Results and Model Predictions for Various Constraint Factors (α)	69
45	Comparison of Experimental Results and Model Predictions for Various Constraint Factors (α)	70
46	Comparison of Experimental Results and Model Predictions for Various Constraint Factors (α)	71
47	Comparison of Experimental Results and Model Predictions for Various Constraint Factors (α)	72
48	Comparison of Experimental Results and Model Predictions for Various Constraint Factors (α)	74
49	Comparison of Experimental Results and Model Predictions for Various Constraint Factors (α)	75

LIST OF TABLES

<u>Table</u>		<u>Page</u>
1	Labeling of Data Sets Analyzed	18
2	Equations for Normalized Strain Ahead of Crack Tip	43
3	Distance Ahead of Crack to Elastic Strain Boundary	43
4	Loading Variables for Experiments Analyzed with FAST-2	59

1.0 INTRODUCTION

This report summarizes work conducted over the past year designed to examine the mechanics of fatigue crack growth under constant-amplitude and variable-amplitude loading. In the latter case, critical loading histories involving relatively simple overload and overload/underload cycles were studied in order to provide a basic understanding of the underlying physical processes controlling crack growth. The material used for this study was 7091-T7E69, a powder metallurgy aluminum alloy. Extensive measurements of local crack-tip parameters have been made at various times before, during, and after the overloads--these include crack-tip opening loads and displacements, as well as crack-tip strain fields. The latter were used, in combination with the materials cyclic and monotonic stress-strain properties, to compute crack-tip residual stresses. The experimental results were also compared with analytical predictions obtained using the FAST-2 computer code. A study of the sensitivity of the analytical model to constant-amplitude fatigue crack growth rate properties and to through-thickness constraint was also conducted.

The report is organized into four main sections which are distinct but interrelated.

Section 2.0 presents crack closure measurements as a function of the applied ΔK and K_{max} , as well as a comparison of crack closure measurements obtained local to the crack tip using an optical stereoimaging technique and remote from the crack tip using an elastic compliance technique.

Section 3.0 contains a detailed determination of the residual stress-strain fields at crack tips resulting from overloads and overload/underloads. These results are used to establish a correlation between crack-tip strain and crack growth rate and to examine the issue of similitude by comparing stress-strain fields obtained before, during, and after the overloads.

Section 4.0 presents the sensitivity study of the FAST-2 computer model and compares analytical predictions with experimental results.

Section 5.0 provides a general discussion of results from the entire study, and Section 6.0 gives the resulting conclusions and recommendations.

Two appendices are provided for supplemental information. Appendix A gives the definitions of the terms used to characterize the overload and overload/underload events, as well as resulting crack growth retardation and delay phenomena. Appendix B provides a supplement to Section 5.0 by presenting additional details on the comparison of analytical and experimental results, as well as predictions of the crack-tip residual stresses from the FAST-2 analyses.

The work summarized in this report is an extension of that conducted under a previous NASA program [1].

2.0 CRACK CLOSURE MEASUREMENTS FOR CONSTANT-AMPLITUDE FATIGUE CRACK GROWTH

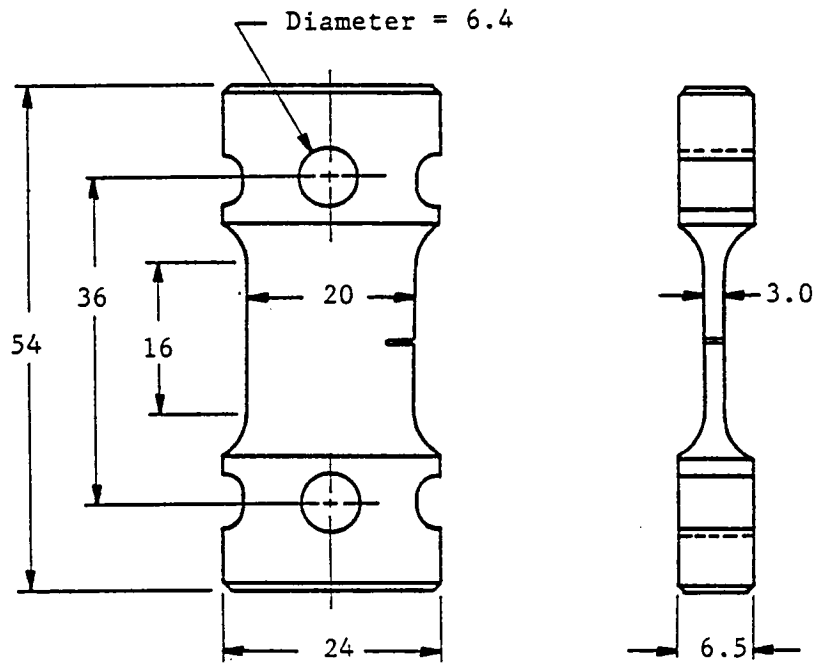
Extensive measurements have been made of the load at which a fatigue crack opens, for the powder metallurgy aluminum alloy 7091. These measurements were made on single-edge notched specimens, Figure 1, with the stereoimaging technique, using both an optical imaging system and a scanning electron microscope (SEM). Also, for the 2024 center-cracked panels supplied by NASA shown in Figure 1, measurements of crack opening load were made both locally and remotely. Locally, they were made using optical microscopy and stereoimaging; remotely, the compliance technique was used, and potential drop was attempted. Results from the various methods are compared.

2.1 Local Crack-Tip Opening Load as a Function of ΔK and K_{\max}

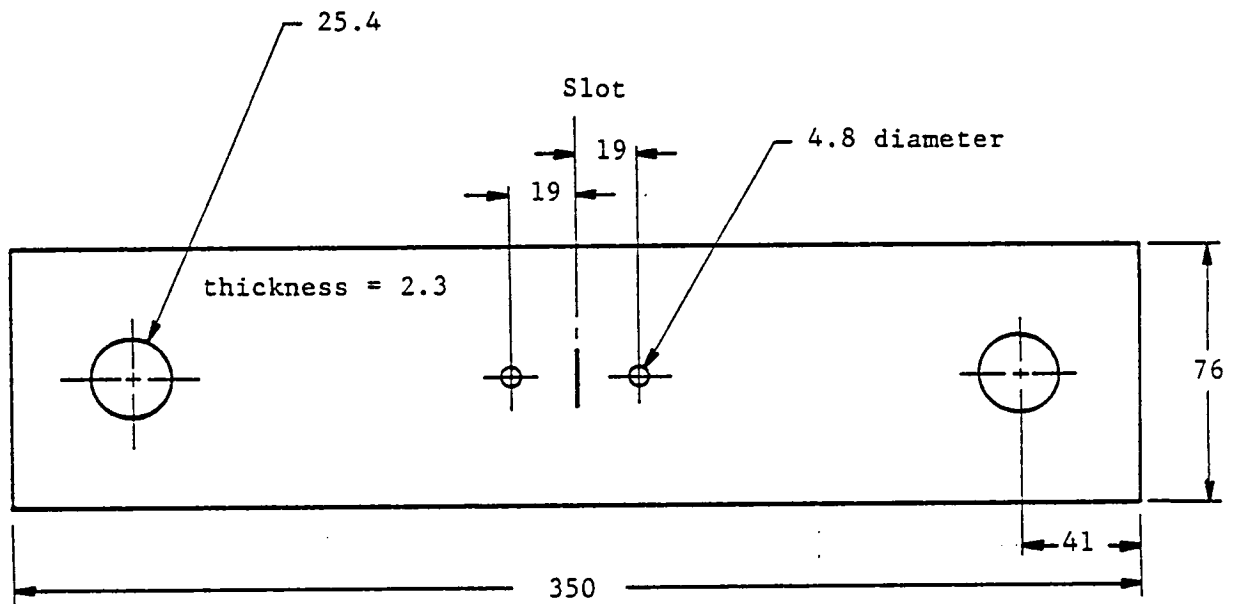
Crack opening load is determined using the stereoimaging technique by comparison in a stereoviewer of photographs made at successively-increasing loads with a photograph made at the minimum cyclic load. The viewing axis is that of Mode I; i.e., the eye axis is the same as the loading axis. Crack opening load in Mode II can also be determined by imaging the crack-tip region with the eye axis orthogonal to the loading axis. The latter procedure was used in a limited number of cases.

When observed in this way, the crack is seen to "peel open" with increasing load until it is open down to the crack tip. The load required to obtain complete opening of this crack to its tip in Mode I is termed P_0^I . The accuracy of this method of determining opening load is greater than its reproducibility from cycle to cycle. That is, if opening loads are measured carefully each 10-100 cycles at constant ΔK , variations in magnitude result; this observation is consistent with the previous findings of periodic variation in crack-tip opening displacements and strains as the crack propagates.

Typical findings of the variation in the length of the crack which remains closed with increasing applied load are shown in Figure 2. The



(a) 7091 aluminum alloy (Alcoa)



(b) 2024 aluminum alloy (NASA)

FIGURE 1. SPECIMEN DESIGNS USED. (a) Single edge notched design used for for both constant amplitude and spectrum loading using both scanning electron and optical microscopy. (b) Center notched panel for crack opening load measurement under constant amplitude loading as determined by stereoimaging and compliance. Dimensions in mm.

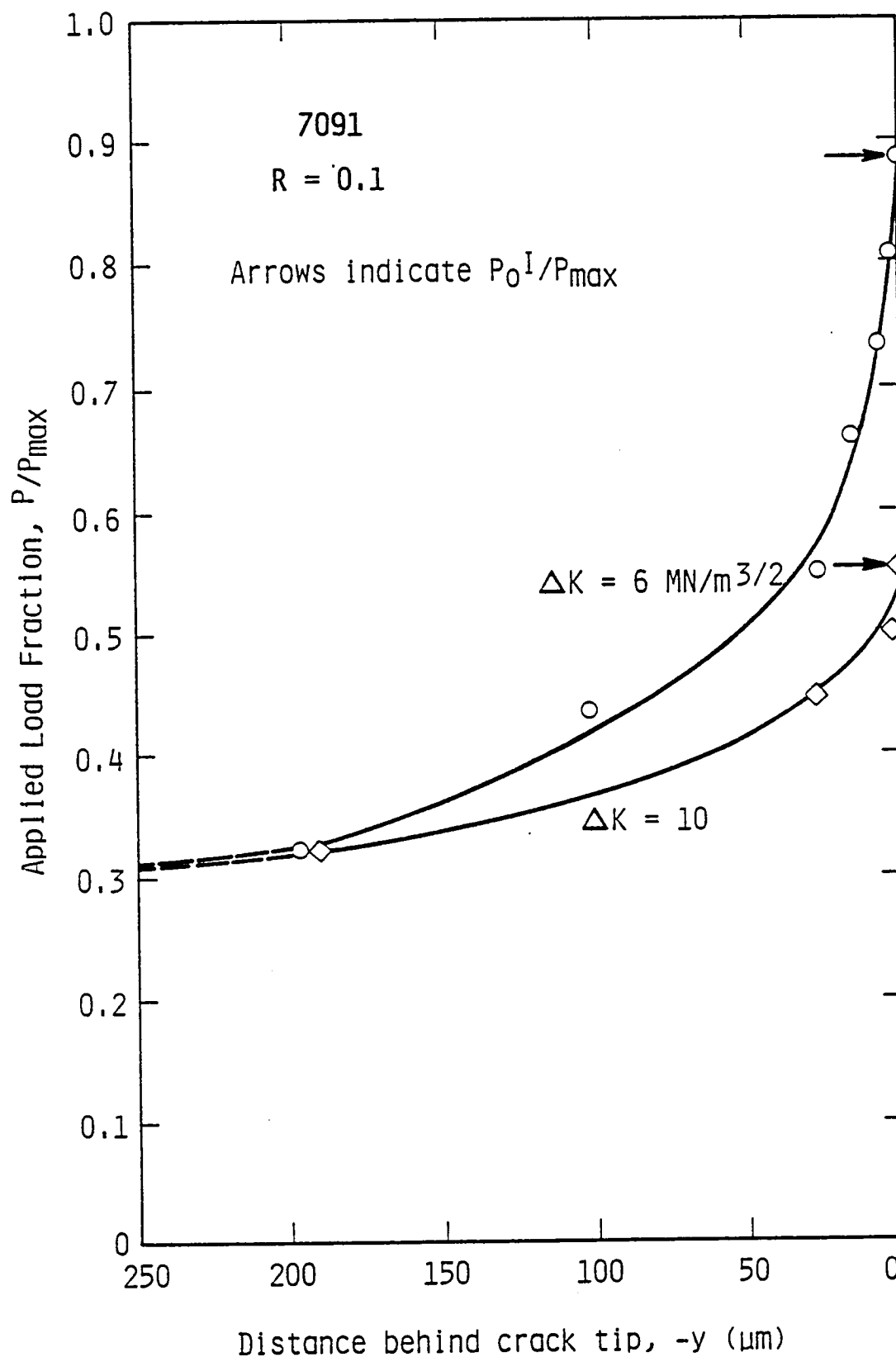


FIGURE 2. CRACK OPENING LOCATION RELATIVE TO THE CRACK TIP AS LOAD P IS INCREASED TO P_0^I , THE CRACK OPENING LOAD IN MODE I. Note the large change in load required to open the crack the last few micrometers at low ΔK .

spatial resolution of the measurement technique is clearly an important factor in determining the magnitude of the opening load because of the large change in values close to the crack tip. This is especially true for values of ΔK near the threshold for fatigue crack growth.

The results of numerous measurements obtained over a wide range of applied ΔK and R are presented in Figure 3. Values at low- R and low- ΔK were made in the SEM under high-resolution conditions, while values at high- R were made optically at lower resolution. A comparison between optical measurements and SEM measurements at $\Delta K = 6 \text{ MN/m}^{3/2}$ and $R = 0.1$ showed that optical microscopy resulted in ΔK_{eff} values 15% larger than those determined in the SEM, whereas at $\Delta K = 10 \text{ MN/m}^{3/2}$, the results were coincident. At higher R , optical and SEM-derived results were also in agreement, at least down to $\Delta K = 6 \text{ MN/m}^{3/2}$.

The values of $\Delta K_{\text{eff}}/\Delta K$ in Figure 3 are calculated from measured values of P_0/P_{max} using the equation

$$\Delta K_{\text{eff}}/\Delta K = (1 - P_0/P_{\text{max}})/(1 - R) \quad (1)$$

The line shown on the figure is not fit statistically because of the large scatter in the data and because some data are better than others due to the learning process which took place as more data were obtained. Nevertheless, the line shown is a fair representation of the results. The intercept of the line at $\Delta K_{\text{eff}}/\Delta K = 0$ is defined as the threshold for fatigue crack growth, and is shown as $5 \text{ MN/m}^{3/2}$ for this case. Values measured from crack growth experiments are known to be lower than this, which complicates interpretation of this concept. The reason that the threshold is lower than $5 \text{ MN/m}^{3/2}$ is believed to be related to the fact that the Mode II opening load is lower than the Mode I opening load at low ΔK . Thus, Mode I no longer controls the value of ΔK ; rather it is Mode II which sets the lower limit of fatigue crack growth.

The results of Figure 3 may be used to reinterpret the comparison between measured and computed values of $\Delta K_{\text{eff}}/\Delta K$ and R . The comparison, shown in Figure 4, indicates that a family of lines should be used to show different values of ΔK in this representation. Results of FAST-2

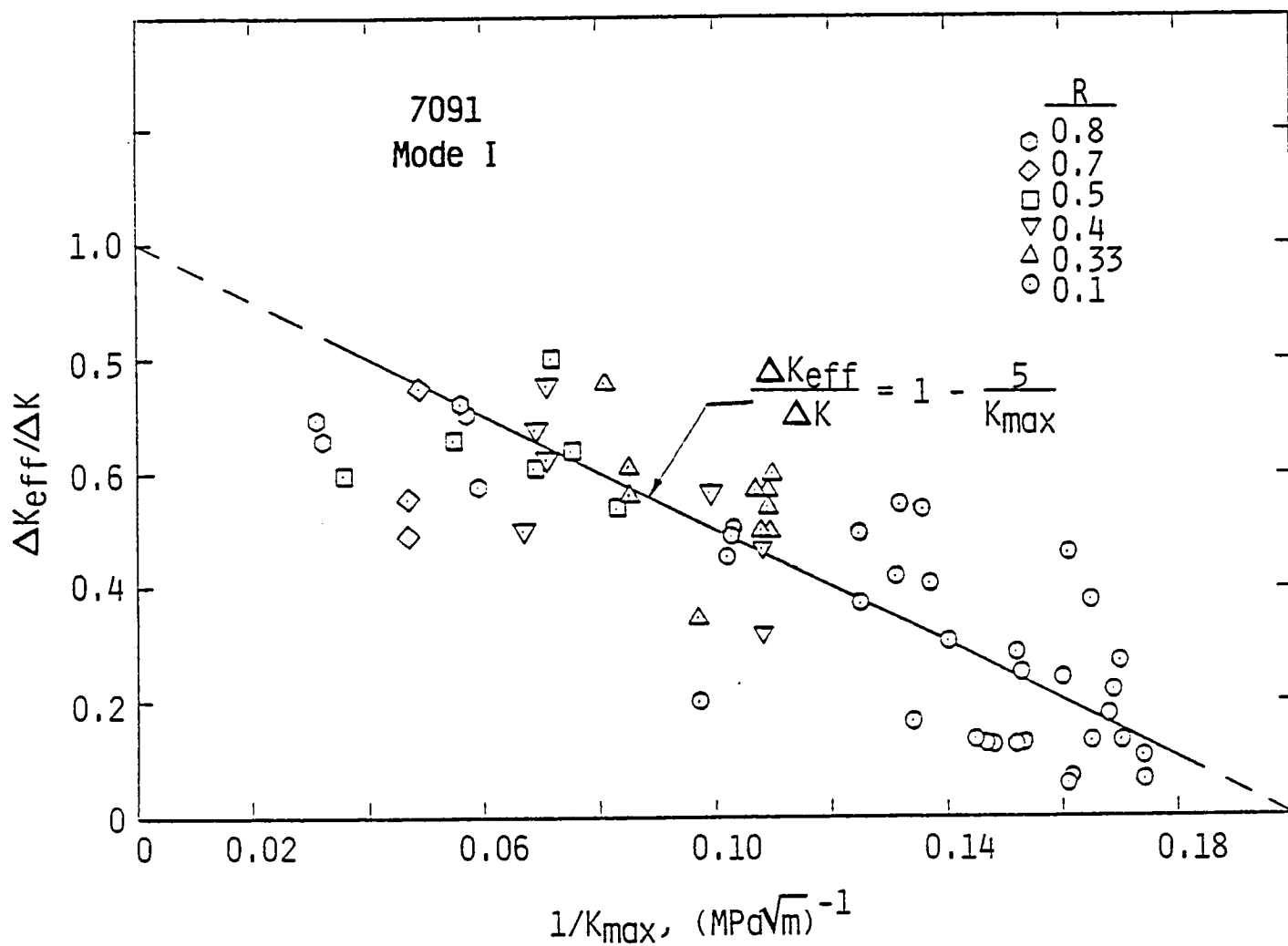


FIGURE 3. RELATION BETWEEN NORMALIZED EFFECTIVE STRESS INTENSITY FACTOR AND K_{max} , AS DETERMINED FROM LOCAL MEASUREMENTS OF OPENING LOAD IN MODE I.

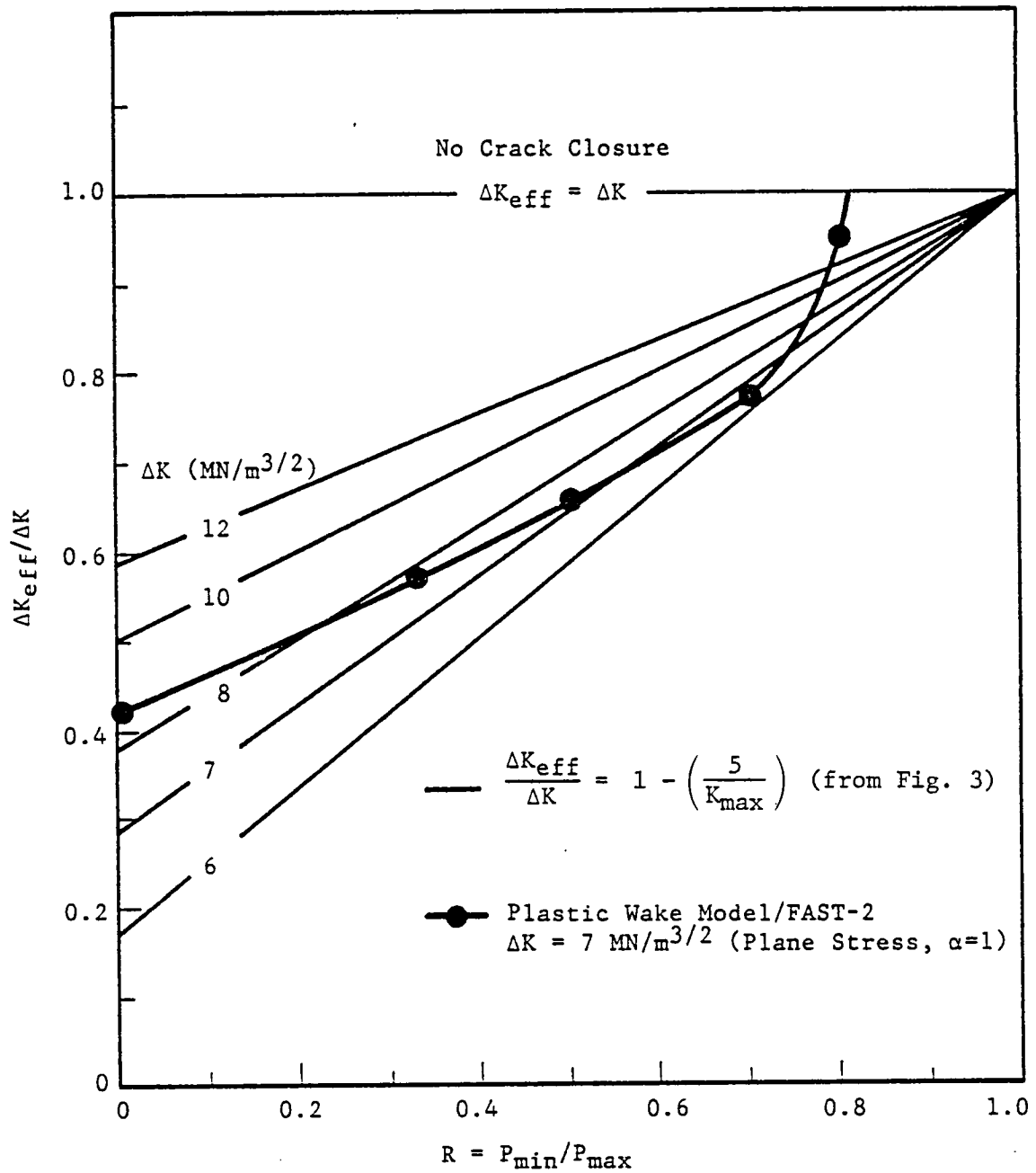


FIGURE 4. COMPARISON OF MEASURED AND PREDICTED NORMALIZED EFFECTIVE CRACK-TIP STRESS INTENSITY RANGES ($\Delta K_{eff}/\Delta K$) AS A FUNCTION OF LOAD RATIO (R) FOR CONSTANT-AMPLITUDE FATIGUE CRACK GROWTH.

were obtained at $\Delta K = 7 \text{ MN/m}^{3/2}$ and are in good agreement at intermediate R values, but diverge at both high and low values of R. At high-R, the measurements are extrapolated, so the uncertainty between measurement and computation is not resolved; however, at low-R, the measurements are very reliable and the divergence between computation and experiment is meaningful.

2.2 Comparison of Compliance and Stereoimaging Measurements of Crack Opening Load

Panels of 2024-T3 aluminum alloy (2.3 mm thick) supplied by NASA were used for these measurements. The specimen design is shown in Figure 1(b). Both potential drop and compliance techniques were used for remote measurements. An optical microscope, together with the stereoimaging technique, was used for the local measurements.

For the potential drop measurements, current leads were attached by spot welding near the loading pin holes and the potential leads were attached at the small (4.8 mm diameter) holes on either side of the center notch. Autographic recordings of potential versus applied load provided no indication of crack closure. It is presumed that oxidation of the crack surfaces due to moisture in the air was the apparent cause of the failure to obtain crack opening measurements by potential drop, and efforts to make meaningful measurements with this technique were abandoned. In order to have been successful, it appears that it would have been necessary to conduct these experiments in a vacuum or inert gas environment.

All compliance measurements were made with the compliance gage located 2 mm behind the crack tip. Selected measurements were also made with the compliance gage located 8 to 10 mm behind the crack tip. However, no measurable difference in crack opening load was obtained for these two locations. For the compliance gage used, the gage length of the displacement measurement was 5 mm.

Fatigue cracks were extended under constant-amplitude loading at $R = 0.05$ and $P_{\max} = 1053 \text{ lb}$, and measurements were made at relative crack lengths (a/W) of 0.26.

Results of crack opening load measurements by compliance are compared with those by stereoimaging of optical photographs in Figure 5. Both

$$P_{op}/P_{max} \quad R=0.05$$

2024 A1

7091 A1

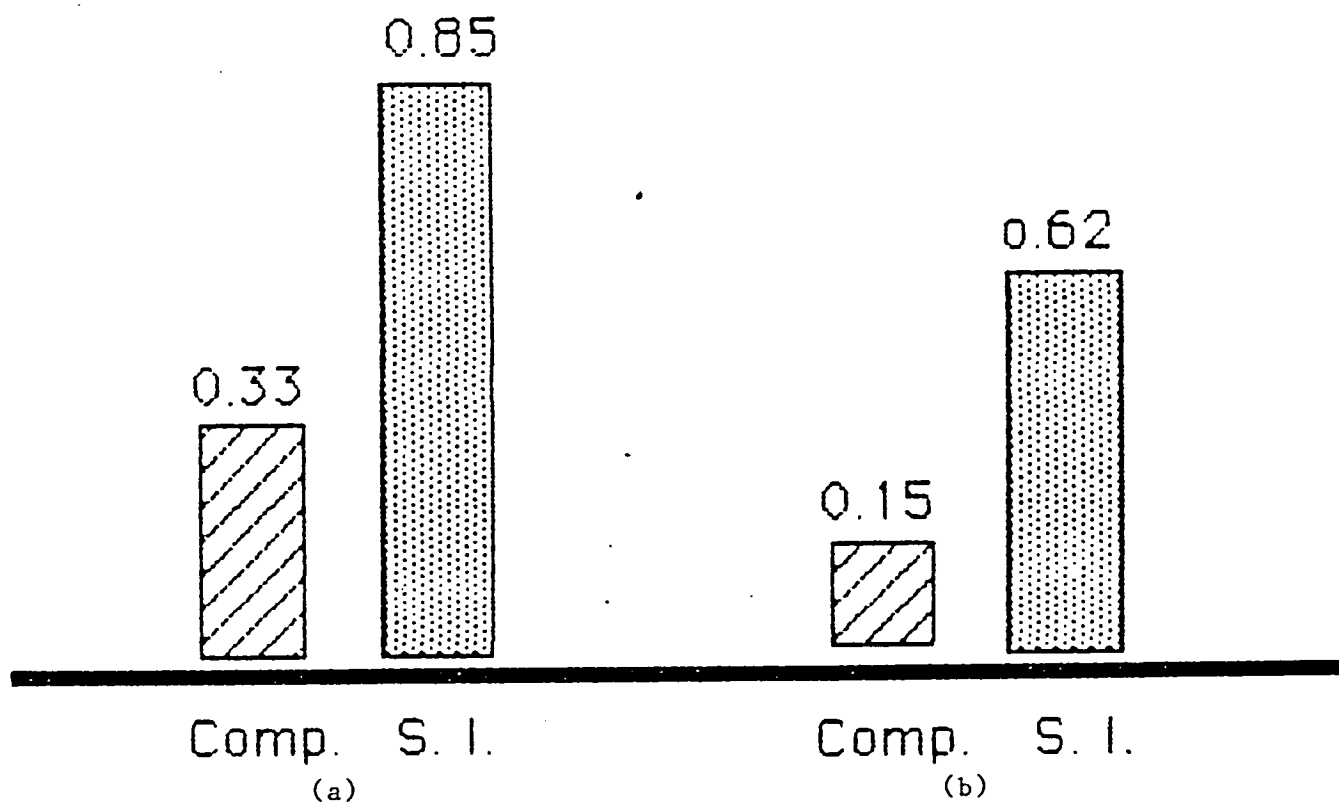


FIGURE 5. COMPARISON OF THE OPENING LOAD TO MAXIMUM LOAD RATIO AS DETERMINED REMOTELY (COMPLIANCE) AND LOCALLY (OPTICAL MICROSCOPY WITH STEREOIMAGING) FOR (a) 2024 PANELS SUPPLIED BY NASA, AND (b) 7091. (a) For 2024, both measurements were made at SwRI on the same specimen, while (b) for 7091, local measurements made at SwRI are compared with compliance measurements reported by McEvily.

compliance and stereoimaging measurements were made on the 2024 specimens at SwRI, while for the 7091 measurements, the compliance values were derived from work reported by McEvily [2]. As the figure illustrates, stereoimaging measurements in each case give higher values of opening load than do the compliance measurements, a finding consistent with the results of Figure 2.

3.0 CRACK-TIP STRAIN AND STRESS FIELDS DURING CONSTANT-AMPLITUDE AND VARIABLE-AMPLITUDE FATIGUE CRACK GROWTH

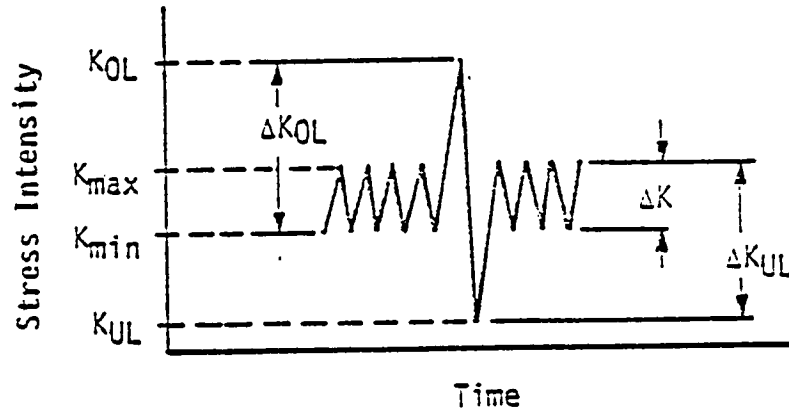
Three overload sequences have been analyzed in great detail, with one of the overloads being followed by an underload. In each case, measurements were made before, during, and after the overload event; thus information was obtained for both constant-amplitude and variable-amplitude fatigue crack growth. The history of each load excursion analyzed is shown in Figure 6, and the relevant loading parameters for each case are listed. A comparison of the crack growth rates subsequent to each of these load excursions is shown in Figure 7, along with determinations of effective stress intensity factors.

The methodology used for analysis of each load excursion will be detailed for one of the overloads in the next section. Summary information for all cases examined will then be presented.

3.1 Analysis of Experiment 1: $OLR^* = 2.15$, $ULR^* = 1$, $R = 0.16$, $\Delta K = 6.2 \text{ MN/m}^{3/2}$

In preparation for the load excursion event, a photograph was taken under minimum load at a location several hundred micrometers ahead of the crack tip. This is labeled as Photograph No. 1 on Figure 8. The specimen was then cycled until the crack had grown into the field of this photograph, and a matching picture (No. 2) was taken at minimum load. Next, Photograph No. 3 was taken at the maximum load of the cyclic range. Comparison of Photographs 1 and 2 shows the effect of the crack being present, and comparison of Photographs 2 and 3 gives the cyclic crack-tip parameters just prior to the load excursion. The crack opening load was also measured on this last constant amplitude cycle.

The overload cycle was then applied, with Photograph No. 4 taken at the maximum load, and No. 5 taken at the minimum load, as shown in Figure 8. Comparison of Photographs 2 and 4 shows the effect of the loading portion of the overload, while the reversibility due to the subsequent unloading part of the cycle is shown by comparison of Photographs 4 and 5.



$$R = K_{\min} / K_{\max}$$

$$OLR^* = \frac{K_{OL} - K_{\min}}{K_{\max} - K_{\min}} = \frac{\Delta K_{OL}}{\Delta K}$$

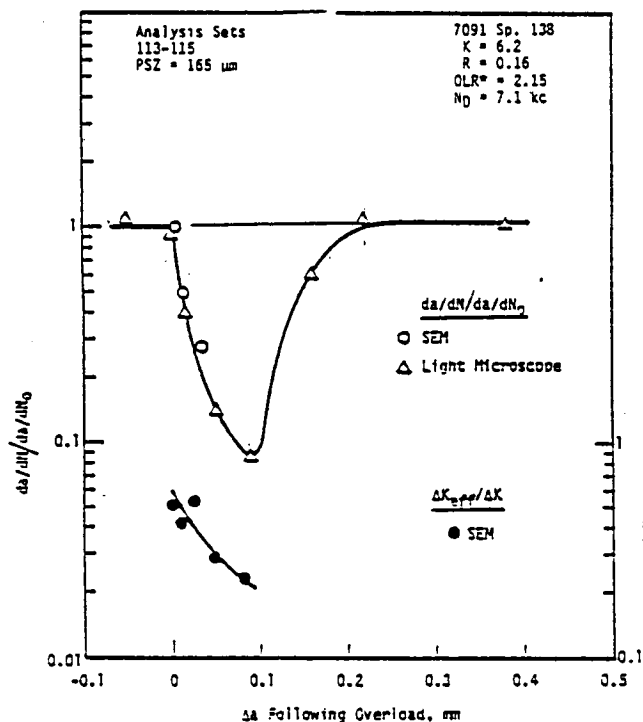
$$ULR^* = \frac{K_{\max} - K_{UL}}{K_{\max} - K_{\min}} = \frac{\Delta K_{UL}}{\Delta K}$$

Conditions Tested

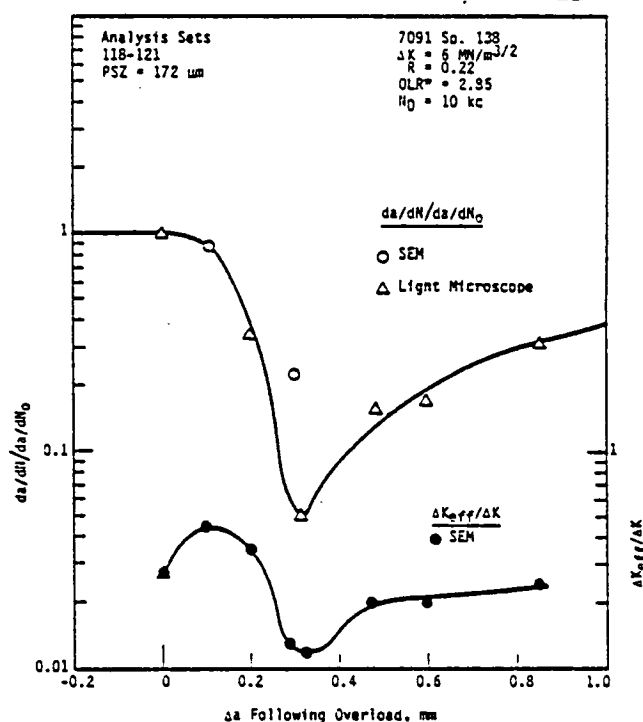
<u>Experiment</u>	<u>R</u>	<u>ΔK, MPa\sqrt{m}</u>	<u>OLR*</u>	<u>ULR*</u>
1	0.16	6.0	2.15	1.0
2	0.22	6.2	2.85	1.0
3	0.50	7.2	3.0	2.0

Note: For each sequence stereoinaging data were taken for both loading and unloading of overload cycle plus two or three additional times during the subsequent delay period.

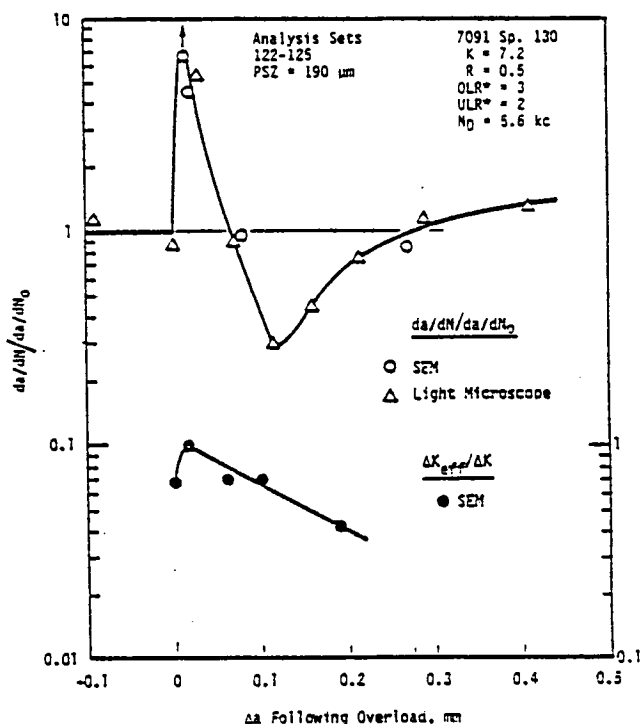
FIGURE 6. DEFINITION OF LOADING PARAMETERS AND SUMMARY OF SEQUENCES FOR WHICH RESIDUAL STRESSES WERE DETERMINED.



(a) Measured crack growth rate response and ΔK_{eff} following a single overload at $R = 0.16$, $OLR^* = 2.15$.



(b) Measured crack growth rate response and ΔK_{eff} following a single overload at $R = 0.22$, $OLR^* = 2.85$.



(c) Measured crack growth rate response and ΔK_{eff} for a single overload followed by an underload to near zero ($R = 0.5$, $OLR^* = 3$, $OLR^* = 2$).

FIGURE 7. CRACK GROWTH RATE AND EFFECTIVE STRESS INTENSITY FACTOR HISTORIES OF THE THREE LOAD EXCURSIONS ANALYZED USING STEREOIMAGING. Cases (a) and (c) are similar to those for which results were obtained using FAST-2.

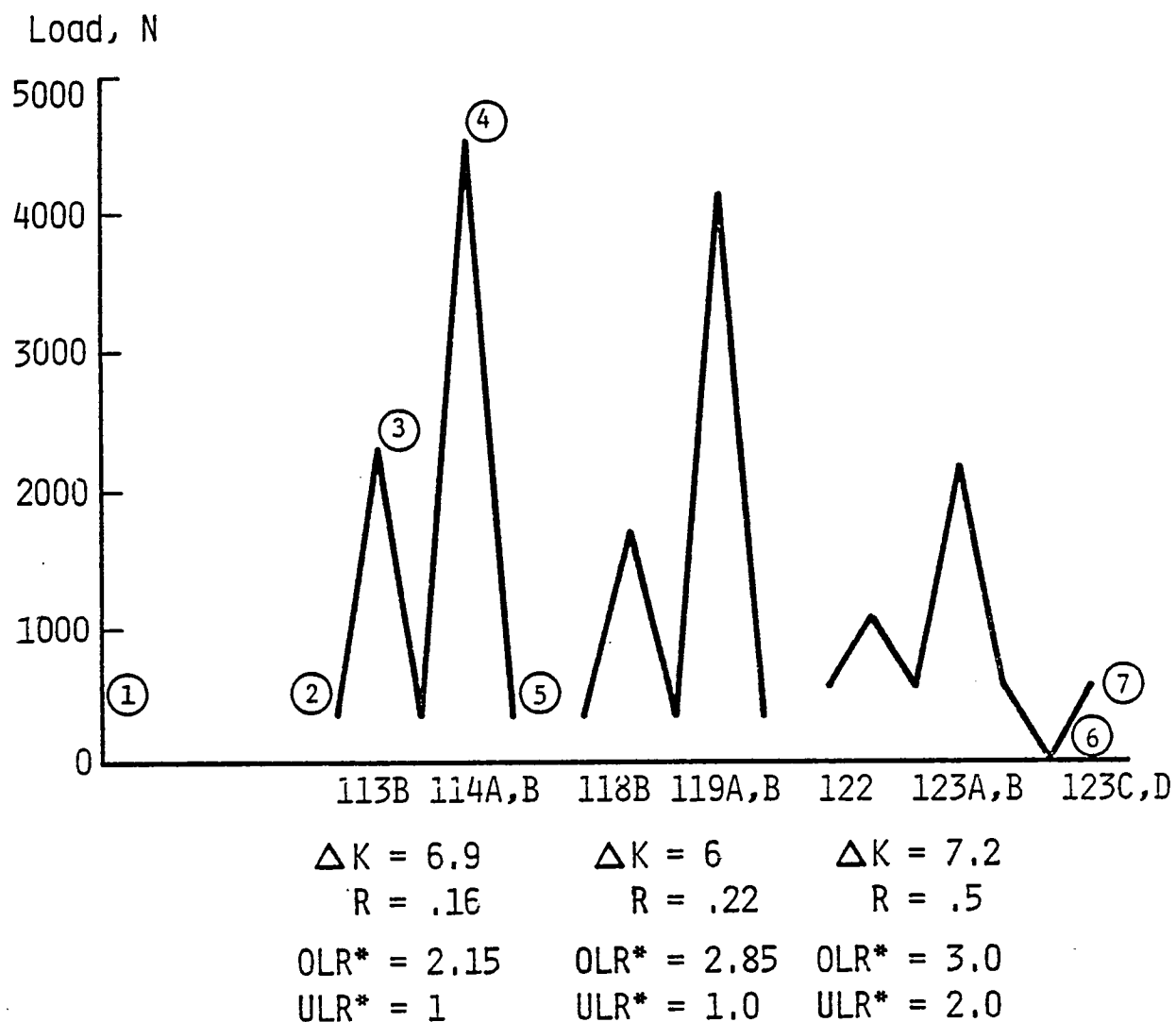


FIGURE 8. LOADING HISTORY FOR THE THREE LOAD EXCURSIONS ANALYZED. The circled numbers indicate the points where photographs were taken for subsequent analysis. Below each part of the figure is information describing the loading history.

Data sets are labeled as indicated in Table 1 and partially shown in Figure 8. Examination of these data were made using the stereoimaging technique [3], and measurement of the displacements was accomplished using the methods of photogrammetry. Strains were computed from the gradients of the measured displacements [4].

3.1.1 Results Before the Overload

The net displacements caused by the growth of the crack (comparison of Photographs 1 and 2) are shown in Figure 9. The displacements are seen to be small and are local to the crack region, as anticipated. Most of the displacements occur within a few micrometers of the crack. Net displacement in the loading direction across the region marked D_R on Figure 9 is $0.12\text{ }\mu\text{m}$. Strains have been computed for this case and are shown in Figure 10 as Mohr's circles. With a few exceptions, the strains are less than a few percent.

For constant-amplitude cyclic loading prior to the overload, displacements (Figure 11) are similar to previous work with this material [5]. The distribution of maximum shear strains in the near crack tip vicinity is shown in Figure 12. Note the asymmetric and biaxial nature of the displacements about the crack, but the more symmetric distribution of shear strains. These findings are similar to previous results for 7075-T651 and Ti-6Al-4V.

3.1.2 Results for the Overload Cycle

Displacements caused by the loading portion of the overload cycle are shown in Figure 13, and those due to unloading are shown in Figure 14. Greater symmetry is evident in the overload cycle than is found in the cyclic response prior to the overload, and considerable reversibility in displacements is evident upon unloading.

Strains computed from the displacements shown in Figures 13 and 14 have the same general distribution as the cyclic strains before the overload, but peaked much more near the crack tip. Further analysis of these strains will be found in the next section.

TABLE 1
LABELING OF DATA SETS ANALYZED

Suffix	Condition
Preoverload	
A	no crack vs unloaded crack photograph 1 vs 2
B	unloaded crack vs loaded crack photograph 2 vs 3
Overload Cycle	
A	loaded crack vs maximum load photograph 3 vs 4
B	crack at maximum load vs unloaded crack photograph 4 vs 5
Underload Cycle	
C	crack unloaded after overload vs maximum underload photograph 5 vs 6
D	crack at maximum underload vs unloaded crack photograph 6 vs 7

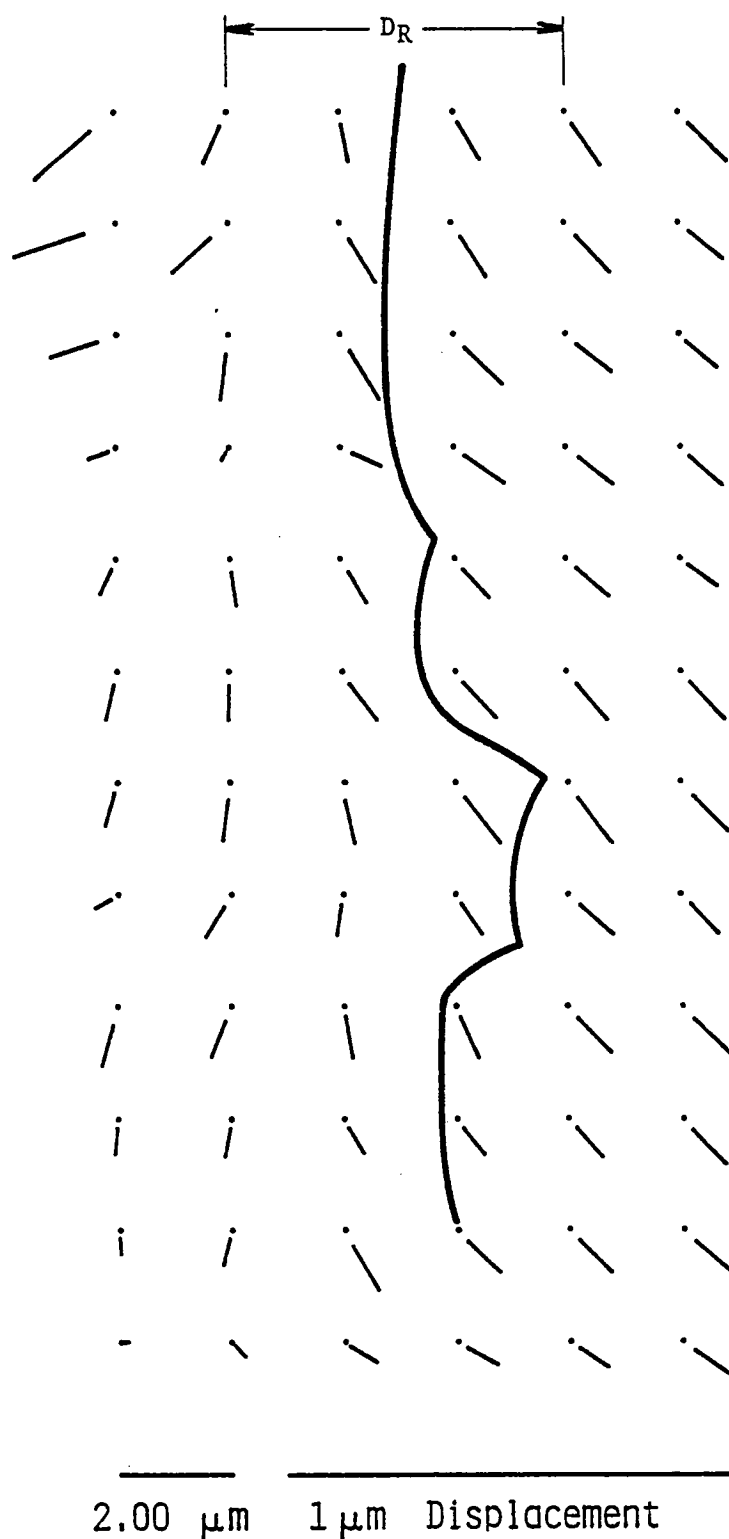
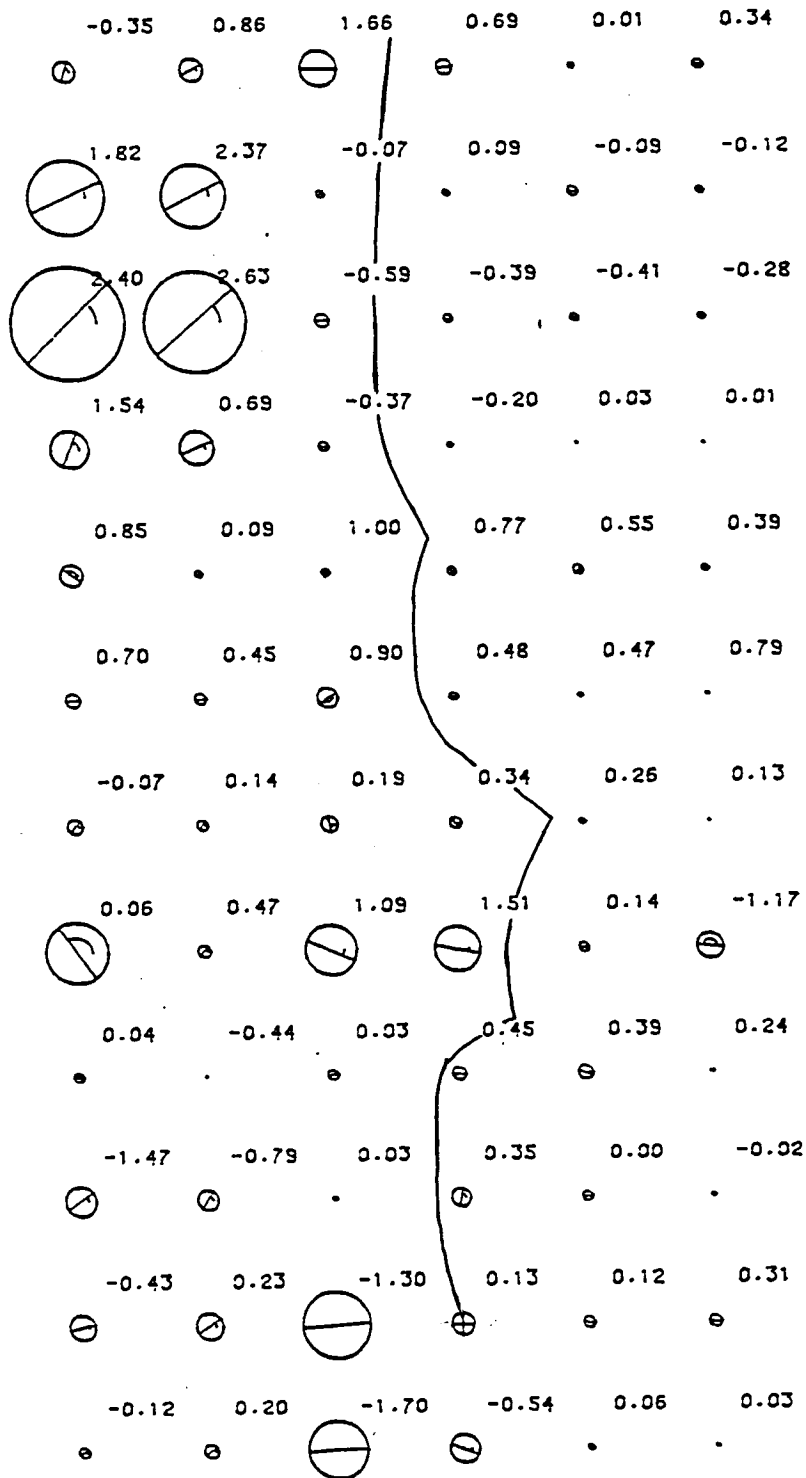


FIGURE 9. DISPLACEMENTS CAUSED BY THE PRESENCE OF THE CRACK. These were determined by comparison of photographs #1 and #2 of Fig. 8. Note that displacements were measured each two micrometers (scale on the left), and that the scale of displacements is greatly magnified (scale on the right). The dot marks the original position of the material point, and the tip of the line is the point to which the material has been displaced by passage of the crack.



2 MICRONS 10% STRAIN

FIGURE 10. MOHR'S CIRCLES OF STRAIN AS DERIVED FROM THE DISPLACEMENTS SHOWN IN FIGURE 9. Maximum shear strain is the diameter of the circle, while the mean strain is indicated by a numeral.

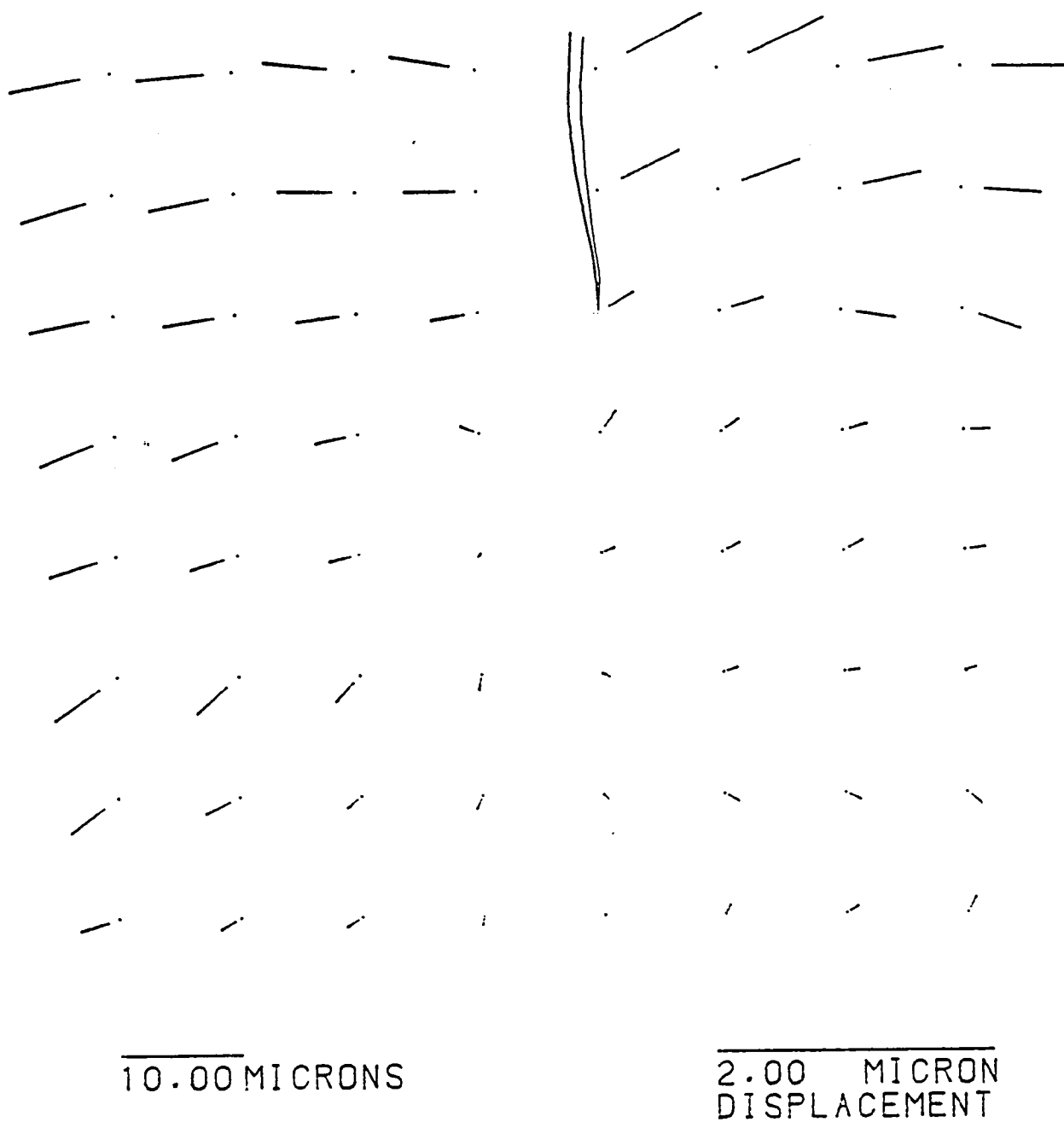


FIGURE 11. DISPLACEMENTS FOR THE CYCLIC CRACK JUST PRIOR TO THE OVERLOAD CYCLE. Note that the displacement magnitude is larger than the actual spatial scale.

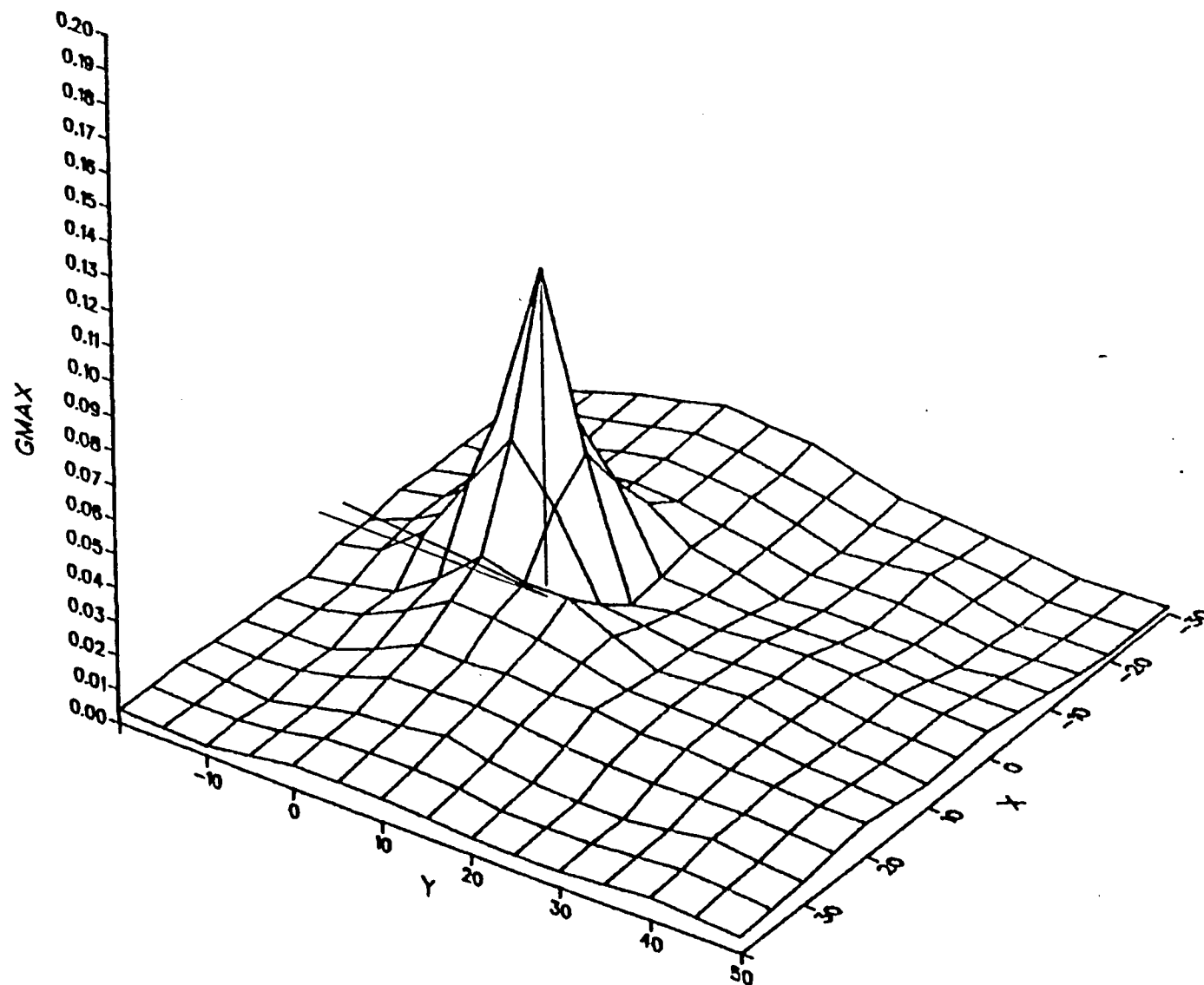


FIGURE 12. DISTRIBUTION OF THE MAXIMUM SHEAR STRAIN FOR THE CYCLIC CRACK JUST PRIOR TO THE OVERLOAD CYCLE. The crack is shown schematically on the plane of zero strain.

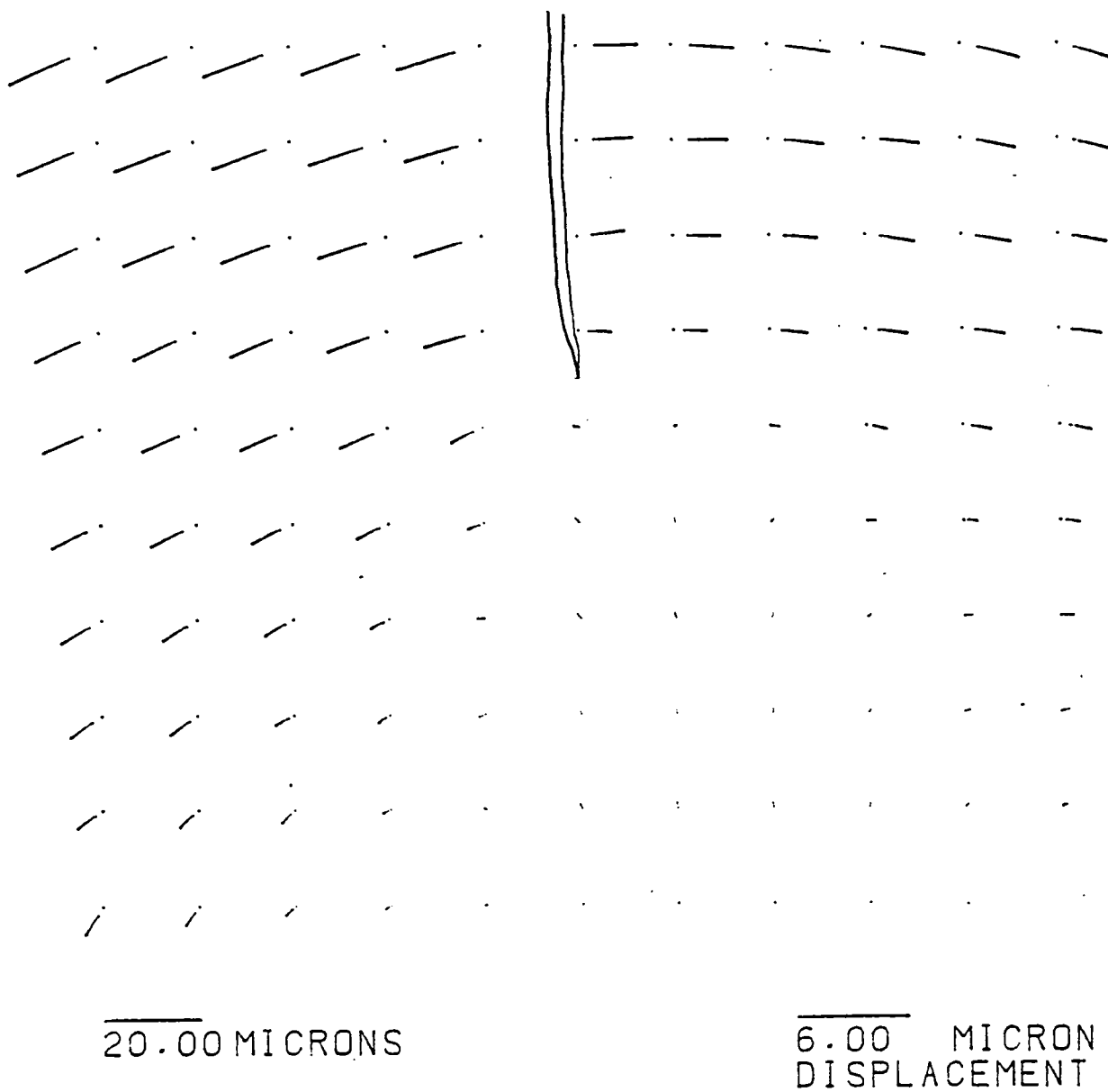


FIGURE 13. DISPLACEMENTS CAUSED BY THE CRACK BEING LOADED TO MAXIMUM VALUE DURING THE OVERLOAD CYCLE. These displacements were determined from comparison of photographs #2 and #4 of Figure 8.

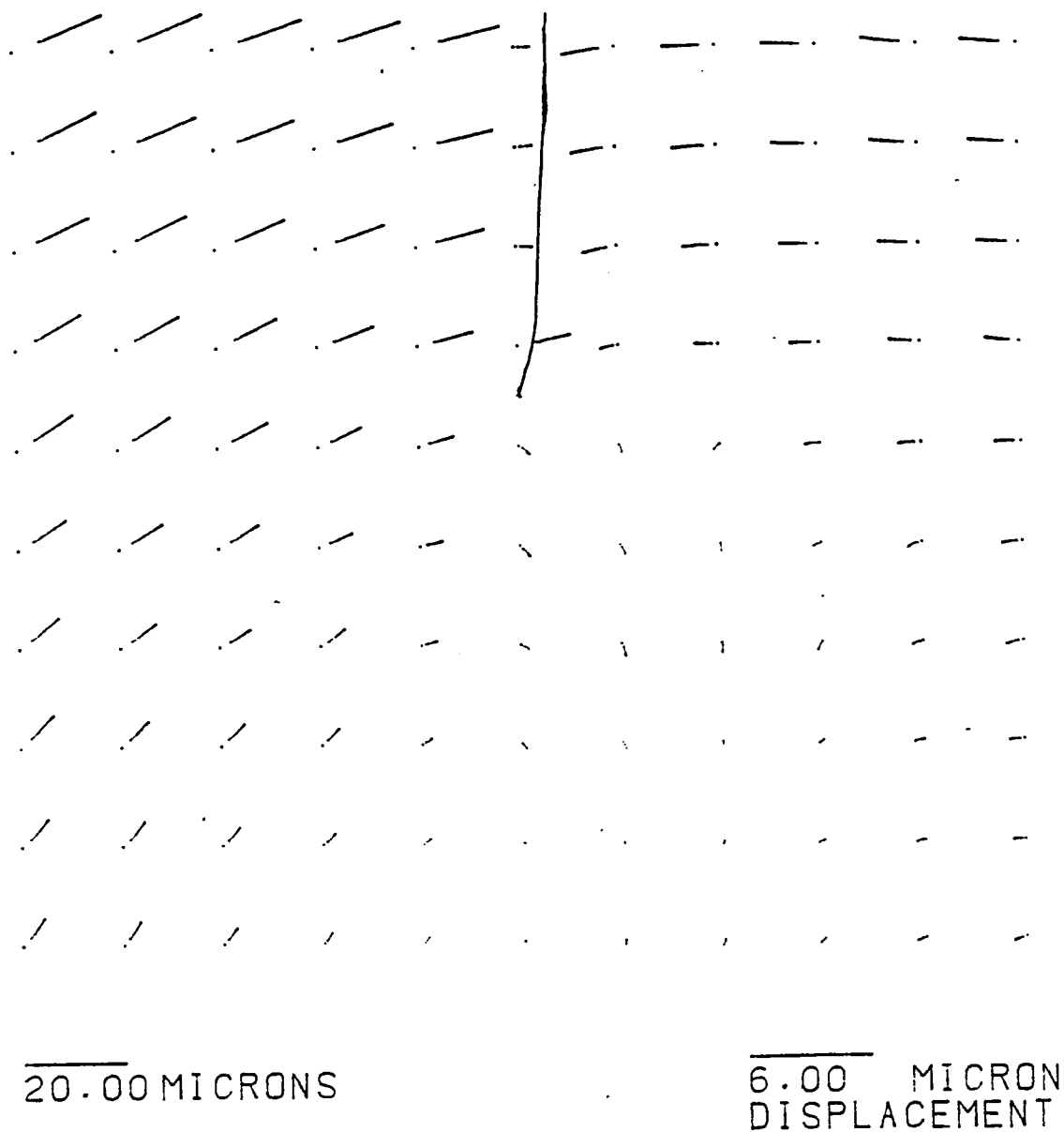


FIGURE 14. DISPLACEMENTS CAUSED BY THE UNLOADING PORTION OF THE OVERLOAD CYCLE. Comparison with Figure 13 indicates considerable reverse material flow.

3.1.3 Computation of Stresses

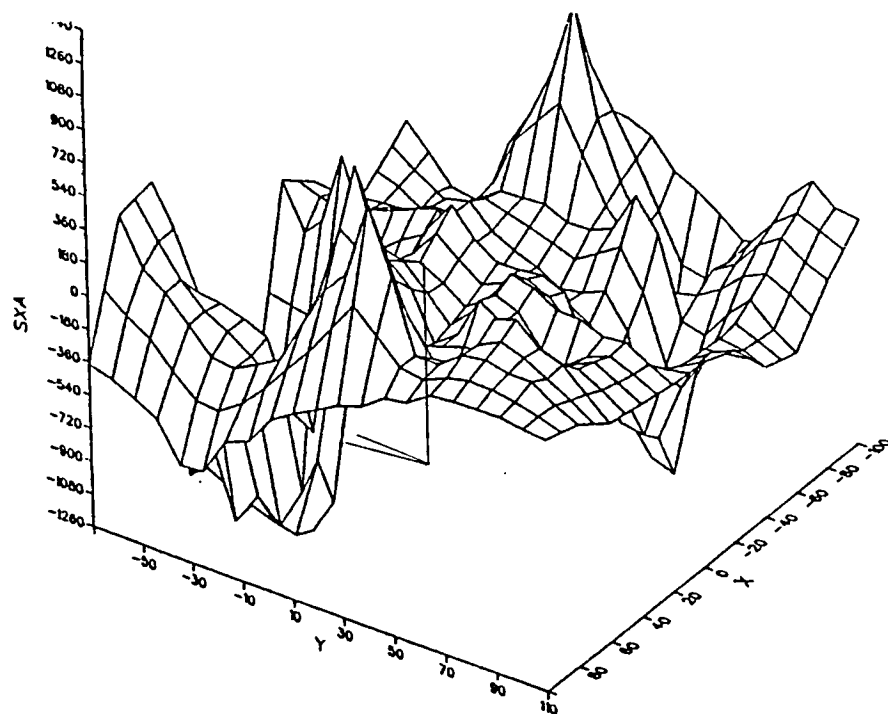
One of the major efforts of this analysis has been to compute the distribution of residual stresses which result from the load excursion. Stresses were computed from strains at each step in the applied loading sequence, using a procedure previously derived [6]. This computation requires knowledge of the appropriate stress-strain curves. Consequently, the monotonic and cyclic stress-strain curves were measured for this material and were reported previously [1]. The cyclic and monotonic curves are nearly equal and there is essentially no difference between the tension and compressive monotonic curves. The cyclic hysteresis loops were nearly perfect in symmetry, and stabilized very rapidly after a change in strain range.

To obtain the residual stress values, coordinate values of each stress, together with the shear stress, were computed at each node around the crack tip [6], for each step in the loading sequence, and then added together to produce a net residual stress, which occurred due to the nonuniformity and nonreversibility of deformation within the plastic zone.

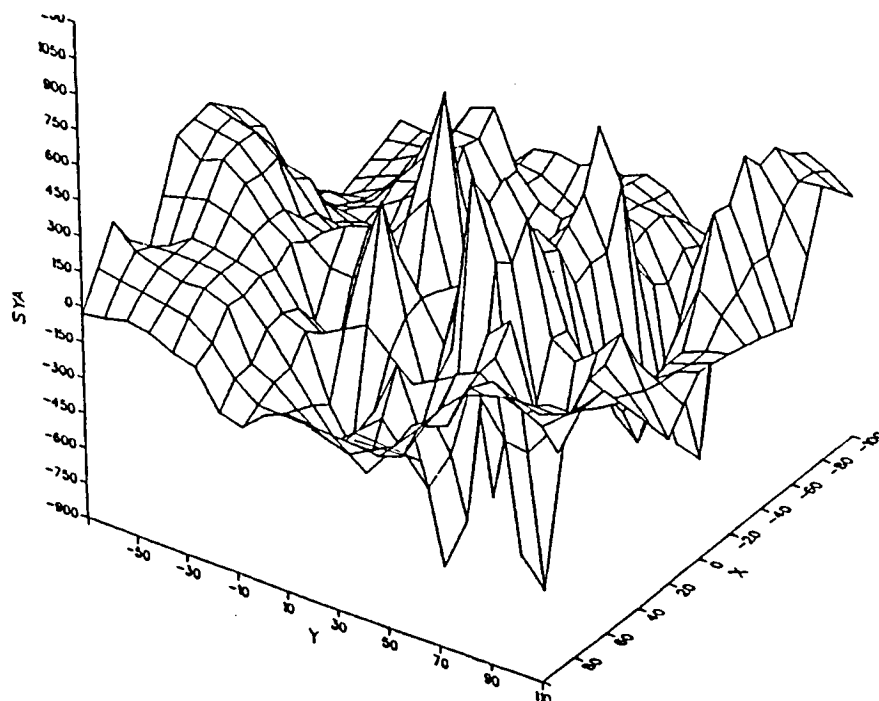
For each load excursion, the result of the stress computation was six components of stress at each point of the analysis. Two of these stresses were chosen for detailed analysis: the stress in the loading axis (σ_x) and the total effective stress (σ_{eff}) were chosen because the loading axis stress could be expected to exert a direct clamping influence on the crack, and the effective stress was examined because it considers both the normal and shear stresses in its computation and represents a stress equivalent to what might be applied in a tensile test.

3.1.4 Determination of Residual Stress

Mostly positive residual stresses in the loading axis resulted, in each case analyzed, from summing the stresses on the loading and unloading portions of the overload cycle, as would be expected, because the net deformation caused by the overload was generally tensile, and no compensation was made for the fact that the overload cycle began at the minimum in the hysteresis loop, which is at a negative stress. The situation described above is depicted in Figure 15(a), while Figure 15(b) shows



(a)



(b)

FIGURE 15. DISTRIBUTION OF THE STRESSES RESULTING FROM THE OVERLOAD. The stresses resulting from the loading and unloading portions of the cycle were added to produce the stresses shown. (a) is the distribution of stresses in x, the axis of loading, and (b) the distribution of stresses in y, the direction of crack growth.

the stress perpendicular to the loading axis, and Figures 15(c) and (d) show the maximum principal stress and the effective stress, respectively. In order to adjust the stresses to their correct value along the stress axis, it was thus necessary to subtract the value of the negative residual stress caused by the previous cyclic loading history of the crack.

The stresses in the specimen at the minimum cyclic load and caused by the constant-amplitude cyclic loading history can be derived from using the data of Figure 11, which resulted in analysis of Photographs 2 and 3 (data sets "A"). First the stresses were computed from the strains, but because of the localized nature of the cyclic loading, these data were taken from photographs at higher magnification than the photographs of the subsequent overload cycle. Therefore, in order to obtain common nodal points from which stresses could be added, a model of the stresses for the cyclic loading prior to the overload was constructed from the computer values. The modeling procedure consisted first of graphing the computed stresses. These were then made symmetric about the line of the crack because, on average, this is the behavior which has been experimentally found. Close to the crack tip, stresses computed from strains were used, but farther away from the crack, where plasticity had ceased to dominate, these stresses were faired into the stresses computed for an elastic crack. A comparison of the actual and modeled stresses is shown in Figure 16.

This modeling procedure allowed the stresses to be computed at the same nodal points for which analyses were made after the load excursion. The stress field derived using this method is shown in Figure 17. The stresses shown are the change in stress between minimum and maximum cyclic load.

The next step was to determine how much of the stress range computed was actually compressive when the load was at minimum. Opening load was used to make this estimate. The stress range was partitioned using the fraction of total K change which was effective, as computed from the opening load. The concept is shown in Figure 18. The fraction of stress computed to be negative from the cyclic loading analysis was then subtracted from the net stress resulting from the load excursion. The resulting stresses

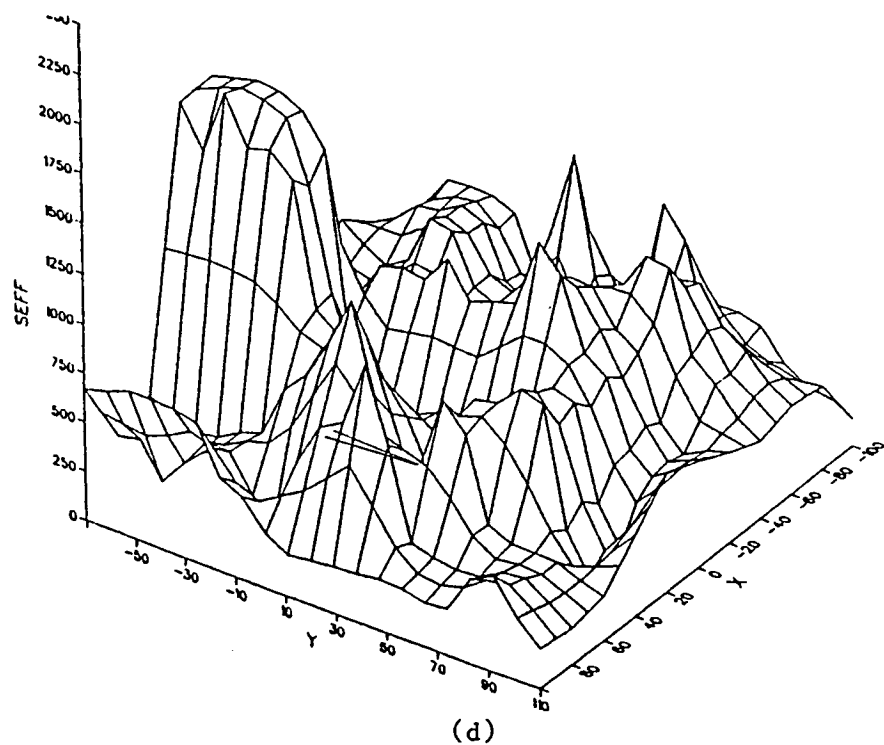
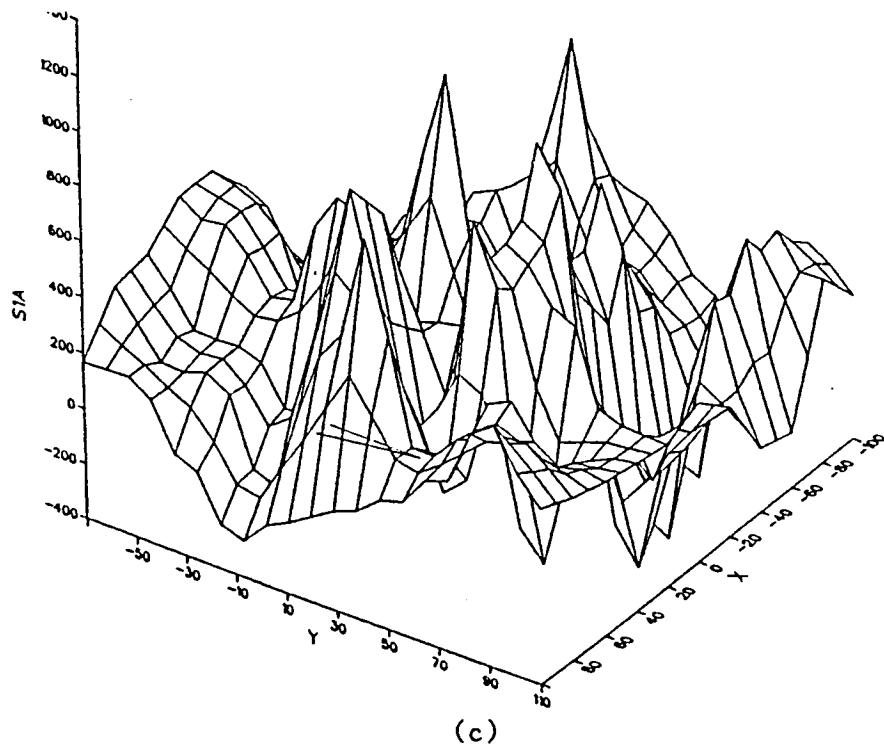
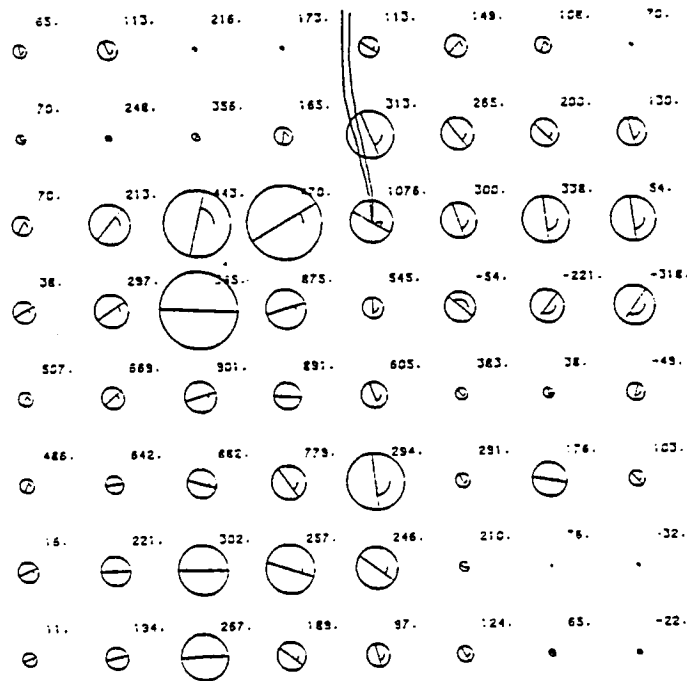
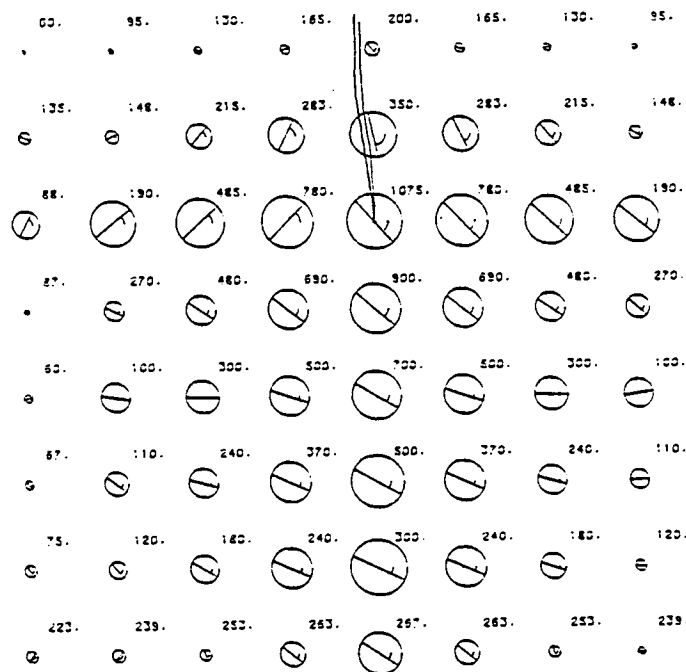


FIGURE 15 (CONTINUED). DISTRIBUTION OF THE STRESSES RESULTING FROM THE OVERLOAD. The stresses resulting from the loading and unloading portions of the cycle were added to produce the stresses shown. (c) is the distribution of maximum principal stress, and (d) the distribution of the effective stress.



10 MICRONS

1100MPA STRESS
(a)

10 MICRONS

1100MPA STRESS
(b)

FIGURE 16. MOHR'S CIRCLES OF STRESS FOR THE CYCLIC CRACK PRIOR TO THE OVERLOAD. (a) as determined directly from the measured strains, and (b) as determined from a model of the crack tip stress field.

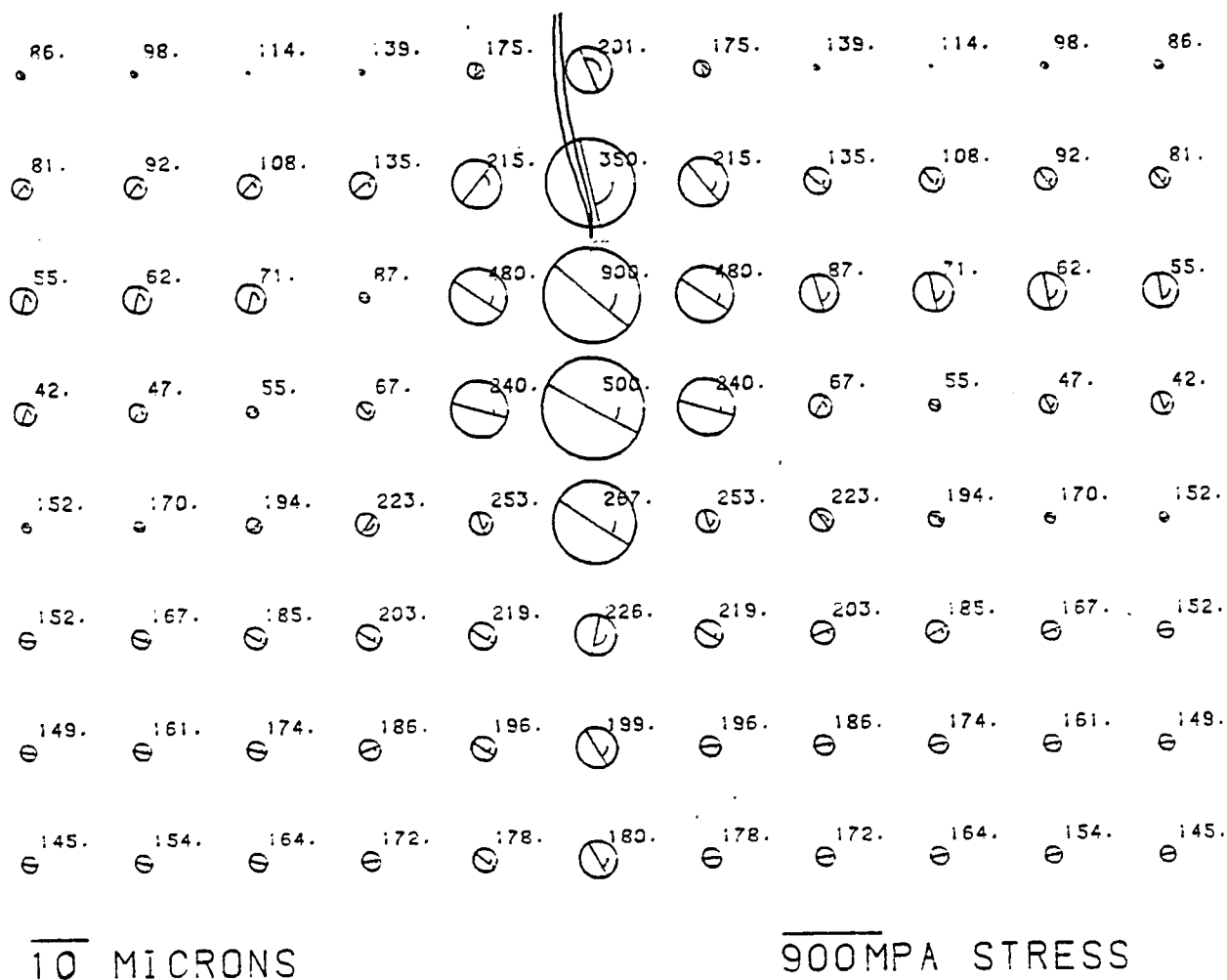


FIGURE 17. CYCLIC STRESSES AS DETERMINED FROM THE MODEL AND EXTRAPOLATED TO COVER THE SAME FIELD AS THE OVERLOAD CYCLE ANALYSES.

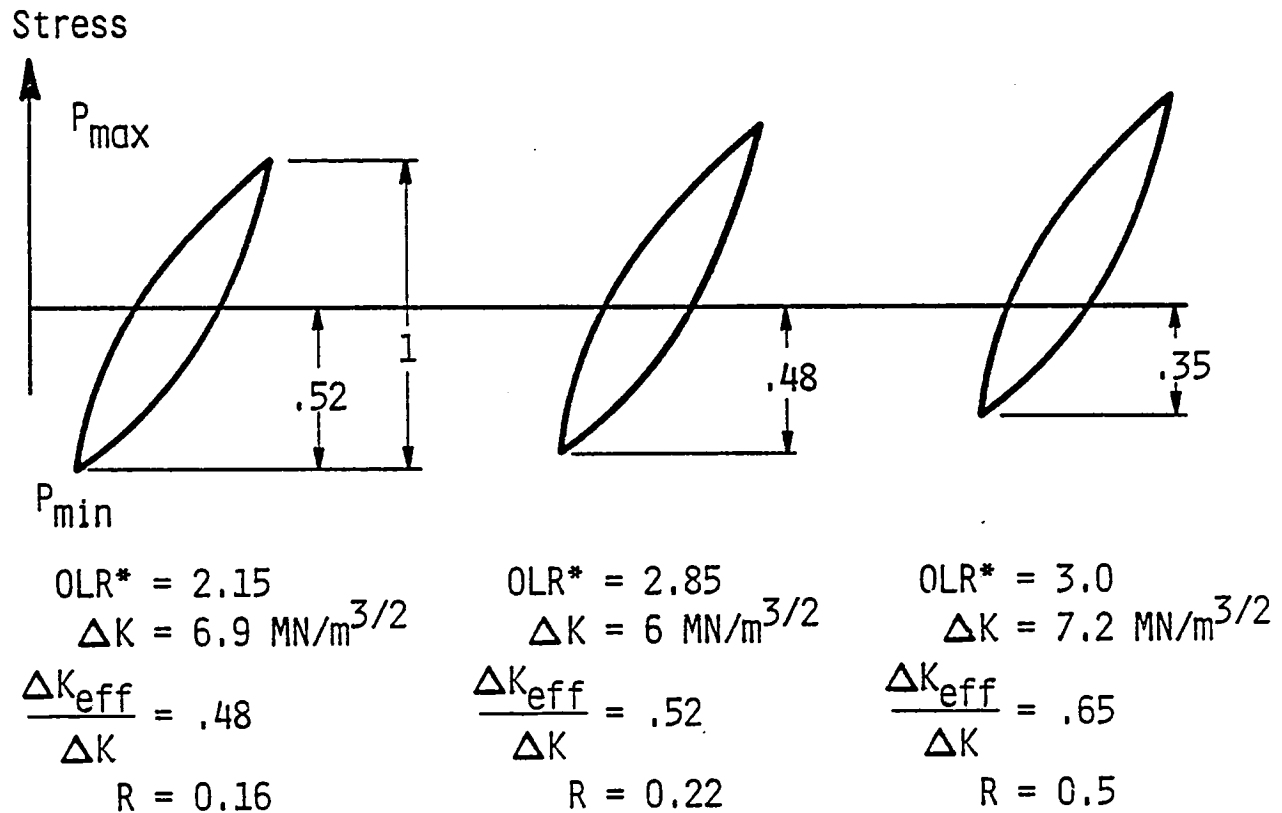


FIGURE 18. PARTITIONING OF THE CYCLIC STRESS RANGE PRIOR TO THE OVERLOAD. Partitioning is done by using the measured crack opening load, and is assumed to be equally distributed throughout the plastic zone.

in the load axis (σ_x) and the effective stress are shown in Figures 19 and 20. In Figure 21, a cross section through the residual stress field of Figure 19 is shown along the crack plane ($x = 0$), in order to make visualization of the effect clearer.

3.1.5 Post-Overload Cycling

After the load excursion, the cyclic loading range was returned to that previously applied, and crack growth was monitored as the crack progressed through the plastic zone of the load excursion. At two points along this growth path, additional analyses were made of the crack-tip strain field. One point was chosen to be as close as possible to the point of minimum crack growth rate. The opening load at each point was measured and the strains around the crack tip were determined. An analysis was made to determine if the crack tip strain fields were in similitude with the crack-tip field before the load excursion and whether the crack-tip strains correlated with crack growth rates.

3.2 Comparative Analysis of the Load Excursions

The analysis method outlined in the previous section was applied to all the loading variations shown in Figure 8. This section summarizes the findings of the other two load variations studied and compares the results.

3.2.1 Overload Cycle Strains

Maximum shear strains at the peak of the overload cycle are compared in Figure 22. It is apparent that strain magnitude increases with the magnitude of the stress intensity factor. Crack-tip strain fields have also been determined for a crack loaded monotonically in tension, and the crack-tip strains for the overload cycle and monotonic loading are compared in Figure 23, where it may be seen that the correlation between crack-tip strain and stress intensity factor for monotonic loading is different than for the overload cycle.

The distribution of strains directly ahead of the crack has been examined for the three overload cycles and is shown in Figure 24. Strains

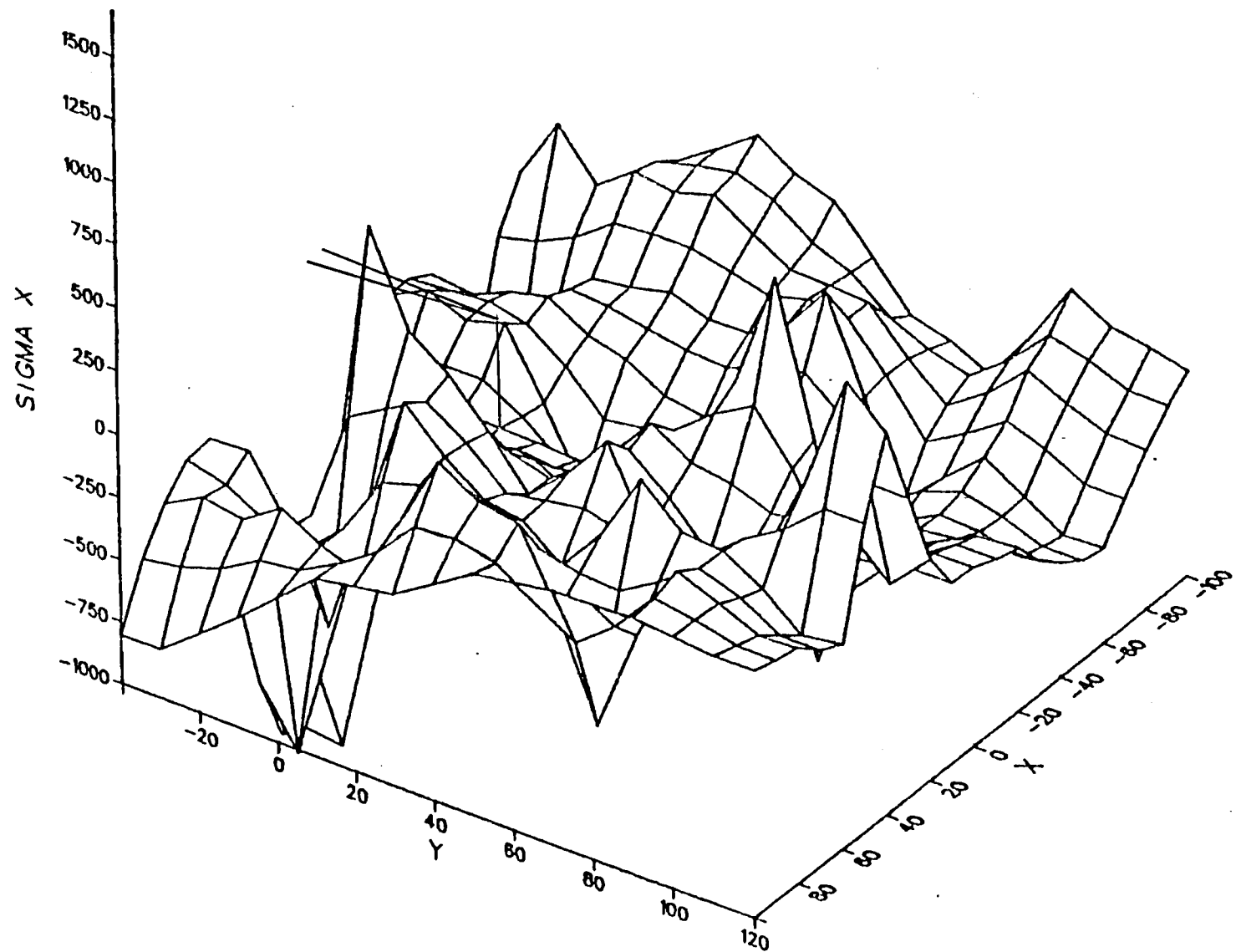


FIGURE 19. THE RESIDUAL STRESS IN THE DIRECTION OF LOADING WHICH RESULTED FROM APPLICATION OF THE OVERLOAD. These stresses are the sum of those shown in Figure 15(a) and Figure 17, as partitioned using the concept of Figure 18.

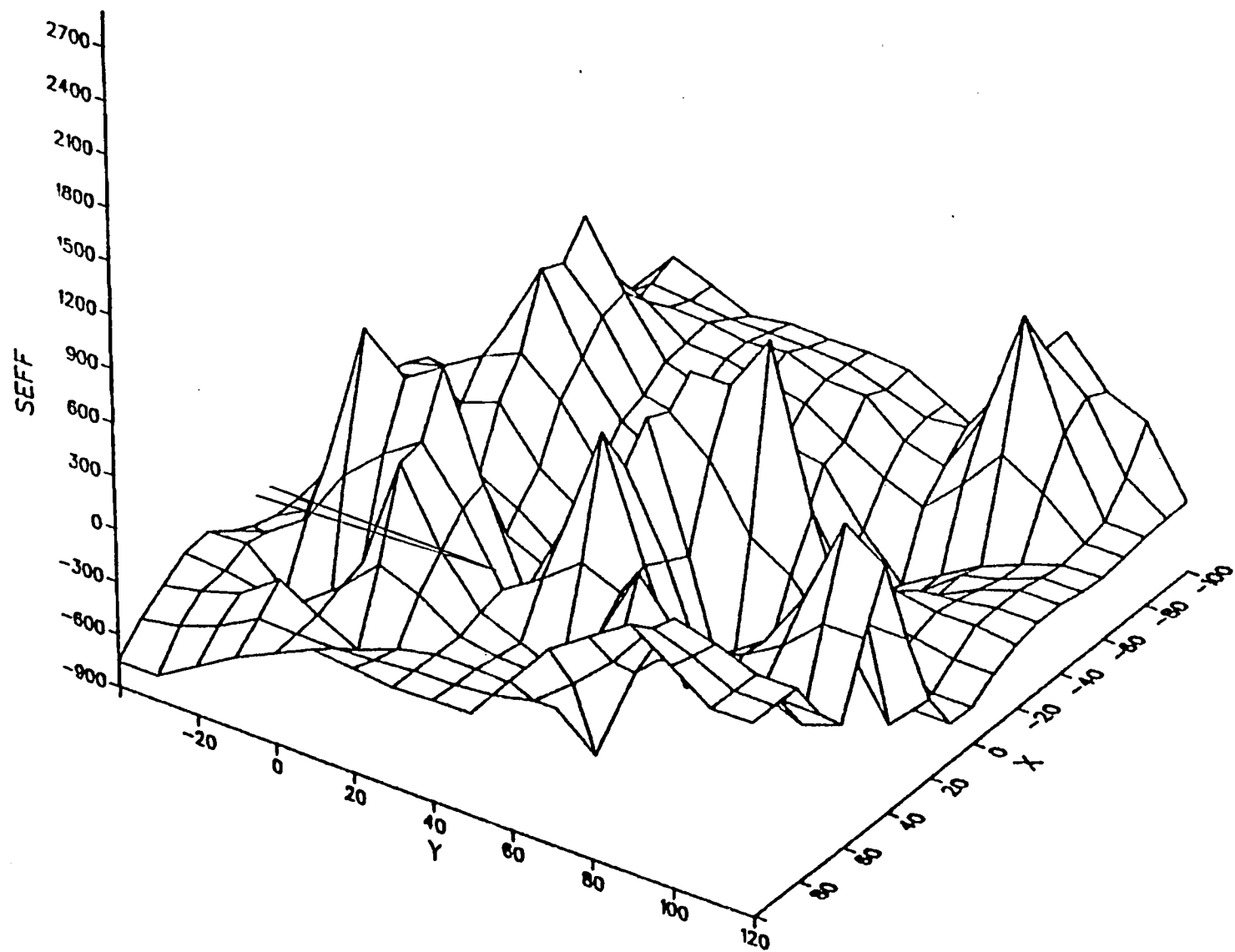


FIGURE 20. THE RESIDUAL EFFECTIVE STRESS RESULTING FROM THE OVERLOAD. These stresses were derived using the same method as described for Figure 19.

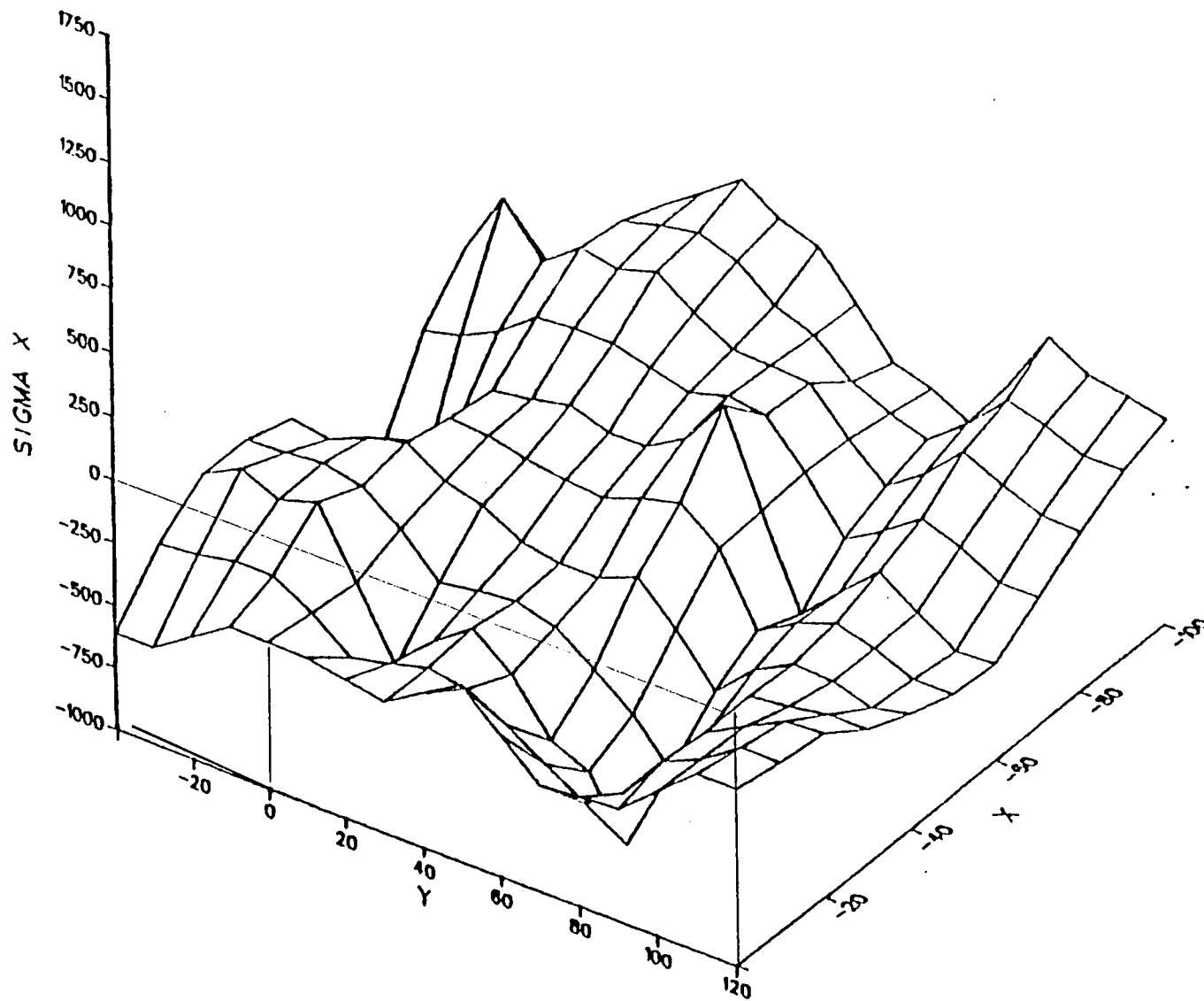
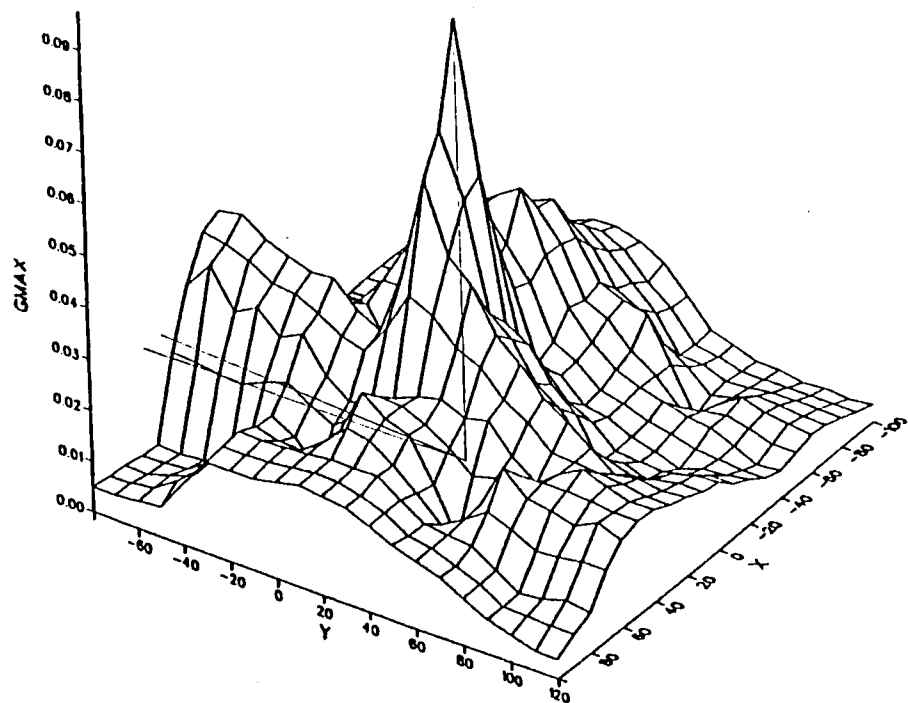
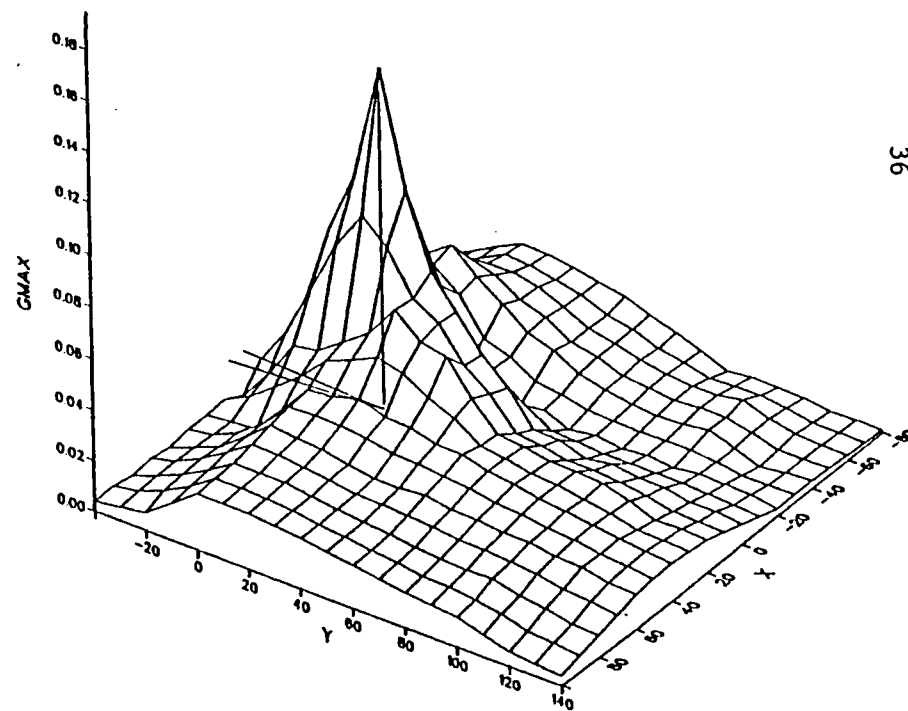


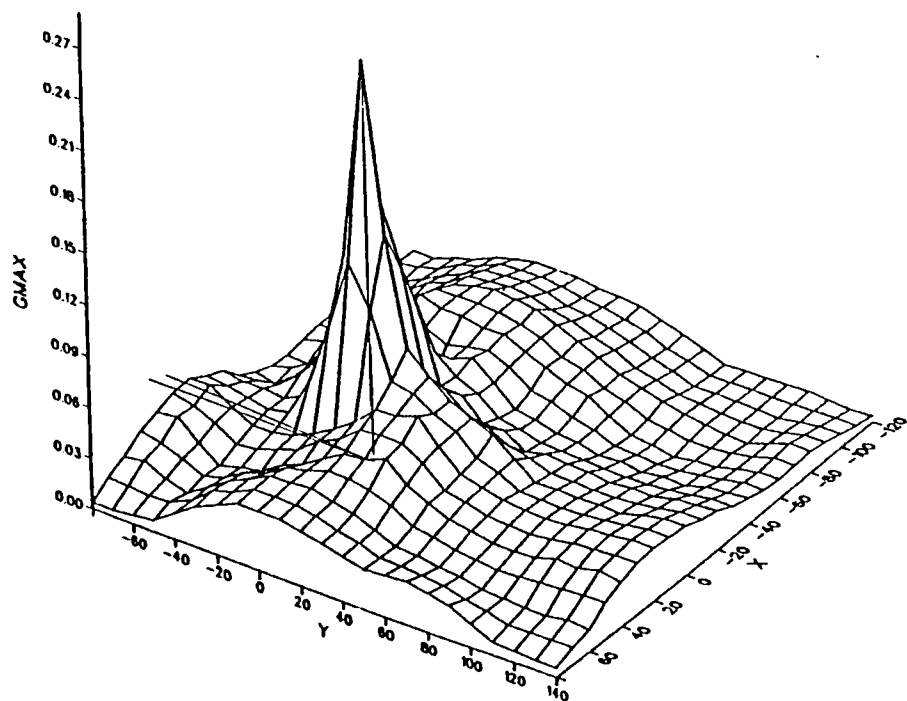
FIGURE 21. A CROSS SECTION THROUGH THE RESIDUAL STRESS FIELD OF FIGURE 19 SHOWING THE STRESSES DIRECTLY AHEAD OF THE CRACK TIP CAUSED BY THE APPLICATION OF THE OVERLOAD CYCLE.



(a)



(b)



(c)

FIGURE 22. COMPARISON OF THE MAXIMUM SHEAR STRAINS RESULTING FROM EACH OF THE OVERLOAD CYCLES ANALYZED. (a) $OLR^* = 2.15$, (b) $OLR^* = 2.85$, and (c) $OLR^* = 3.0$.

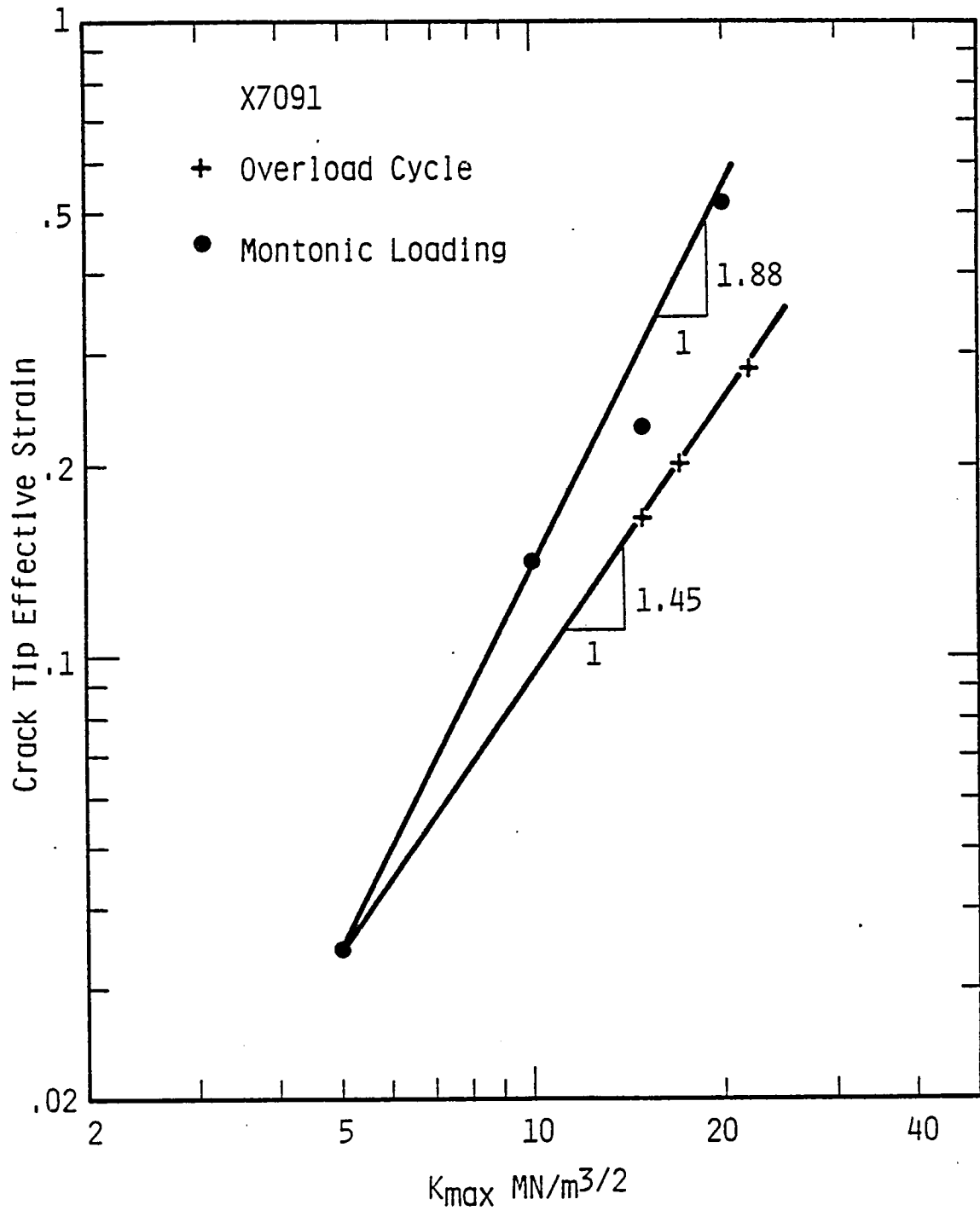


FIGURE 23. COMPARISON OF THE EFFECTIVE STRAIN AT THE CRACK TIP CAUSED BY THE OVERLOAD CYCLE WITH THE STRAIN CAUSED BY MONOTONICALLY LOADING A CRACK FROM $\Delta K = 5$ MN/m^{3/2}.

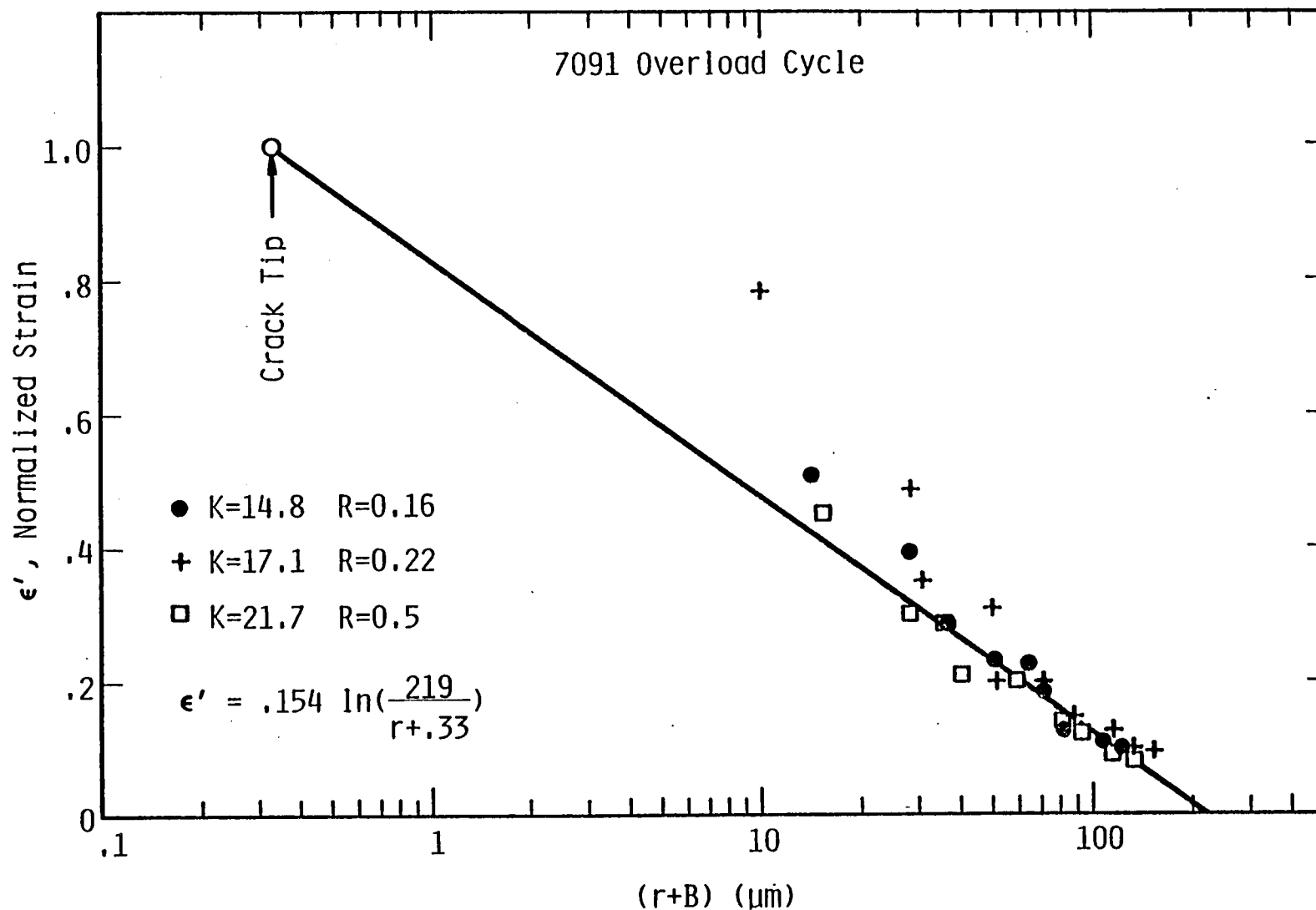


FIGURE 24. OVERLOAD CYCLE EFFECTIVE STRAINS AHEAD OF THE CRACK TIP, AS NORMALIZED BY THE CRACK TIP STRAIN. The horizontal axis is the adjusted distance parameter $(r+B)$. The line shown represents the equation shown in the figure. The fact that one equation fits all data is one indication that similitude exists between all three crack tips on the overload cycle.

from all three may be described by the following function:

$$\epsilon'(r) = 1.54 \ln\left(\frac{219}{r+B}\right) \quad (2)$$

where $\epsilon'(r)$ = strain at the distance r , normalized by the crack-tip strain. The constant $B = 0.33$ and limits the strain to a finite value at the crack tip ($r = 0$). This result may be compared to a similar analysis of strains for monotonic loading, Figure 25. For this case, the function shown on the figure appears to describe the strains in the near-tip region, but not in the far-field region.

A comparison of results from Figures 24 and 25 suggests that differences occur in the strain distribution within the plastic zone for fatigue cracks which are overloaded and cracks which are monotonically loaded.

3.2.2 Cyclic Loading Strains

The similarity of strain distributions ahead of the crack tip before and after the load excursion is examined in Figure 26. Although there is considerable scatter in the data, it is concluded that similitude is demonstrated by the crack-tip strain fields, and that it is not altered by the load excursion. This conclusion is further strengthened by the correlation of crack-tip strains and opening displacements, Figure 27. The cyclic data fall mostly along the same line, but the monotonic tension and overload cycle data do not.

3.2.3 Plastic Zone Size Ahead of Crack Tip

The functions which describe the strain distributions ahead of the crack tip are summarized in Table 2. There is obviously not much commonality between the three loading conditions. Apparently, loading history is important in determining the strain distribution ahead of a crack tip. Use of the normalized strain functions to determine plastic zone size for an overload from the monotonic results would, therefore, lead to a large error. Plastic zone sizes before, during, and after the load excursions have been derived from the relevant strain distributions and are listed in Table 3. As expected, the plastic zone size for the

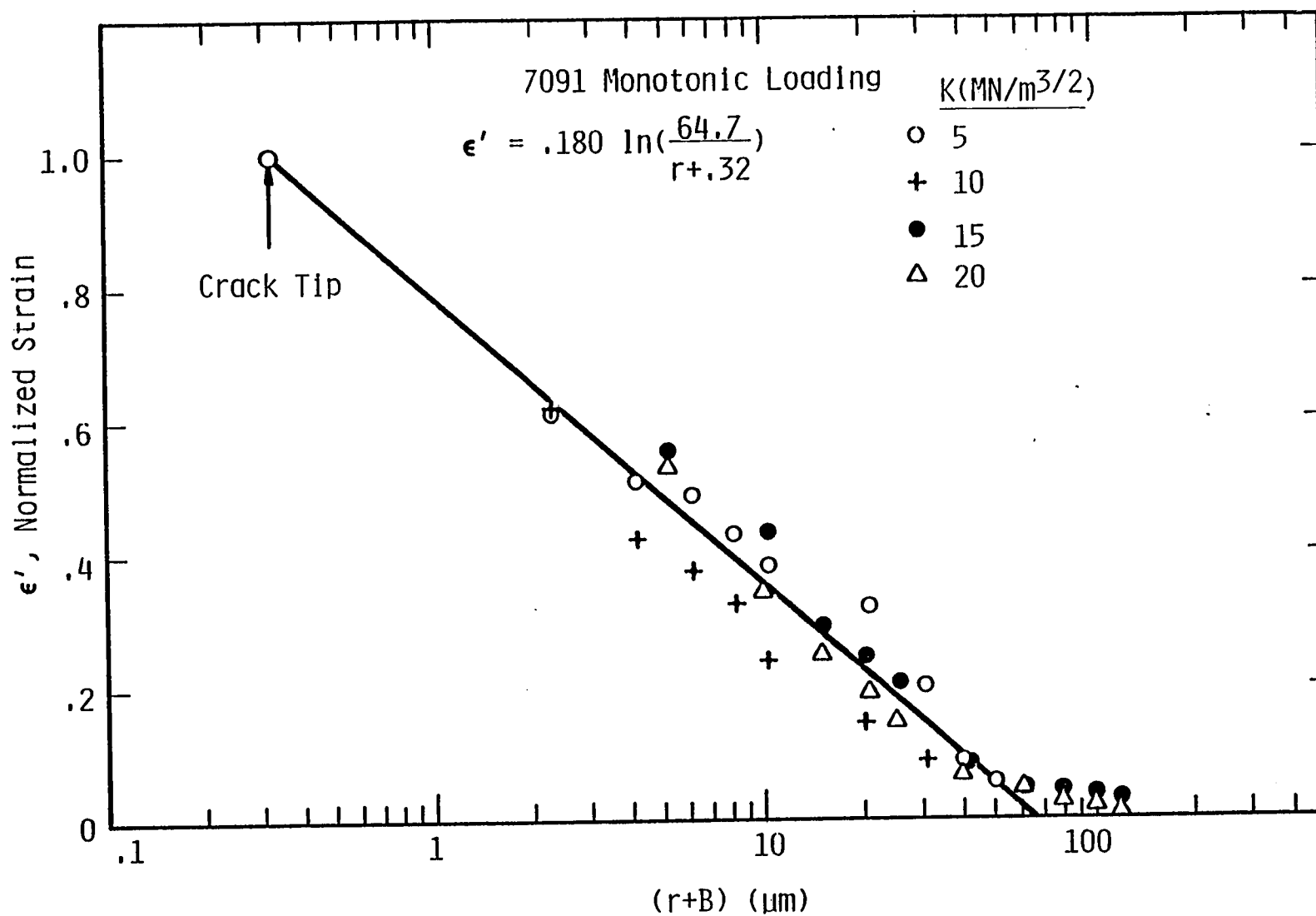


FIGURE 25. MONOTONIC LOADING NORMALIZED EFFECTIVE STRAIN VS ADJUSTED DISTANCE PARAMETER. The line shown fairly well represents the data, except at high values of K and at distances exceeding about 70 micrometers. Comparison with Figure 24 indicates a clear difference.

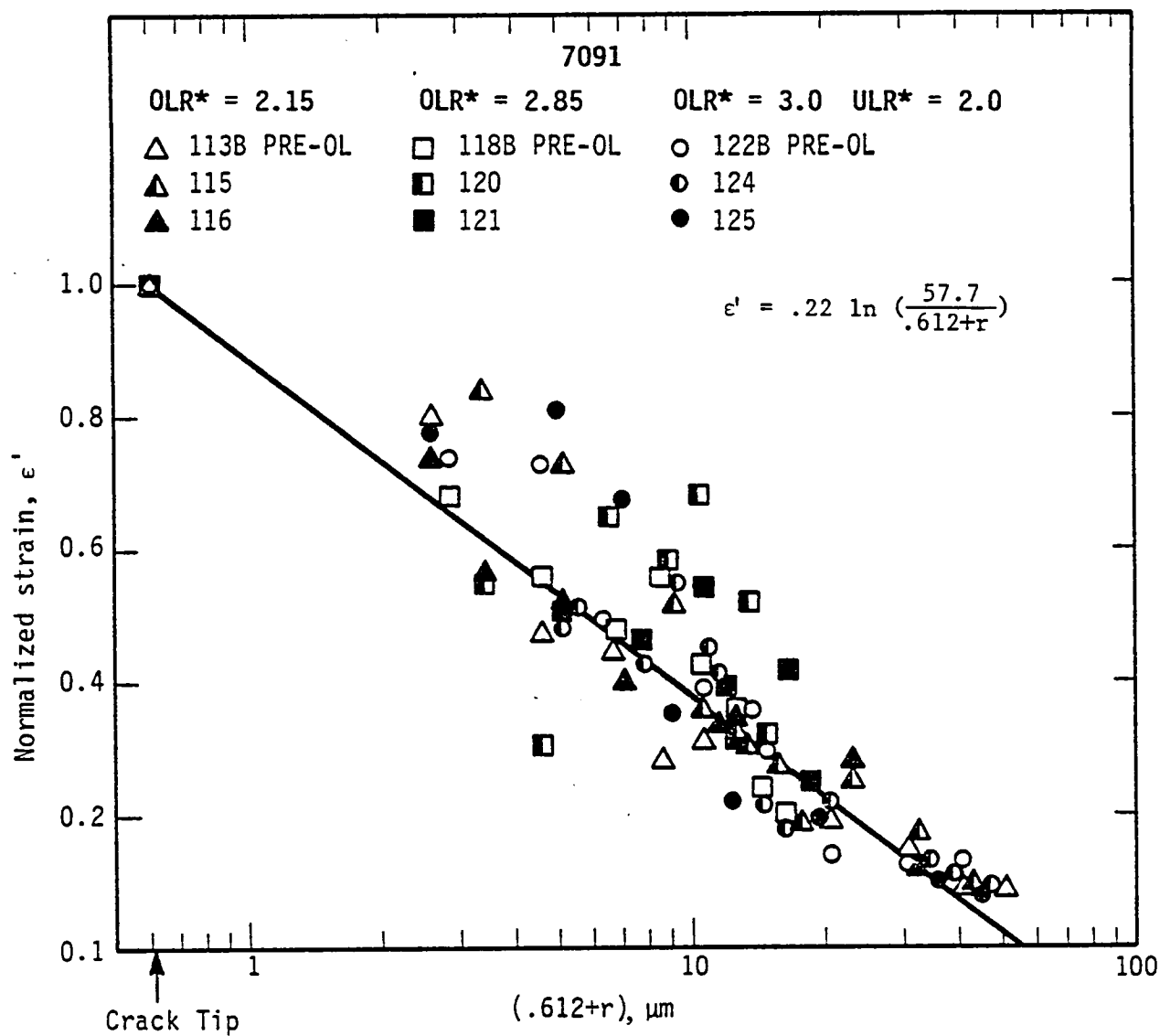


FIGURE 26. COMPARISON OF THE EFFECTIVE STRAIN DISTRIBUTIONS BEFORE AND AFTER THE OVERLOAD CYCLE FOR THE THREE OVERLOADS ANALYZED. Similitude appears to be approximately preserved in spite of the presence of the overload residual stress field.

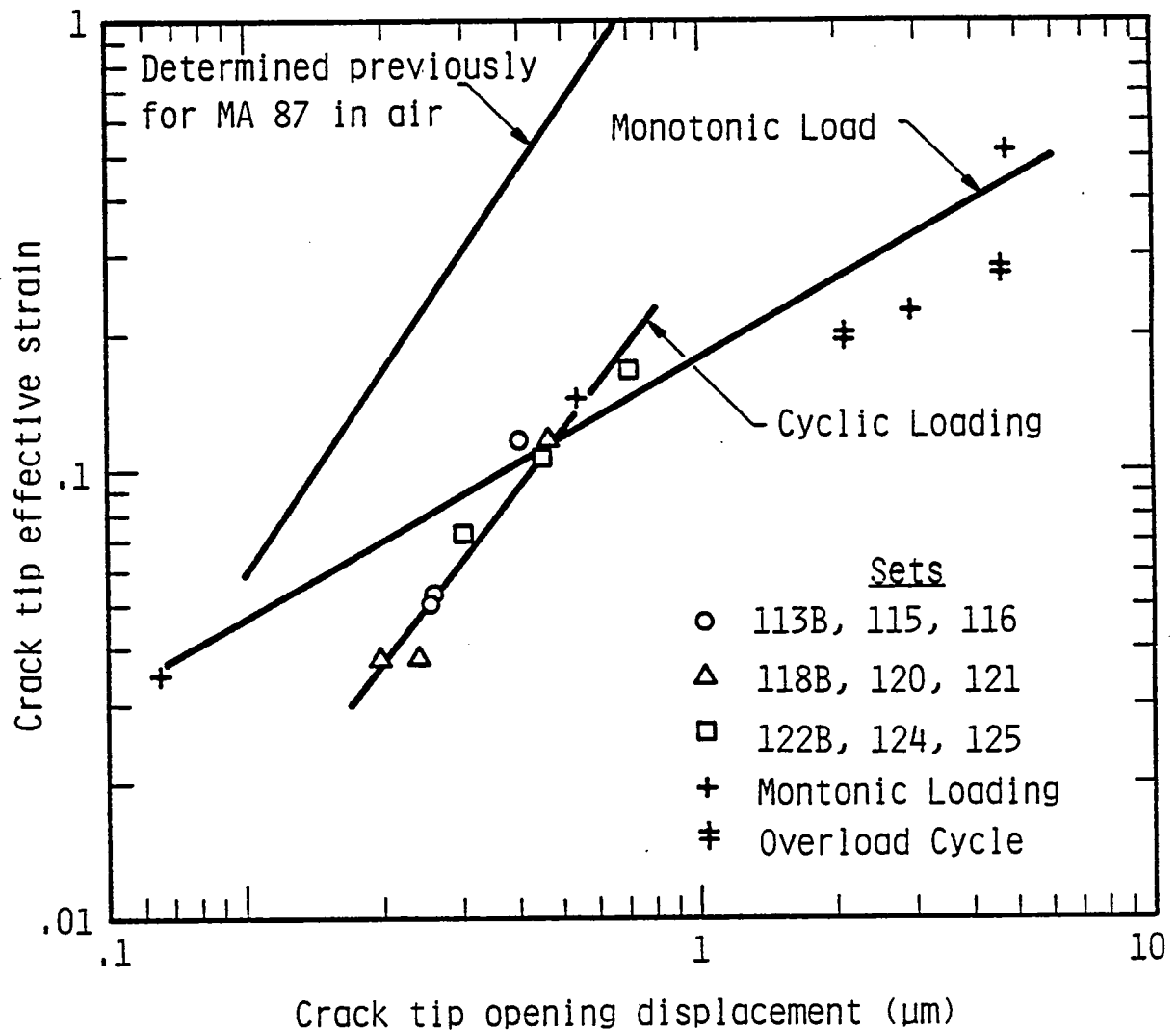


FIGURE 27. CRACK TIP OPENING DISPLACEMENT COMPARED WITH CRACK TIP EFFECTIVE STRAIN FOR CYCLIC, OVERLOAD CYCLE AND MONOTONIC LOADING. Also shown is data previously determined for a similar alloy. Crack tip opening displacement is defined at a distance of one micrometer behind the crack tip.

TABLE 2
EQUATIONS FOR NORMALIZED STRAIN AHEAD OF CRACK TIP
r in μm

<u>Loading</u>	<u>Equation</u>
Cyclic	$\epsilon' = .22 \ln \left(\frac{57.7}{r+.612} \right)$
Overload cycle	$\epsilon' = .154 \ln \left(\frac{219}{r+.33} \right)$
Monotonic	$\epsilon' = .180 \ln \left(\frac{64.7}{r+.32} \right)$

TABLE 3
DISTANCE AHEAD OF CRACK TO ELASTIC STRAIN BOUNDARY
(Plastic Zone Size)

Experiment 1: $\text{OLR}^* = 2.15$, $\text{ULR}^* = 1$, $R = .16$

Set	Crack	ΔK	r (μm)
113B	Before	6.2	42.8
114A	OL	14.8	164
115		6.2	29.3
116		6.2	30.0

Experiment 2: $\text{OLR}^* = 2.85$, $\text{ULR}^* = 1$, $R = .22$

118B	Before	6	55.5
119A	OL	17.1	172
120		6	23.7
121		6	15.5

Experiment 3: $\text{OLR}^* = 3$, $\text{ULR}^* = 2$, $R = .5$

122B	Before	7.2	46.6
123A	OL	21.7	190
124		7.2	35.8
125		7.2	41.9

overload cycle is larger than that for the pre-overload cycle, and the latter is larger than for cracks in the overload-affected period.

3.2.4 Correlation Between Crack Growth Rates and Crack-Tip Strains

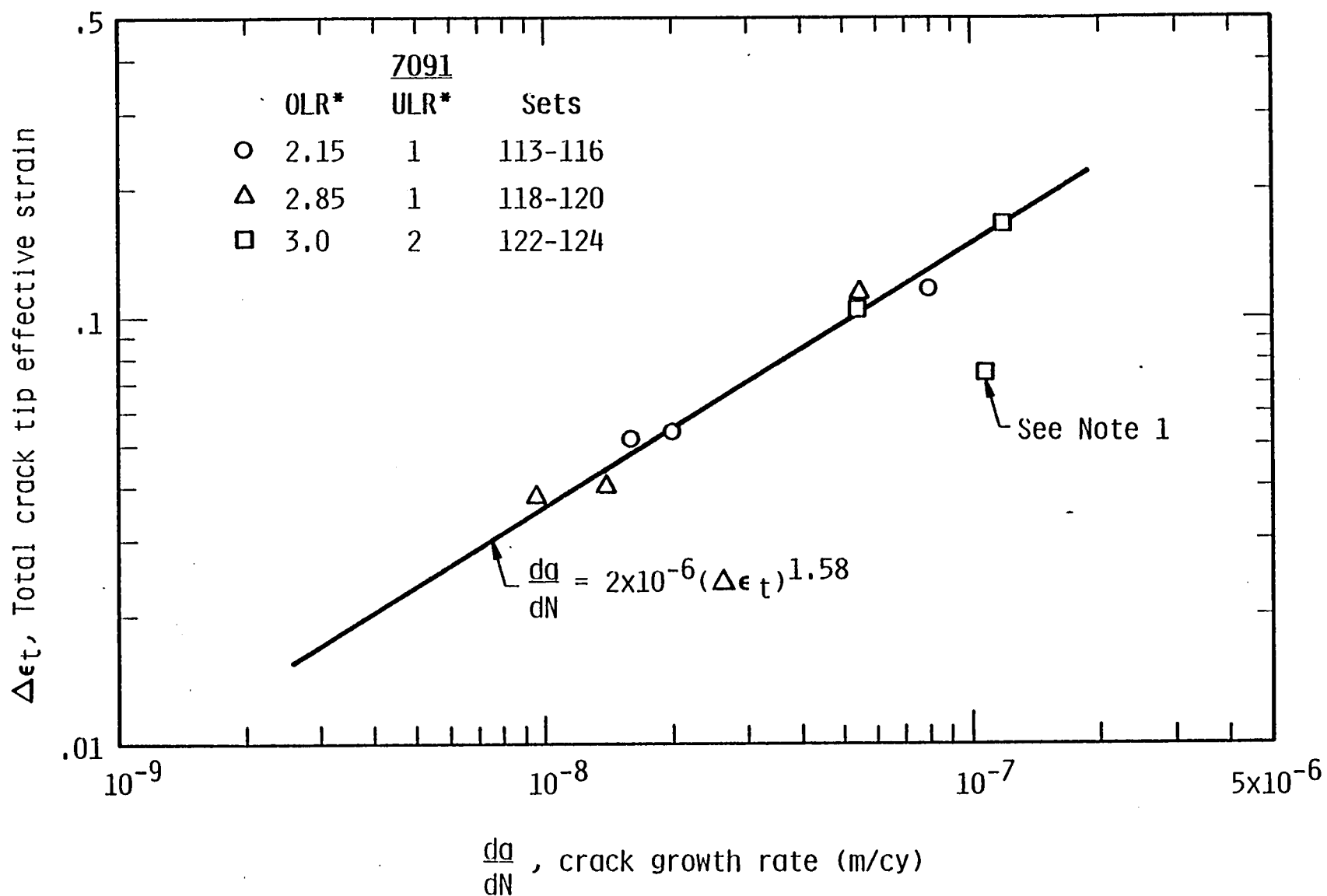
The relationship between total crack-tip strain range and crack growth rate has been examined, Figure 28, for cracks growing before and after the load excursion. With one exception, which was explained, the correlation was excellent. Note that the results also correlate well with the severity of the load excursion.

This result is another indication that similitude is satisfied after application of the load excursion. Similar conclusions were drawn from the results of Figures 26 and 27. Since the crack is responding in a predictable way, this indicates again that it is the driving force which is unknown subsequent to the load excursion.

3.2.5 Residual Stresses from the Load Excursion

Stress changes computed from the strain changes measured at each step in the load excursion are shown in Figures 29, 30, and 31, where, as indicated in Table 1, the "A" refers to the overload-loading part of the cycle and "B" refers to the overload-unloading subcycle. For the overload/underload cycle, Figure 31, "C" is the underload-unloading part of the cycle and "D" refers to the underload-reloading part. The results are about as might be expected from a knowledge of the other load excursions, except for the underload-unloading part of the cycle, Figure 31(d), where the stresses are more inhomogeneous than in the rest of the load excursion.

The summed stresses, adjusted to a reference of zero stress, as outlined in the first section, are shown in Figures 32, 33, and 34. These are the residual stresses in the axis of the loading (σ_x). Figures 32 and 33 should be compared with Figure 19. Note that the overload from $R = 0.5$ is treated both before and after the subsequent underload. The three overloads yield similar results, although Figure 19 exhibits more inhomogeneity than the other two. A cross section through the residual stress field is shown along the crack direction in Figure 35, which should be compared with Figure 21.



Note 1: Crack growth rate averaged over 100 μm . Growth rate at the time of measurement of crack tip strain was probably less.

FIGURE 28. CORRELATION OF CRACK TIP STRAIN WITH CRACK GROWTH RATE.

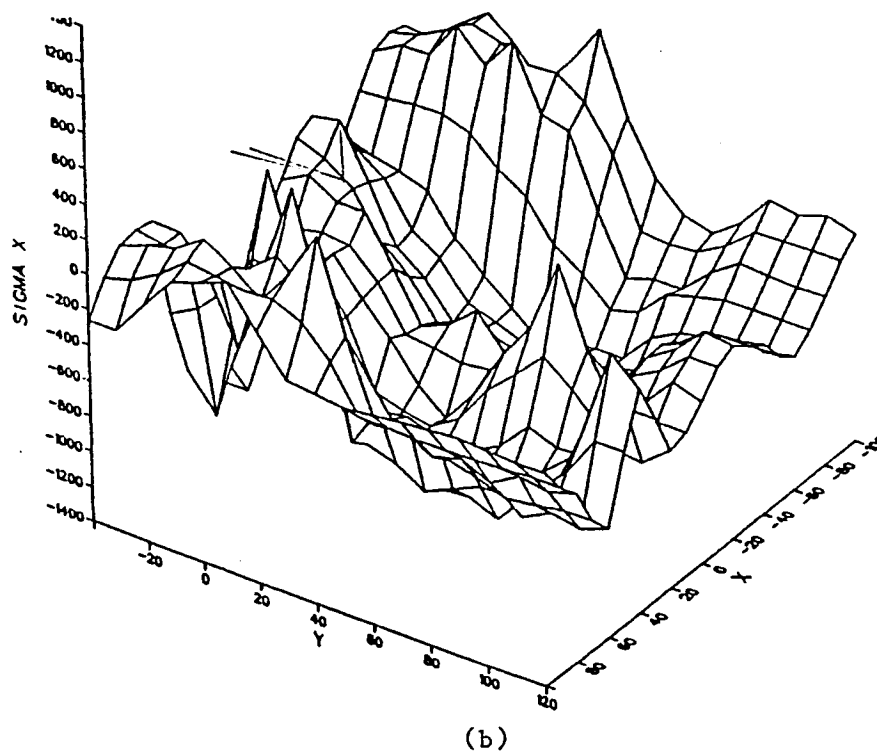
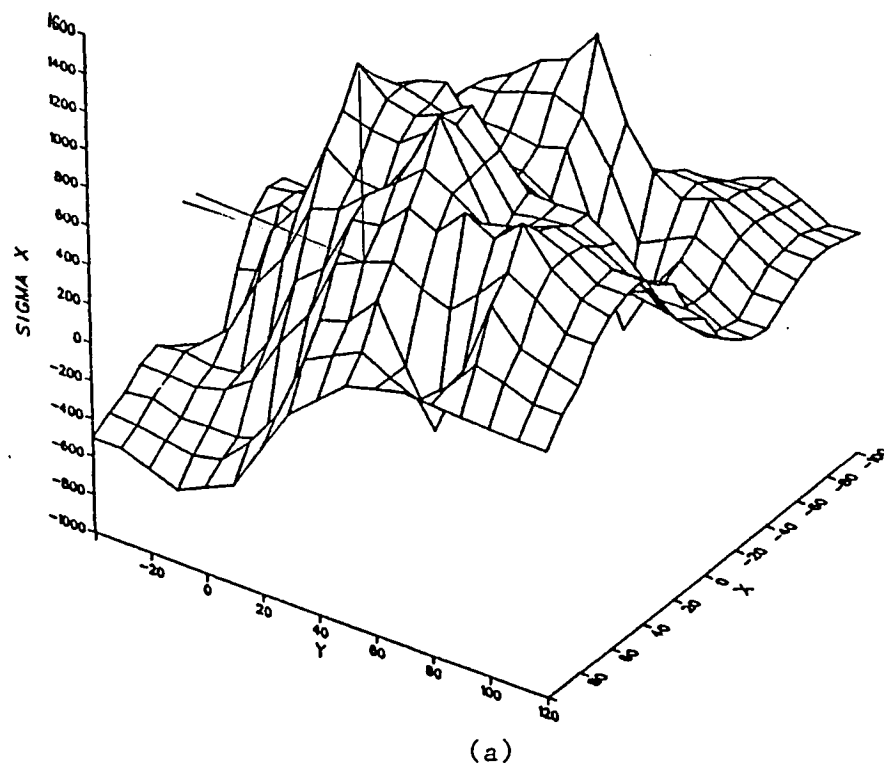
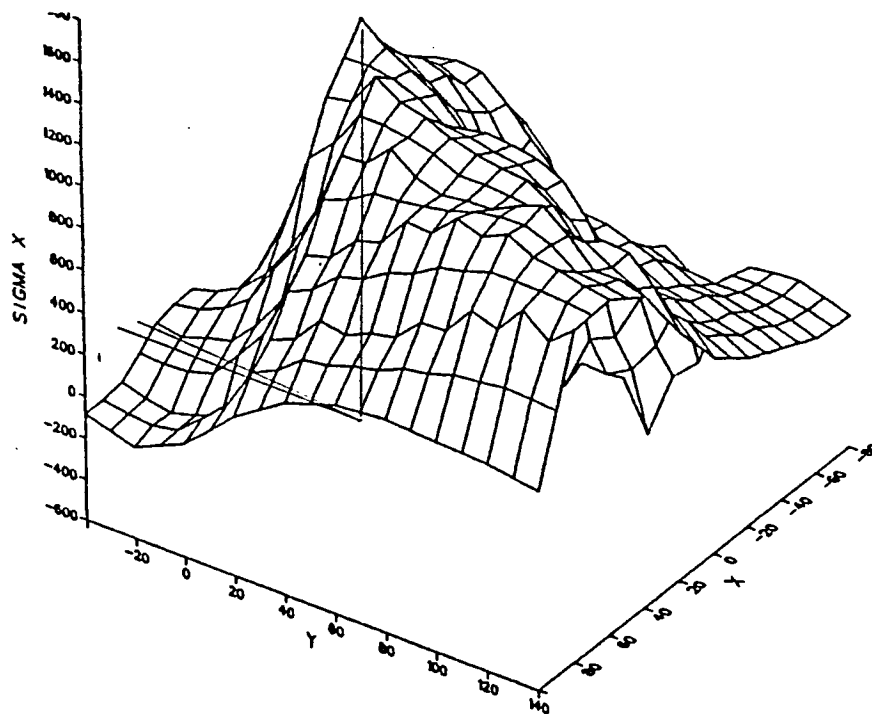
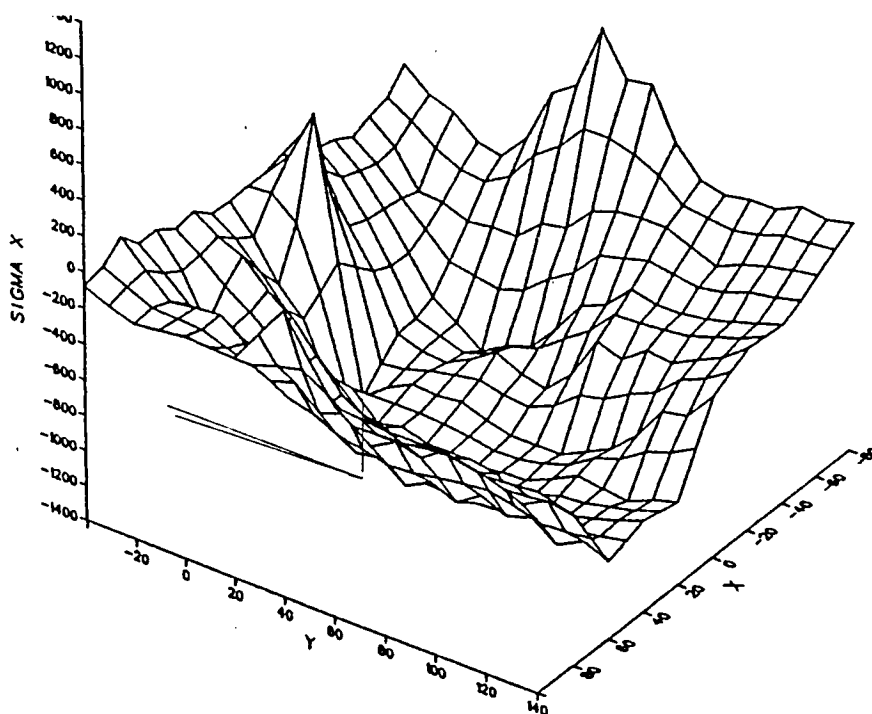


FIGURE 29. (a) STRESSES ON THE LOADING PORTION OF THE OVERLOAD CYCLE AND (b) ON THE UNLOADING PORTION OF THE OVERLOAD CYCLE IN THE AXIS OF THE LOAD APPLICATION, $\text{OLR}^* = 2.15$.

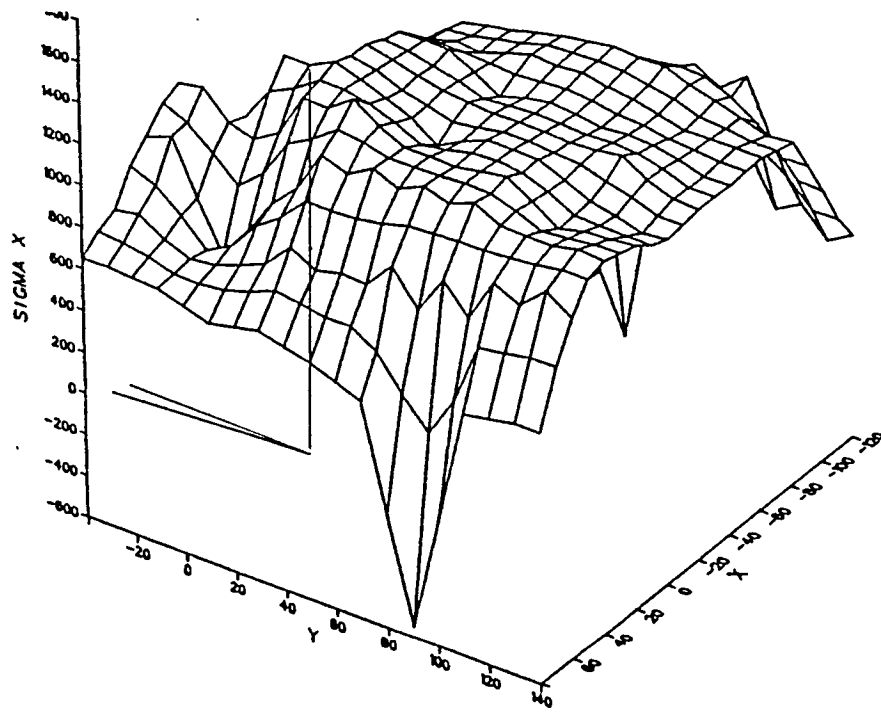


(a)

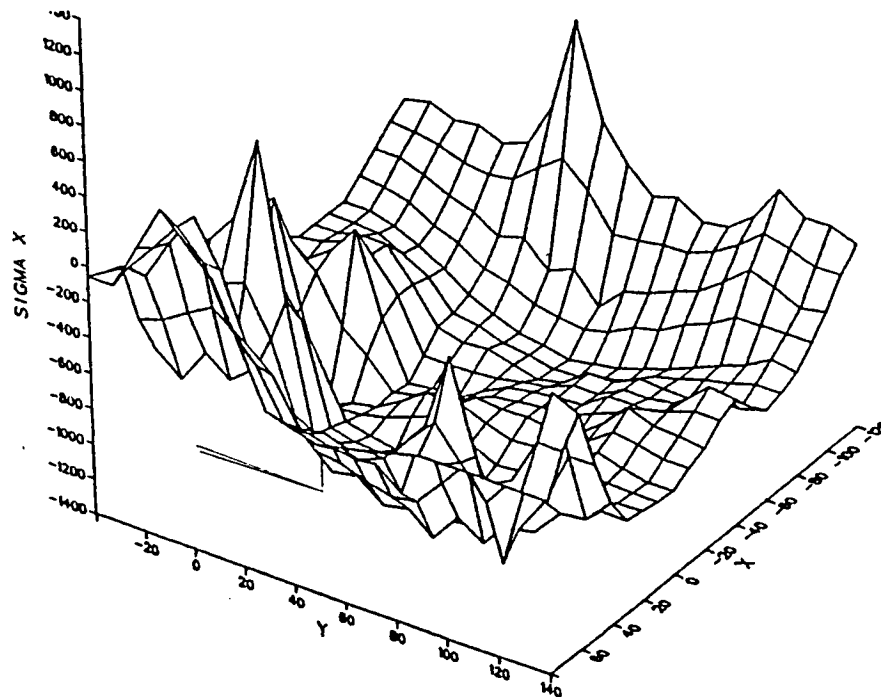


(b)

FIGURE 30. (a) STRESSES ON THE LOADING PORTION OF THE OVERLOAD CYCLE AND (b) ON THE UNLOADING PORTION OF THE OVERLOAD CYCLE IN THE AXIS OF THE LOAD APPLICATION, $OLR^* = 2.85$.



(a)



(b)

FIGURE 31. (a) STRESSES ON THE LOADING PORTION OF THE OVERLOAD CYCLE, AND (b) ON THE UNLOADING PORTION OF THE OVERLOAD CYCLE. All stresses are in the axis of load application. $OLR^* = 3.0$.

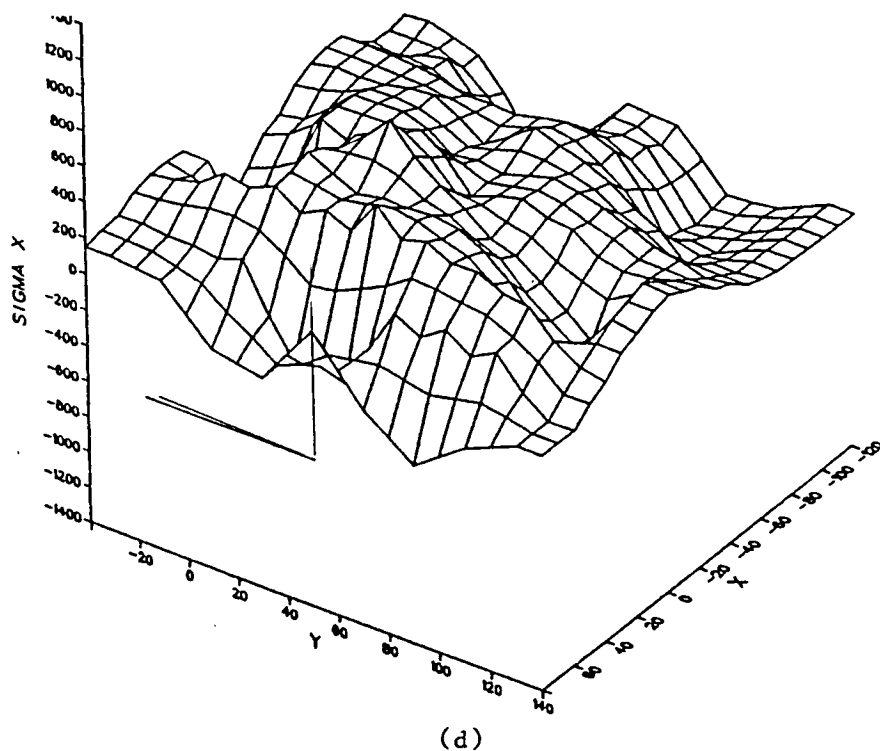
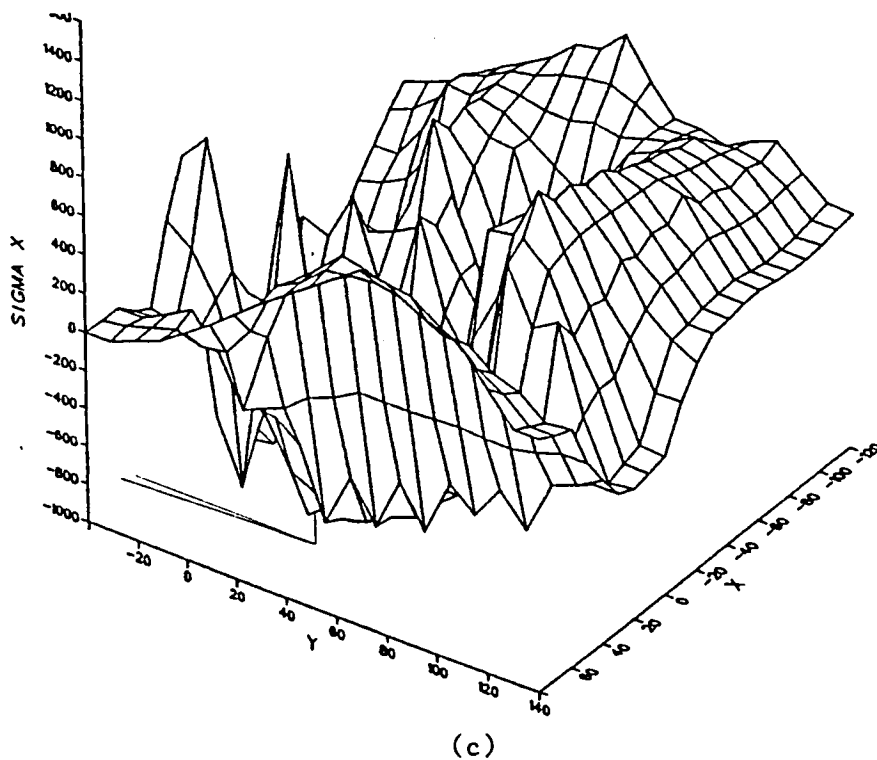


FIGURE 31 (CONTINUED). (c) STRESSES ON THE RELOADING PORTION OF THE UNDERLOAD CYCLE, AND (d) ON THE RELOADING PORTION OF THE UNDERLOAD CYCLE. All stresses are in the axis of load application. $ULR^* = 2.0$.

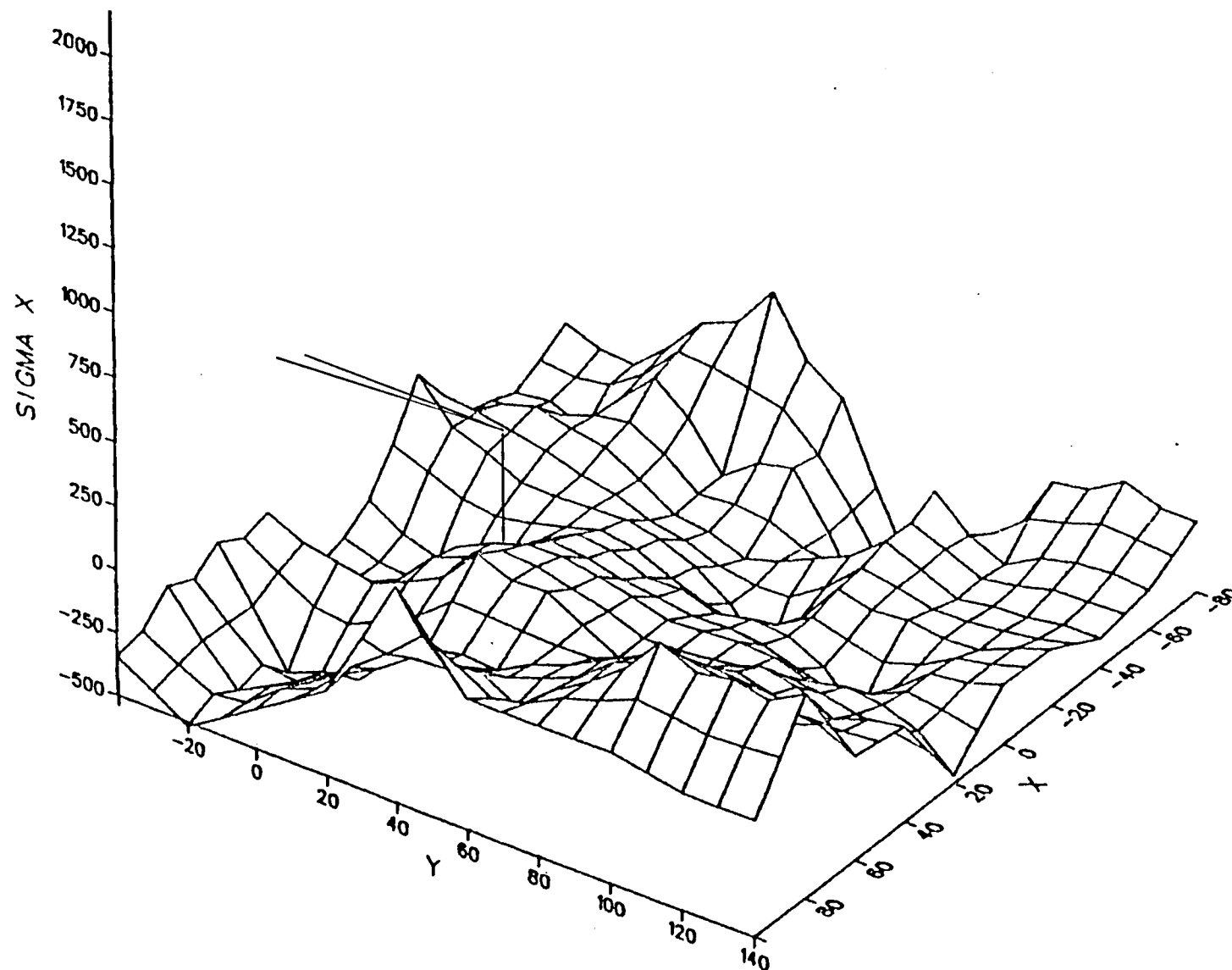


FIGURE 32. RESIDUAL STRESS FIELD IN THE DIRECTION OF LOADING CAUSED BY THE $OLR^* = 2.85$. This figure should be compared to Figure 19 ($OLR^* = 2.15$).

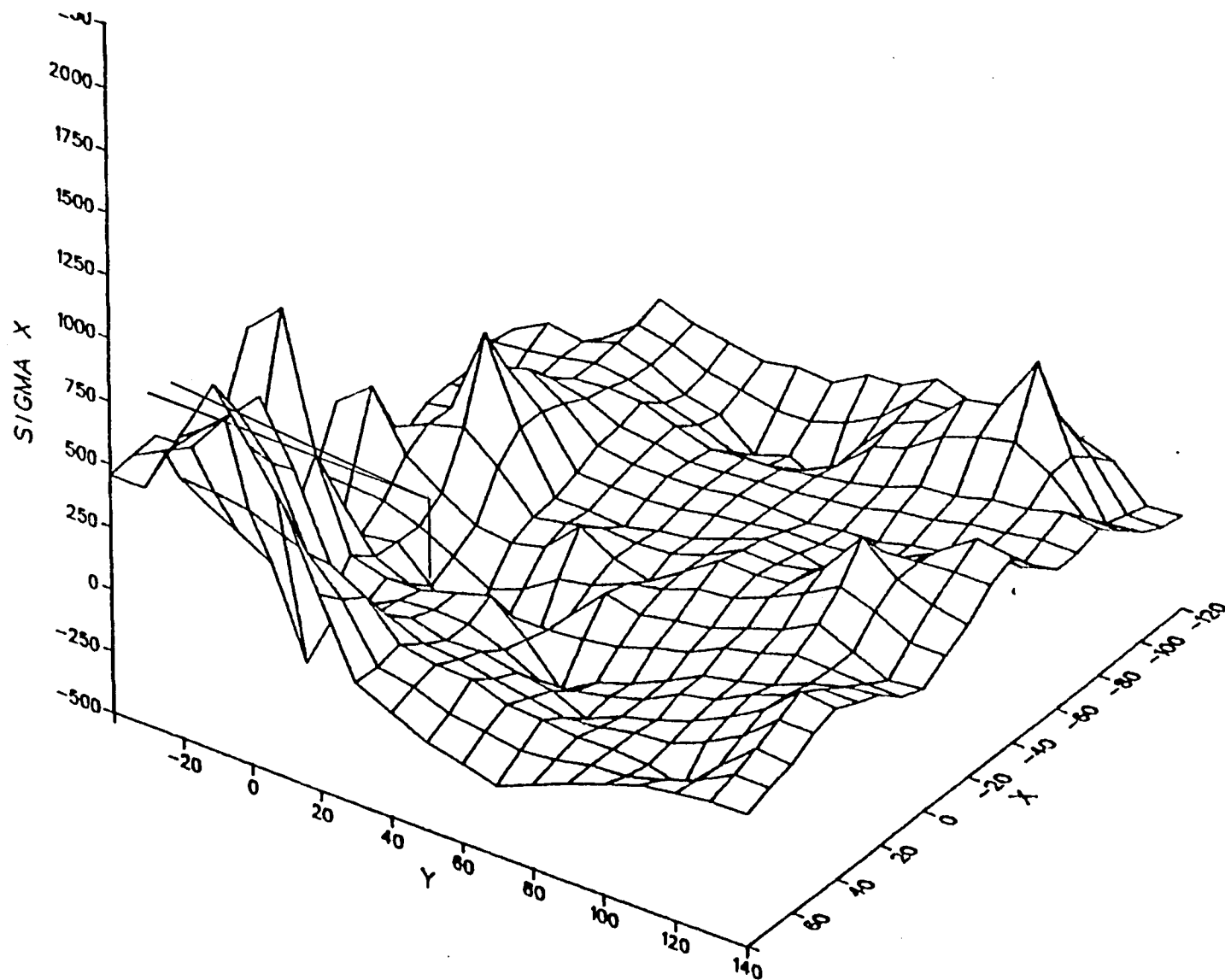


FIGURE 33. RESIDUAL STRESS FIELD IN THE DIRECTION OF LOADING CAUSED BY THE $OLR^* = 3.0$. This figure should be compared with Figures 19 and 32. Note that the crack was not subsequently grown through this condition, but was followed by an underload.

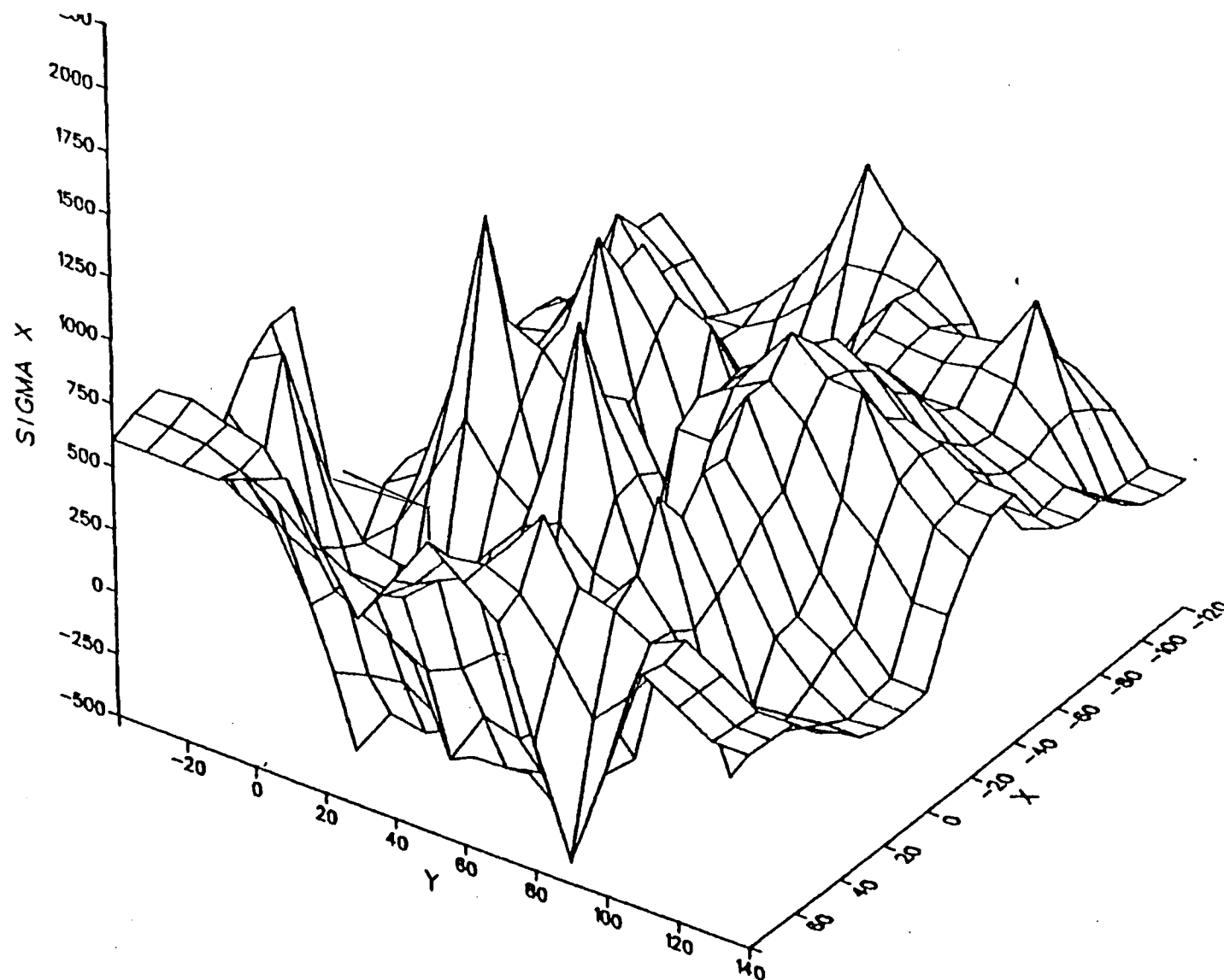


FIGURE 34. RESIDUAL STRESS FIELD IN THE DIRECTION OF LOADING CAUSED BY THE $OLR^* = 3.0$ FOLLOWED BY THE $ULR^* = 2.0$. Compare with Figure 33.

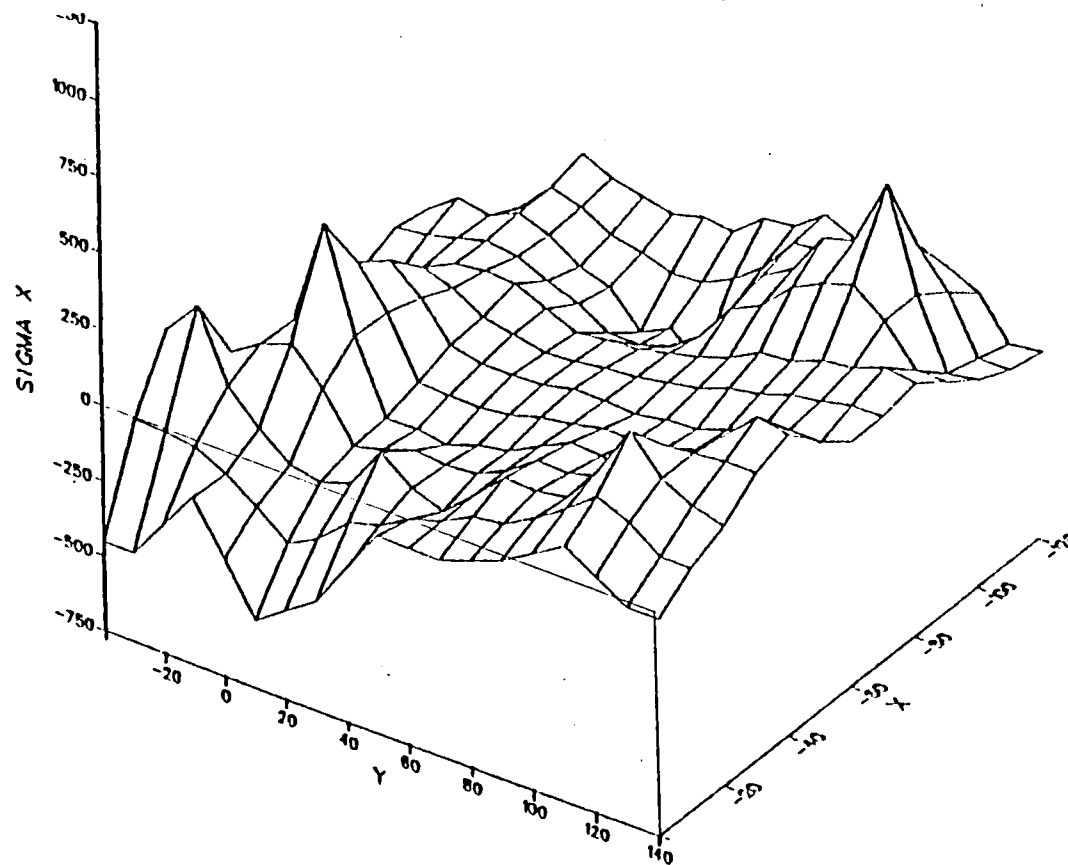


FIGURE 35. RESIDUAL STRESS DISTRIBUTION WITHIN HALF OF THE CRACK TIP PLASTIC ZONE FOR $OLR^* = 3.0$ AND $R = 0.5$. The section along $X = 0$ shows the profile of residual stresses normal to the crack whose tip is at $Y = 0$. Both X and Y are in μm and $SIGMA X$ is in MPa.

The residual effective stresses appear similar to the residual stresses in the loading axis, Figures 36, 37, and 38. These should also be compared to Figure 20.

The residual stresses of Figure 34 or 37, which are a result of the overload/underload, show both tensile and compressive stresses, resulting in a very inhomogeneous residual stress field, but one which has a nearly zero net change in stress averaged over the plastic zone. This small magnitude of residual stress is reflected in the small change in crack growth rates as the crack moves through the residual plastic zone.

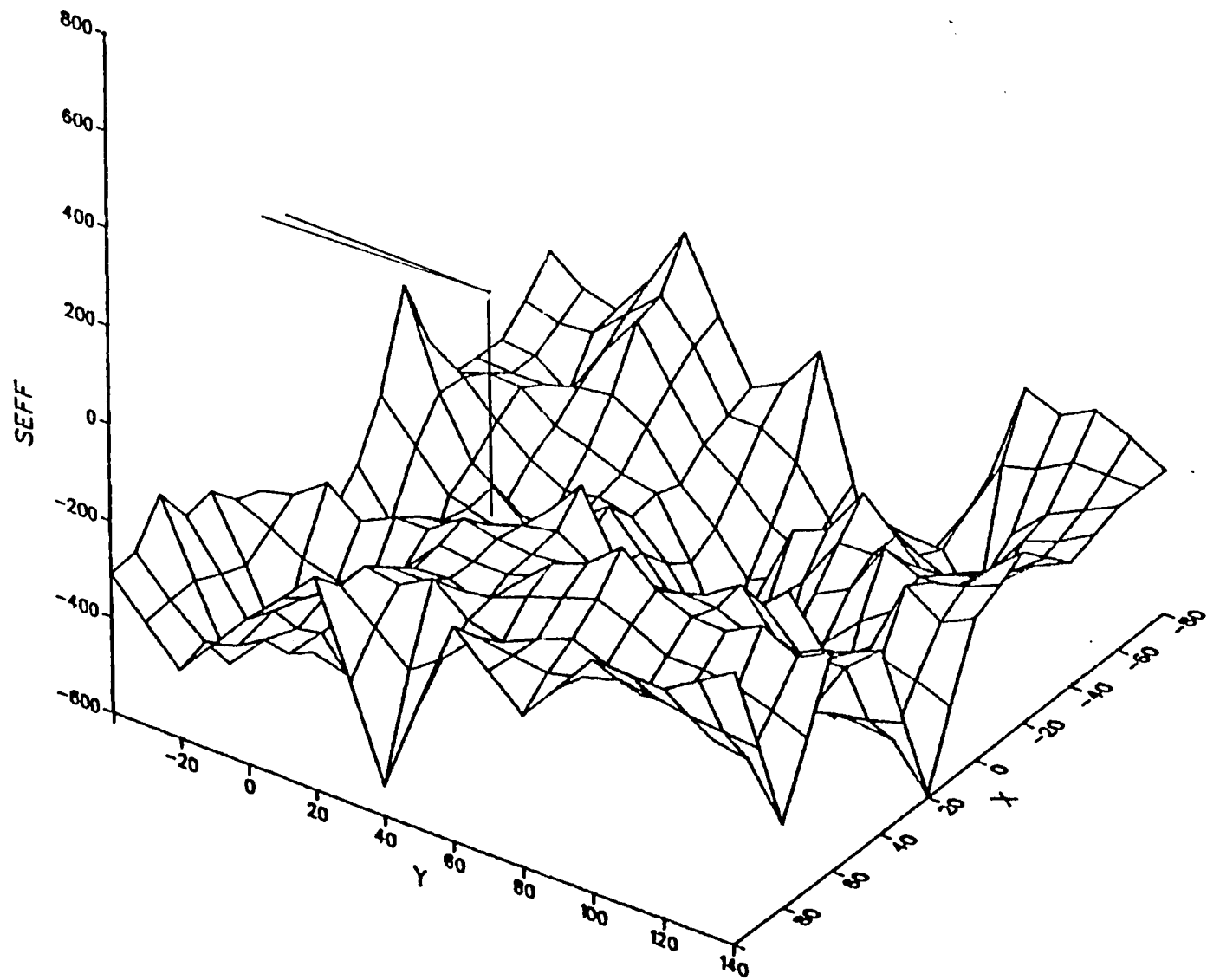


FIGURE 36. RESIDUAL EFFECTIVE STRESS FIELD FOR $OLR^* = 2.85$. Compare with Figure 20.

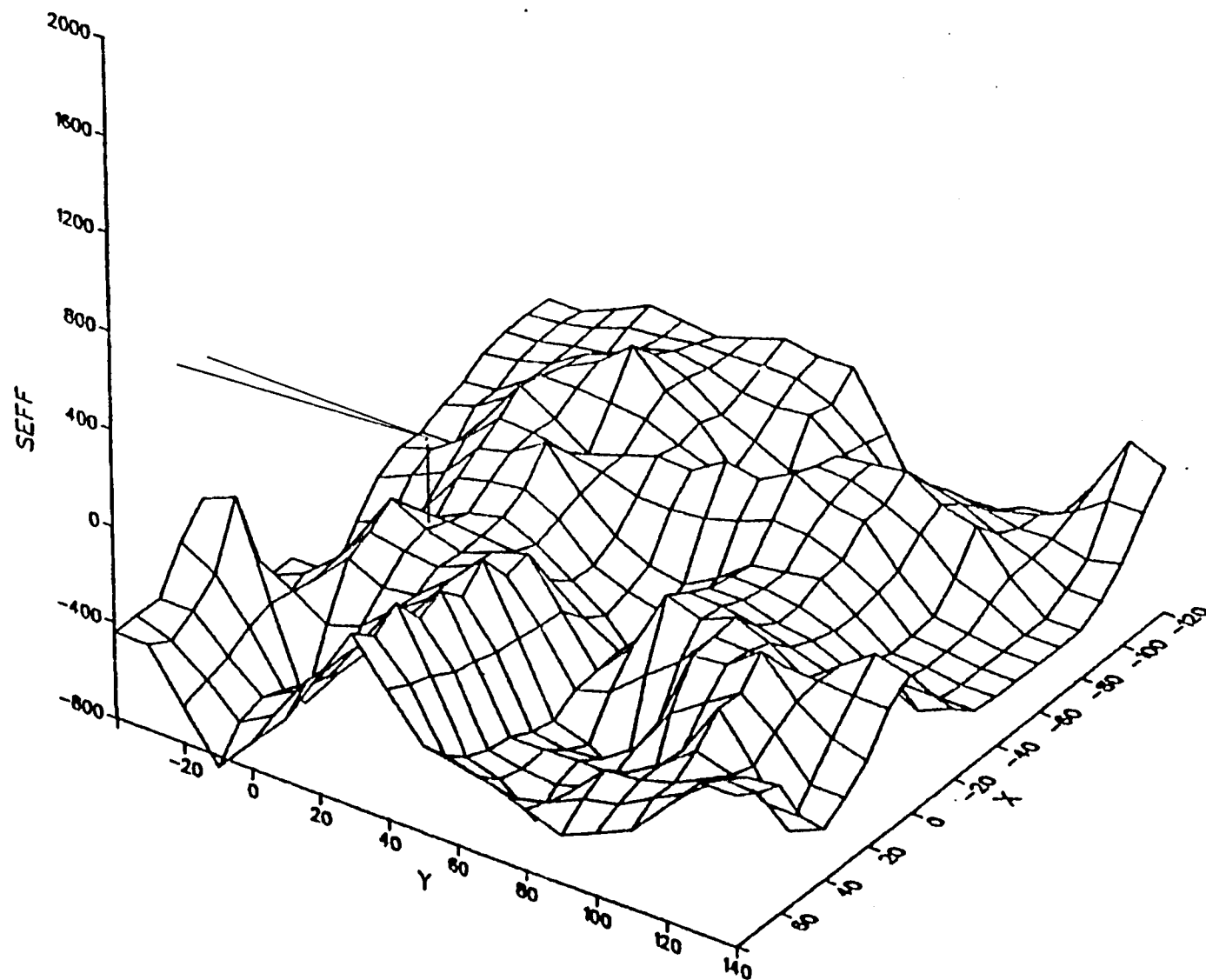


FIGURE 37. RESIDUAL EFFECTIVE STRESS FIELD FOR $OLR^* = 3.0$. Compare with Figures 20 and 35.

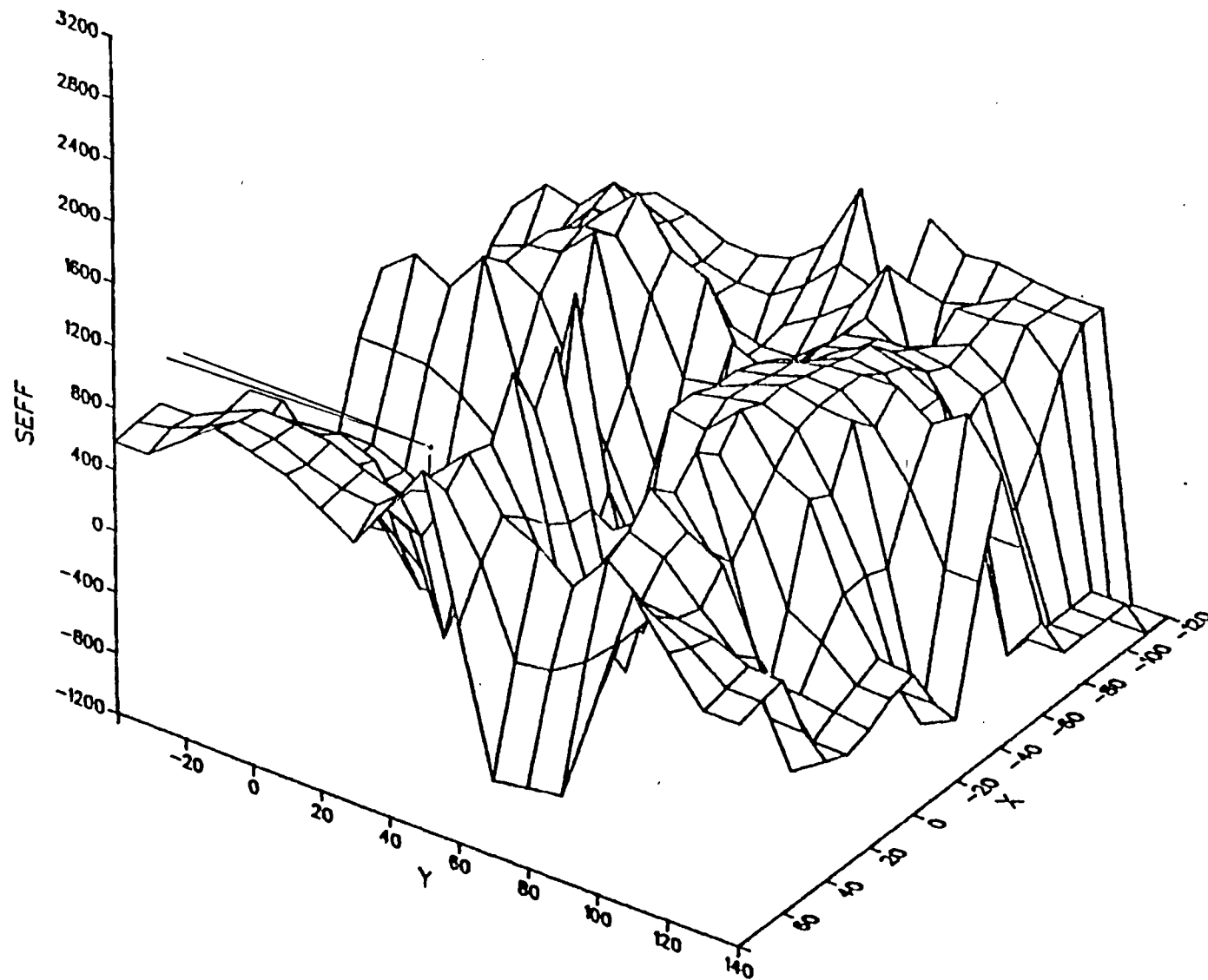


FIGURE 38. RESIDUAL EFFECTIVE STRESS FIELD FOR $OLR^* = 3.0$ AND $ULR^* = 2.0$. Compare with Figures 34 and 36.

4.0 ANALYSIS OF SELECTED EXPERIMENTS WITH THE PLASTIC WAKE MODEL (FAST-2)

Three experiments involving either a single overload or an overload/underload sequence were selected for detailed analysis with Newman's plastic wake closure model (FAST-2) [7]. Two of these experiments (shown in Figure 7), designated Experiments 1 and 3, have been previously discussed in the detailed plasticity analysis of Section 3.0. One other experiment, designated Experiment 4, was also modeled. Table 4 shows the data characterizing these experiments.

TABLE 4
LOADING VARIABLES FOR EXPERIMENTS ANALYZED WITH FAST-2
 $\Delta K = 7 \text{ MPa}\sqrt{\text{m}}$

Experiment No.	OLR*	ULR*	R
1	2.15	1.0	0.1
3	3.0	2.0	0.5
4	3.0	1.0	0.5

The sensitivity of the analysis to variations in the degree of constraint and to variations in constant-amplitude fatigue crack growth properties were examined. The model was evaluated by comparing analytical predictions with experimental measurements. Specifically, the following quantities were compared for times before, during, and after the load excursions:

- Crack opening stress, expressed as the effective load ratio ($R_{\text{eff}} = P_o/P_{\text{max}}$)
- Crack extension (Δa)
- Crack growth rate (da/dN)
- Number of delay cycles (N_D)

The shape of the overload-affected da/dN versus Δa curve, as well as crack-tip residual stresses were also examined.

4.1 Influence of Crack Growth Rate Properties on Analytical Predictions

The FAST-2 model computes ΔK_{eff} for each cycle, or block of cycles, and then integrates the crack growth rate properties, da/dN as a function of ΔK_{eff} , to obtain da/dN versus Δa . A procedure which may be used to obtain the fatigue crack growth rate properties in terms of ΔK_{eff} is described in Reference 7. This procedure involves using the closure model to analyze the test specimen from which the crack growth rate data are obtained thereby computing ΔK_{eff} for each ΔK and R value. Growth rate data at several values of R should in theory collapse into a single curve if da/dN is plotted vs ΔK_{eff} .

For crack growth rate data obtained at high- R , little or no crack closure should occur; therefore, ΔK_{eff} should be nearly equal to ΔK . Thus, the single curve which represents da/dN vs ΔK_{eff} for all load ratios should then be the same as the high- R da/dN vs ΔK curve. Thus, if data at high- R are available, the procedure described in Reference 7 is not necessary.

Such data were available from Alcoa from separate production lots of 7091-T7E69, as shown in Figure 39. Between Extrusions 1 and 2 (shown as dots in Figure 39) there is little variability at $R = 0.33$. The third extrusion from another lot was used at SwRI for the experiments described herein. Several crack growth rate measurements at $\Delta K \approx 6 \text{ MPa}\sqrt{\text{m}}$ and $R = 0.33$ were made at SwRI which showed agreement with Extrusions 1 and 2. However, a fourth extrusion tested by Alcoa at $R = 0.33$ shows significantly higher growth rates than Extrusions 1 and 2 at $R = 0.33$ and $\Delta K < 2 \text{ MPa}\sqrt{\text{m}}$. Therefore, there is some uncertainty as to which growth rate properties should be used in the model, particularly in the low-growth-rate regime, if predictions are to be compared with experiments.

Figure 39 also shows the range of crack growth rates covered in the overload experiments that were analyzed. Very high growth rates are obtained during the overload, and very low growth rates are obtained from subsequent retardation of the crack growth rates. Another bar on the right shows the range of crack growth rates for which constant amplitude high- R crack growth rate data were available. Note the unavailability of data above $2 \times 10^{-6} \text{ m/cycle}$; this gives rise to uncertainty as to what growth rate properties should be used in the model to predict crack extension during the overload cycles.

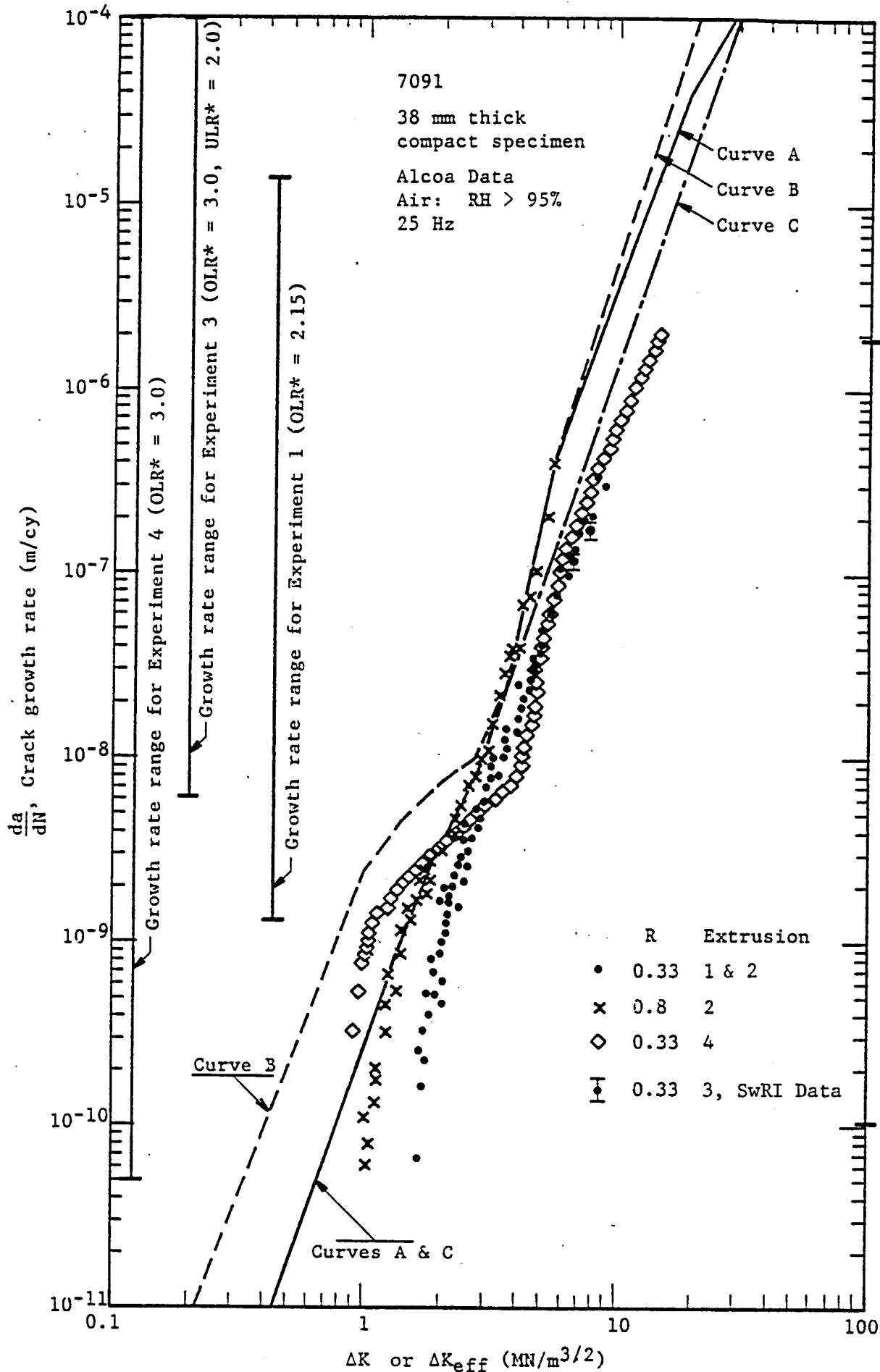


FIGURE 39. COMPARISON OF CRACK GROWTH RATE CURVES USED IN ANALYTICAL PREDICTIONS VERSUS MEASURED CRACK GROWTH RATE DATA ON 7091-T7E69 FROM SEVERAL EXTRUSIONS AND LOAD RATIOS. Data are shown plotted vs ΔK , but Curves A, B and C are vs ΔK_{eff} .

Figure 39 shows three curves which were used in the analyses to examine the effects of this uncertainty at both very high and very low growth rates. Curve C represents a power law fit to the $R = 0.8$ data for Extrusion 2 (shown as 'x's in Figure 39). Analyses performed using Curve C revealed that the increment of crack extension for the overload cycle was much less than that measured in the experiments. The high- ΔK measurements made in the overload experiments indicated that the high growth rates were better represented by Curves A or B in Figure 39.

In the low growth rate regime, Curves A and C are nearly coincident. Curve B was intended to estimate the $R = 0.8$ data for Extrusion 4. For Extrusion 2, there exists a consistent offset in ΔK at each crack growth rate between the $R = 0.8$ and $R = 0.33$ data. This offset may be thought of as the difference between ΔK and ΔK_{eff} . The particular offset at each crack growth rate was applied to the $R = 0.33$ data for Extrusion 4 to obtain the portion of Curve B for $da/dN < 7 \times 10^{-9}$ m/cycle.

The sensitivity of the analysis to differences in constant amplitude crack growth rate properties is illustrated in Figures 40 through 43. The results in Figure 40 are for Experiment 1 with a constraint factor (α) of 1.9. (This constraint factor gave optimum results for this experiment, as discussed in Section 4.2.) As indicated, the minimum growth rate is primarily affected, while the differences in delay cycles is minimal. Note that the experimental observations indicate the minimum growth rate is higher than predicted, and that the measured results recover from the minimum rate more gradually than predicted by the model.

Figure 41 makes the same comparison for Experiment 4 with $\alpha = 2.3$. (This constraint factor gave optimum results for this experiment.) Note that because a much greater range in growth rates occurred in Experiment 4, the differences in the analytical results for different growth rate curves are more significant than those of Experiment 1. Curve B gives the best prediction of the experimental results. Curve C underestimates the maximum growth rates in all cases. Unlike Experiment 1, the initial growth rate in Experiment 4 is not well predicted by Curves A or B.

Figures 42 and 43 show that the initial growth rate before the overload in Experiment 3 was also not well predicted by Curves A and B.

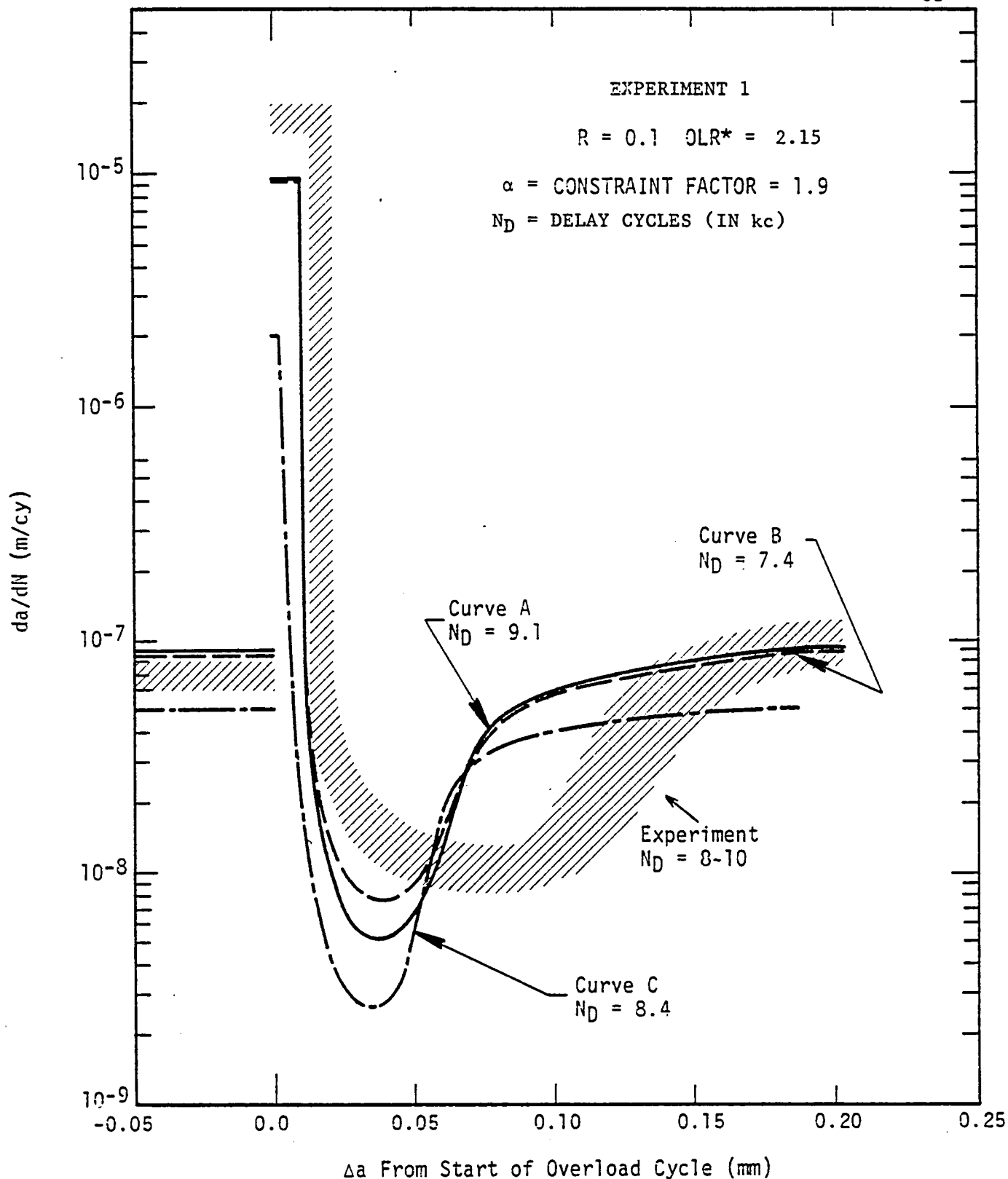


FIGURE 40. COMPARISONS OF EXPERIMENTAL RESULTS AND MODEL PREDICTIONS FOR VARIOUS CRACK GROWTH RATE CURVES. Uncertainty in experimental results is shown as the hatched region.

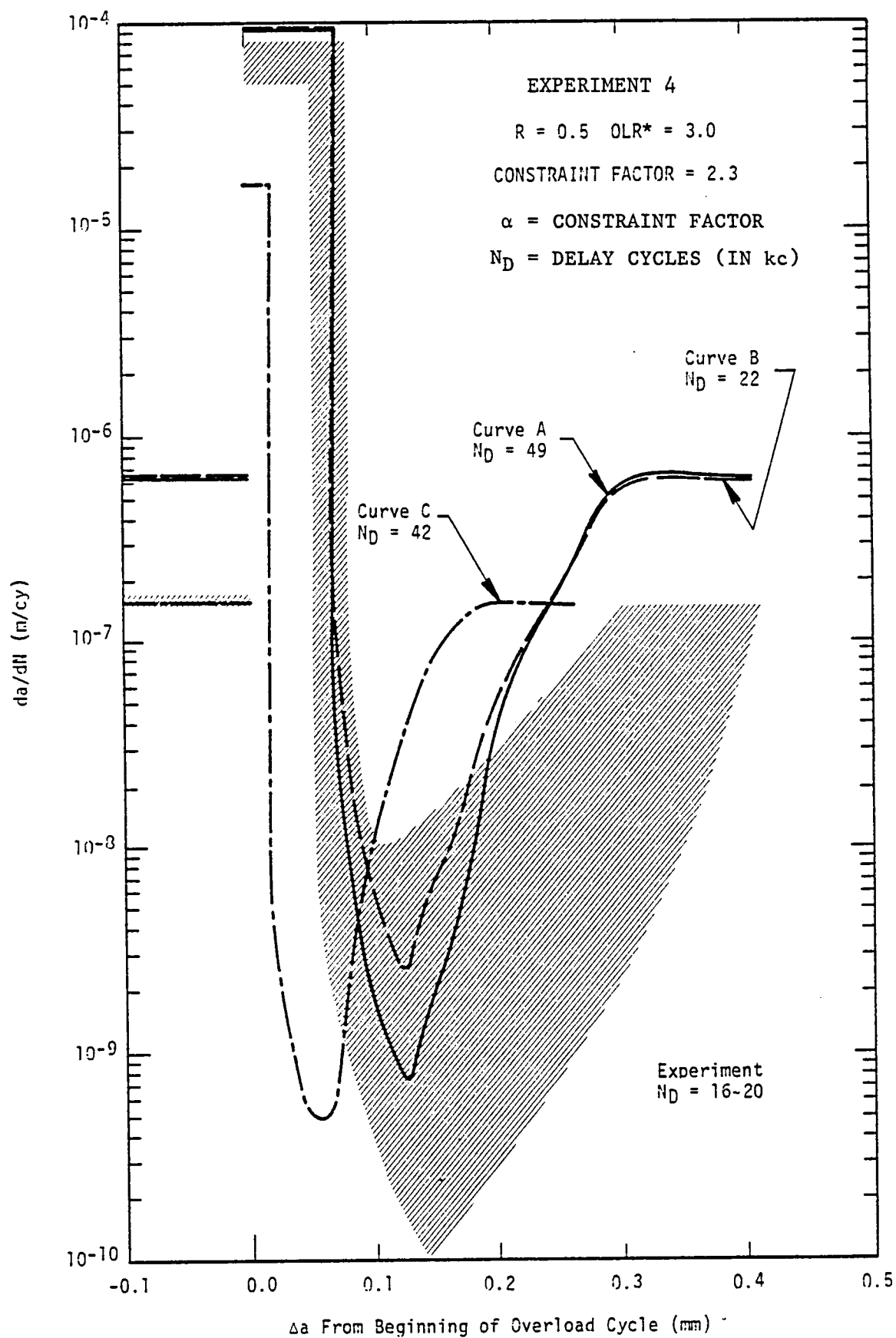


FIGURE 41. COMPARISON OF EXPERIMENTAL RESULTS AND MODEL PREDICTIONS FOR VARIOUS CRACK GROWTH RATE CURVES. Uncertainty in experimental results is shown as the hatched region.

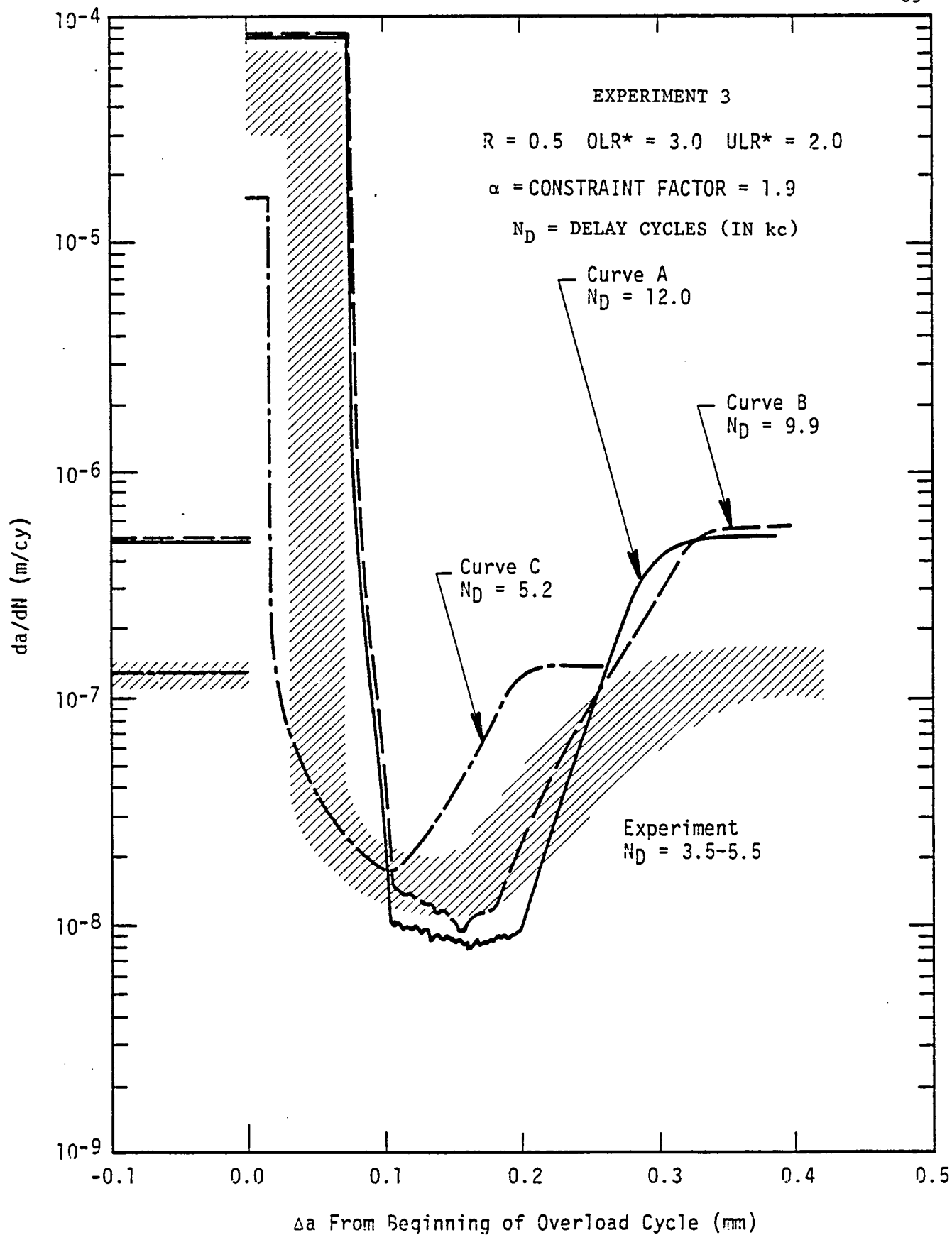


FIGURE 42. COMPARISON OF EXPERIMENTAL RESULTS AND MODEL PREDICTIONS FOR VARIOUS CRACK GROWTH RATE CURVES. Uncertainty in experimental results is shown as the hatched region.

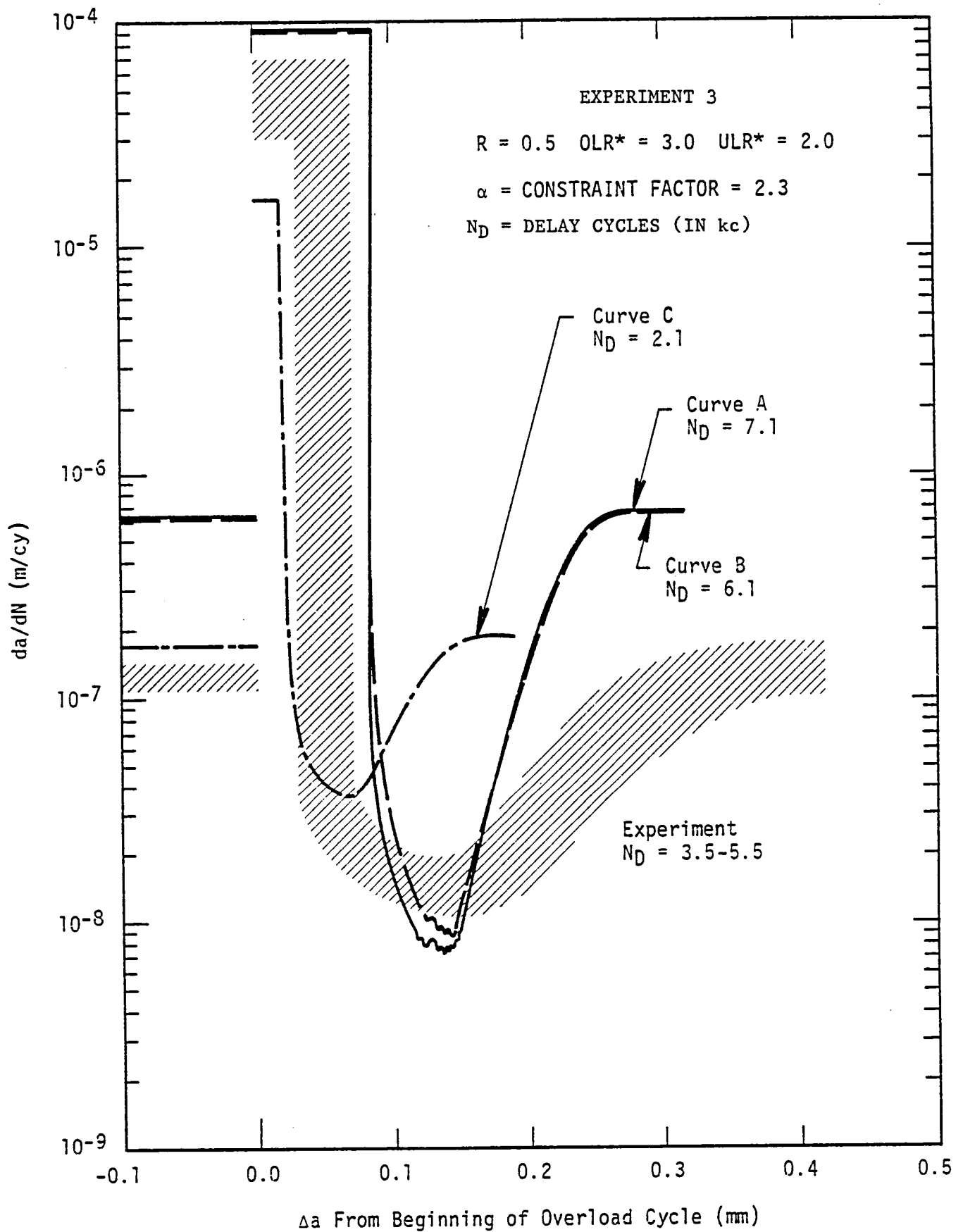


FIGURE 43. COMPARISON OF EXPERIMENTAL RESULTS AND MODEL PREDICTIONS FOR VARIOUS CRACK GROWTH RATE CURVES. Uncertainty in experimental results is shown as the hatched region.

It is suspected that these initial growth rates may have been influenced by transient effects associated with load shedding prior to the overload experiment, i.e., steady state growth rates may not have been fully achieved before the next experiment was conducted.

Figures 42 and 43 show a comparison of the growth rate effect for constraint factors of 1.9 and 2.3, respectively. Note that the sensitivity of predictions to growth rate effect is more significant for $\alpha = 2.3$ (Figure 43).

To assess the effect of crack growth rate properties and constraint factor, many analyses were performed for each of the three experiments using the three growth rate curves described above and constraint factors in the range from 1.5 to 3.0. More detailed results from these analyses are presented in tabular form in Appendix B.

The FAST-2 model predicts the general trends in crack growth rate response following the load excursions. However, a rigorous assessment of the model is limited by its sensitivity to variability in constant amplitude growth rate properties.

4.2 Influence of Constraint Factor on Analytical Predictions

Analyses were performed for the three crack growth rate curves in Figure 39 and for a variety of constraint factors. The constraint factor, which ranges from 1.0 for plane stress to 3.0 for plane strain, serves to elevate the tensile flow stress, thereby simulating the effect of through-thickness constraint on the crack-tip stresses. Options in the FAST-2 computer program allow the constraint factor to be fixed at a given level (used for most cases) or allowed to vary according to the instantaneous ratio of the plastic zone size to the specimen thickness (ρ/t); specifically, for the i_{th} cycle:

$$\alpha_i = 3.67 - 6.67 \frac{\rho_i}{t} \alpha_{i-1}^2 \quad (3)$$

where: $1.0 \leq \alpha_i \leq 3.0$

For Experiments 3 and 4, the above relation gave constraint factors for the overload cycles of 1.68 and 1.75, respectively. For all other baseline cycles, and for the overload cycle of Experiment 1 ($OLR^* = 2.15$), the above relation gave a constraint factor of 3.0. Fixed constraint factors used in the analyses ranged from 1.5 to 2.7.

Figures 44 and 45 show analytical predictions for Experiment 1 for various constraint factors and Growth Rate Curves B and C, respectively. Best results for Experiment 1 appear to be obtained with a constraint factor of between 1.7 and 1.9, although the lower constraint factor predicts a minimum growth rate lower than that observed in the experiment. This lower α compensates for the fact that the measured minimum growth rate persists over a longer increment of crack extension than the predicted rates and thereby gives the best prediction of N_D .

Figures 46 and 47 show results at various α 's for Experiment 4 with Growth Rate Curves B and C, respectively. Because of the large OLR^* for Experiment 4 and the attendant crack growth rate retardation, for $\alpha < 2.3$, the model generally predicted arrest (i.e., the model was run for 90,000 cycles and then aborted before the growth rate recovered). Predictions using Curve B and $\alpha = 2.1$ eventually recovered to give $N_D = 65$ kc.

The above results for Experiment 4 would seem to be in disagreement with the results for Experiment 1, where the optimum fixed α was between 1.7 and 1.9. The best agreement between measured and predicted results for Experiment 4 was obtained with Growth Rate Curve B for the variable- α --for which the constraint factor was 1.68 for the overload and 3.0 for the baseline cycling. Because the higher constraint factors gave more accurate predictions of the minimum growth rates for Experiment 1, it is thought that the use of the low constraint factor for Experiment 1 acts to artificially depress the minimum growth rate to compensate for an inaccurate overprediction of the acceleration, or rate of recovery.

The results for Experiment 4 for $\alpha \geq 2.5$ do not appear to differ significantly, especially in Figure 47, indicating the model is more sensitive to changes in $\alpha < 2.5$ than to changes in $\alpha > 2.5$. The variable α seems to best represent the rate of recovery throughout the analysis and hence the shape of the $da/dN-\Delta a$ curve for Experiment 4 (Figure 46).

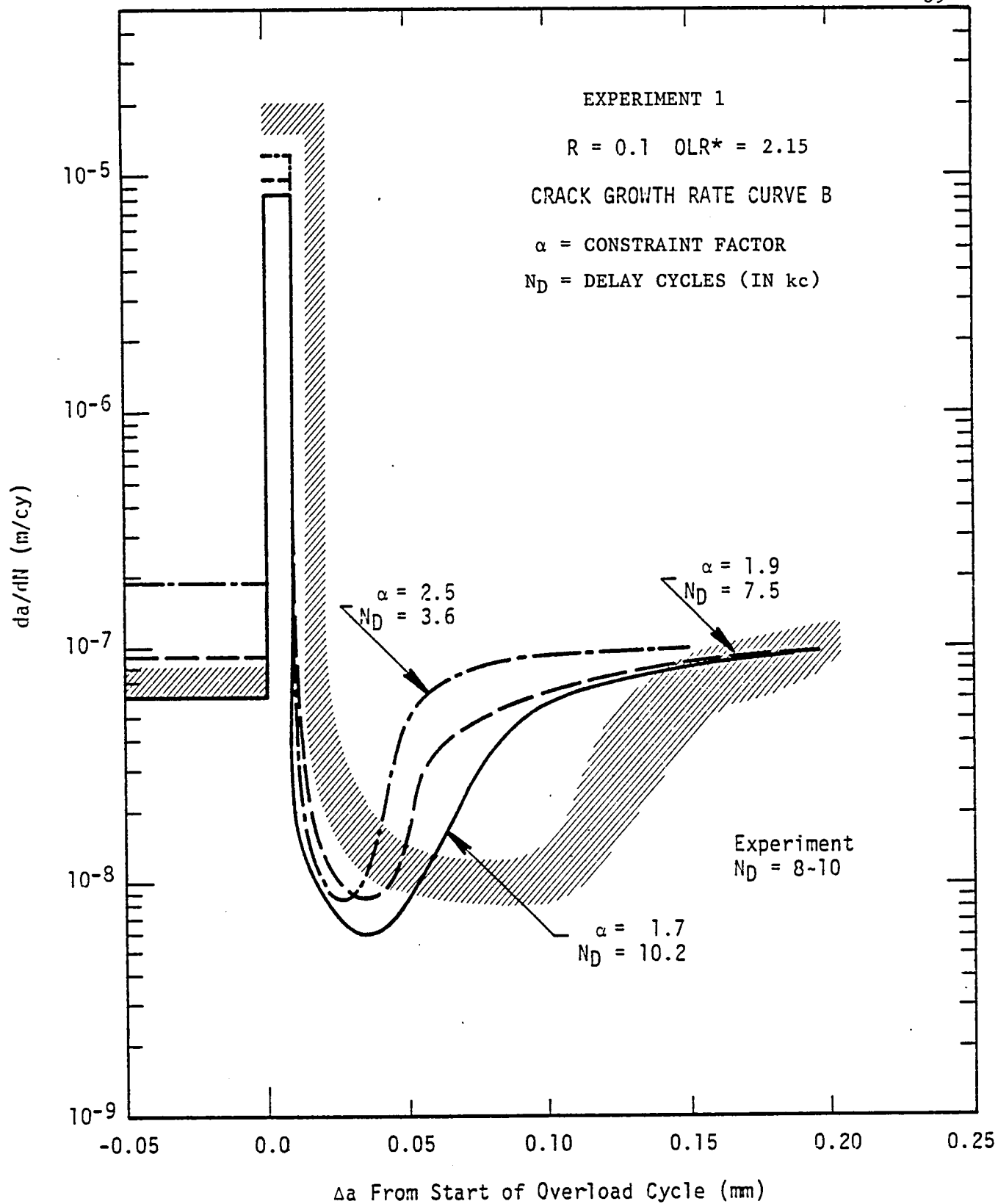


FIGURE 44. COMPARISON OF EXPERIMENTAL RESULTS AND MODEL PREDICTIONS FOR VARIOUS CONSTRAINT FACTORS (α). Uncertainty in experimental results is shown as the hatched region.

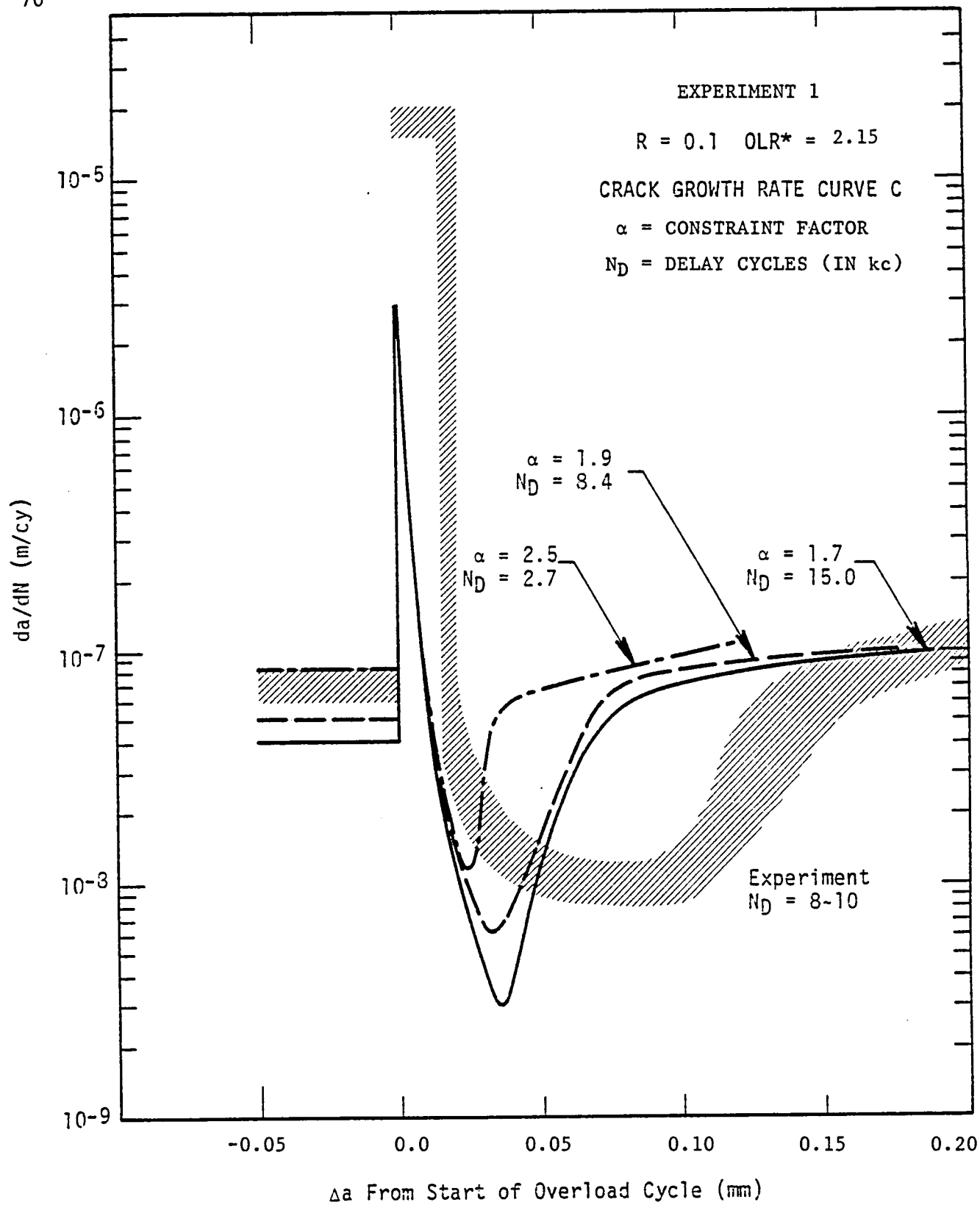


FIGURE 45. COMPARISON OF EXPERIMENTAL RESULTS AND MODEL PREDICTIONS FOR VARIOUS CONSTRAINT FACTORS (α). Uncertainty in the experimental results is shown as the hatched region.

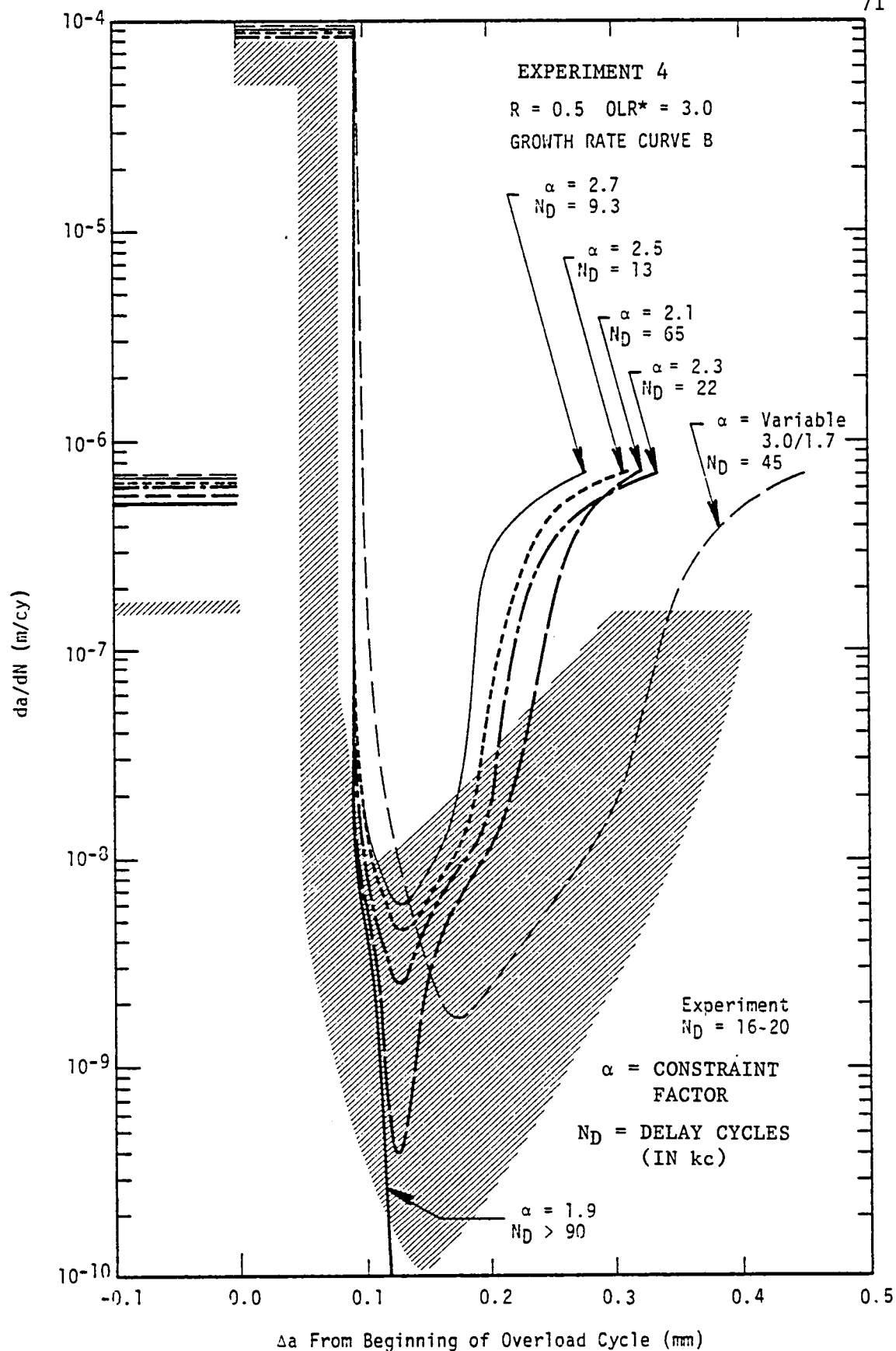


FIGURE 46. COMPARISON OF EXPERIMENTAL RESULTS AND MODEL PREDICTIONS FOR VARIOUS CONSTRAINT FACTORS (α). Uncertainty in experimental results is shown as the hatched region.

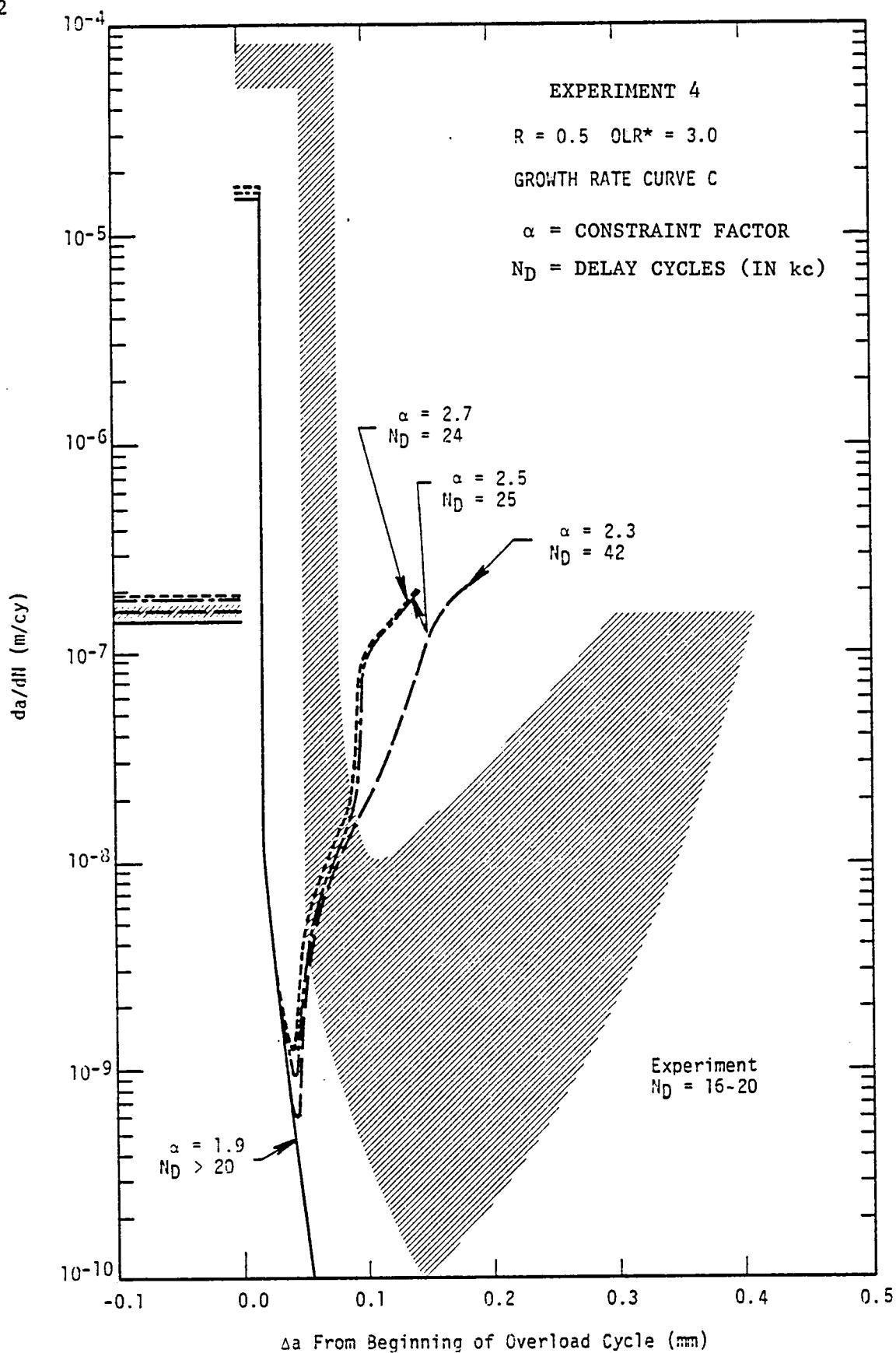


FIGURE 47. COMPARISON OF EXPERIMENTAL RESULTS AND MODEL PREDICTIONS FOR VARIOUS CONSTRAINT FACTORS (α). Uncertainty in experimental results is shown as the hatched region.

Figures 48 and 49 show the results of predictions for Experiment 3. Considering that all conditions for this experiment were the same as for Experiment 4, with the exception of the underload, it is seen that the underload has a significant effect on diminishing the retardation due to the overload, and that the plastic-wake closure model predicts this phenomenon.

Figure 49 shows the results of predictions based on Growth Rate Curve C for α from 1.5 to 2.5. Only the lowest α 's correctly predict the amount of crack extension at recovery, but N_D for the low α 's is higher than N_D observed in the experiment. The optimum α using Curve C seems to be about 1.9. The maximum growth rates are significantly underpredicted by Curve C.

Results based on Curve B are shown in Figure 48. The initial growth rates are poorly predicted by Curve B. The optimum α for these predictions is difficult to judge for $\alpha = 1.7 \sim 2.1$; the correct crack extension is predicted but the N_D is overpredicted. For variable α and fixed $\alpha = 2.5 \sim 2.7$, the N_D and da/dN average are well predicted. Note the marked difference in the shape of the recovery curve for the variable α .

4.3 Summary

The optimum constraint factor (α) for each experiment was different and dependent on the assumed constant amplitude growth rate properties. This is largely because this factor can serve as an adjustment of the analysis to compensate for other problems in the prediction, e.g., inaccurate crack growth rate properties. Overall, best results were obtained with variable α ; it seems that using fixed α results in poor prediction of the shape of the crack growth recovery curve.

Initial crack growth rates before the overload were not well predicted by the model using a growth rate curve that otherwise gave the best post-overload results (i.e., Curve B). Examination of the experimental data led to the hypothesis that in some cases the crack growth rate had not fully recovered from transients associated with load shedding prior to the overload experiments. Future analysis should include simulation of the events prior to the overload.

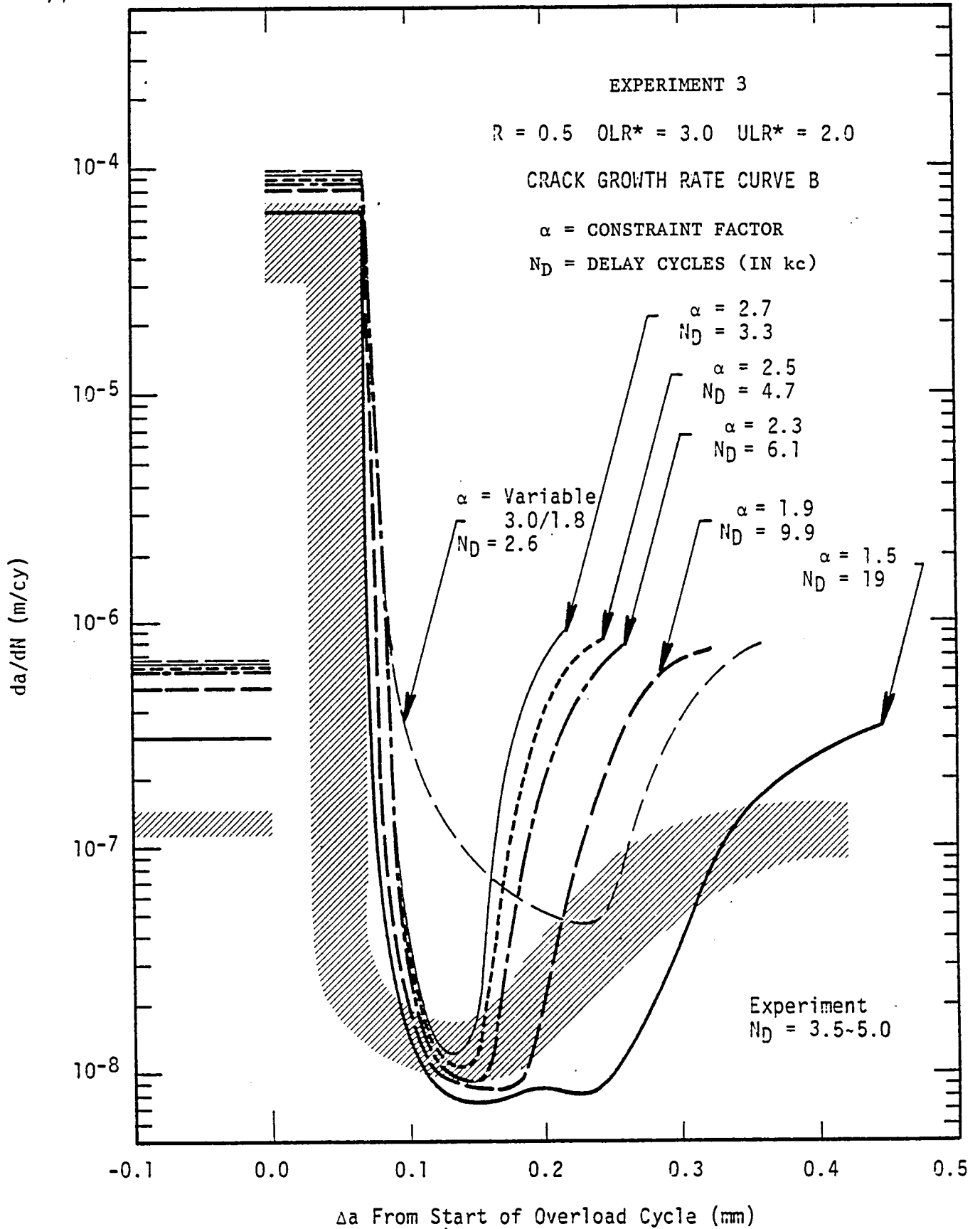


FIGURE 48. COMPARISON OF EXPERIMENTAL RESULTS AND MODEL PREDICTIONS FOR VARIOUS CONSTRAINT FACTORS (α). Uncertainty in experimental results is shown as the hatched region.

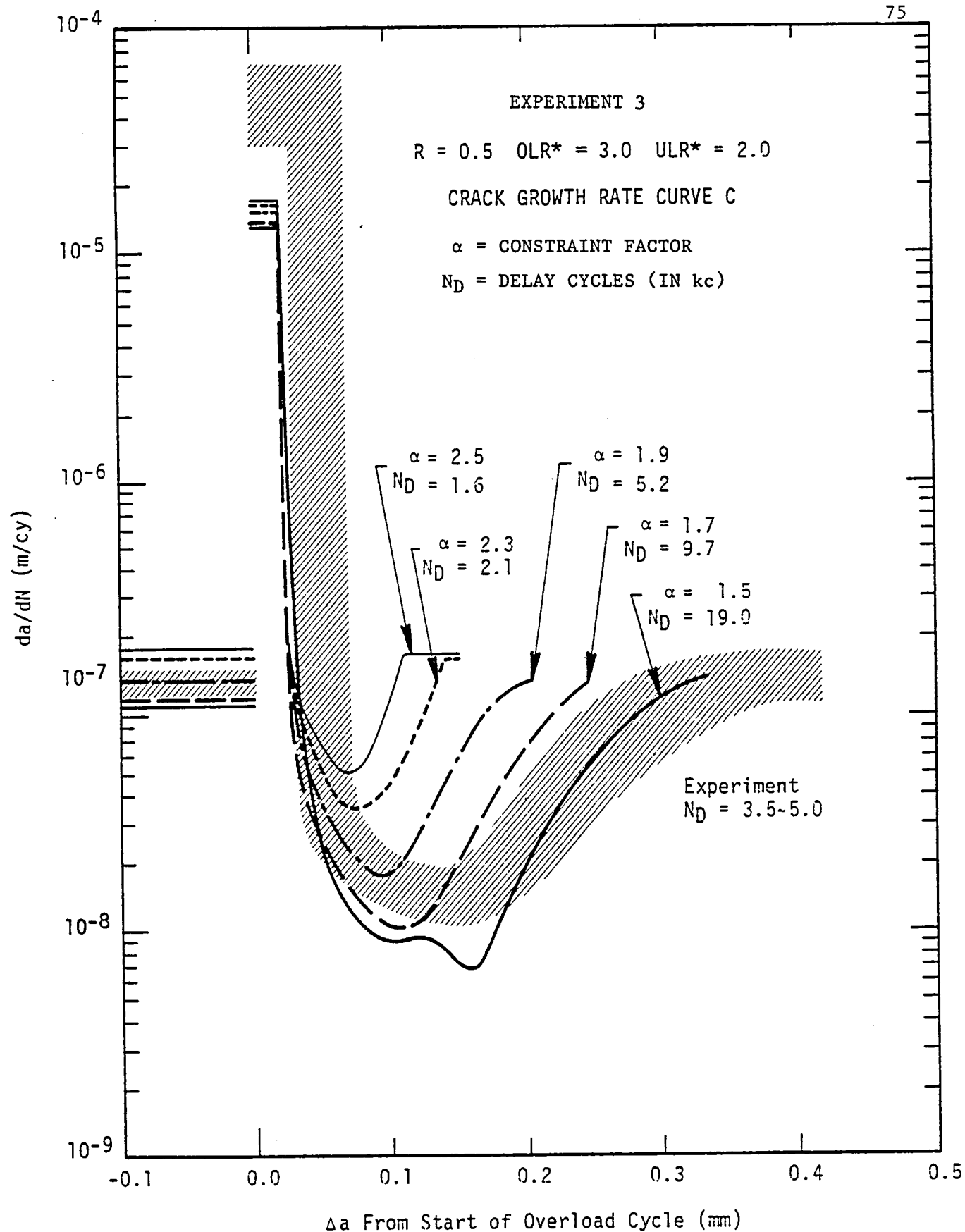


FIGURE 49. COMPARISON OF EXPERIMENTAL RESULTS AND MODEL PREDICTIONS FOR VARIOUS CONSTRAINT FACTORS (α). Uncertainty in experimental results is shown as the hatched region.

The maximum and minimum growth rates predicted in the analysis are affected mainly by the $da/dN-\Delta K_{eff}$ curve, while the amount of crack extension during retardation is affected mainly by the constraint factor, particularly the constraint factor for the overload cycle which directly affects the overload plastic zone size.

5.0 DISCUSSION

It is instructive to further compare the crack opening load values obtained locally using the stereoimaging technique with those obtained remotely using the elastic compliance technique, as shown in Figure 5. The observed differences are at least partially due to the fact that the stereoimaging measurements are sensitive to the near-tip response of the crack, while the compliance measurements depend only on the global response of the cracked specimen and are thus insensitive to local crack-tip response. In addition, the latter provides a measure of the average through-thickness response of the cracked specimen, while the stereoimaging measurements may be dominated by the response of the plane stress region at the specimen surface.

The above implies that the extent of crack closure varies significantly from the surface to the interior of the specimen in proportion to the transition in the near-crack-tip stress state from predominantly plane stress at the surface to increasingly plane strain toward the interior. This view is consistent with the fact that agreement between the constant amplitude stereoimaging measurements of ΔK_{eff} and those predicted using the FAST-2 model can only be obtained when plane stress conditions are assumed in the model, Figure 4. The latter is achieved by setting the constraint factor to $\alpha = 1$. Concurrently, the larger $\Delta K_{eff}/\Delta K$ values measured by the compliance technique can be matched by the analytical results by using larger α values.

A three-dimensional view of the crack closure process is consistent with recent subsurface measurements in a transparent polymer obtained using optical interferometry [8,9] and in a steel obtained using a compliance technique involving hole drilling along with a special displacement transducer [10-12]. These results are also consistent with the measured increase in ΔK_{eff} which has been observed when the plane stress surface regions have been removed by machining subsequent to constant amplitude fatigue crack growth [13]. Indirect evidence for this effect is provided

by the fact that delay periods following overloads tend to increase as the specimen thickness is decreased [14-21].

In spite of the above observations, a quantitative understanding of the role of through-thickness constraint on crack closure, crack growth, and load interaction effects has not yet emerged. Specifically, it is not possible to generalize the above results with respect to loading variables, particularly applied ΔK , R , and OLR^* . For example, most of the results cited above were obtained at relatively high ΔK values where differences in through-thickness constraint are accentuated, thus the applicability of these results to near-threshold fatigue crack growth is uncertain. A study utilizing both remote (average) and local (surface) measurements of crack closure in complementary fashion, while systematically varying thickness and applied loading variables, is needed to clarify this issue.

Although substantial variability was observed in the measured ΔK_{eff} values, as shown in Figure 3, there nevertheless appears to be a systematic deviation between the measured and predicted values of ΔK_{eff} at both low and high values of load ratio, Figure 4. The deviation at low- R values may be due to the operation of supplementary mechanisms of crack closure--for example, closure induced by accumulation of oxides [22-25] and asperity contact due to surface roughness [26-30]. Of the above candidates, oxide-induced crack closure is believed to be most likely in the current system. Oxides are known to readily occur within cracks in aluminum alloys which have been exposed to laboratory air, either during crack extension [25,31] or during subsequent storage [31]. On the other hand, the occurrence of crack roughness-induced closure is inconsistent with the relatively smooth fracture surface morphology which occurs in the 7091 alloy.

At high- R , the deviation between measured and predicted values would appear to be due to another factor. Specifically, it may be due to the fact that the crack-tip element size used in the FAST-2 model is too large to accurately represent the localized nature of the crack opening process, as shown in Figure 2. Thus, the analytical model, which gives the response averaged over the entire element, will predict less crack closure than measured very near the actual crack tip. While it is not

clear whether or not this factor actually predominates at high-R, this can be resolved by a systematic examination of the influence of element size on the predicted crack closure over the entire domain of relevant loading variables.

Examination of the crack-tip residual stresses caused by the overload and overload/underload cycles indicates that the magnitude of the compressive residual stresses ahead of the crack-tip is approximately limited to the yield stress and is independent of the severity of the overload. However, the spacial extent of the compressive residual stress field, including both the length and breadth, increases as the severity of the overload increases. Furthermore, for the case of the underload, following the overload, the extent of the compressive residual stress field is reduced, particularly in width.

Although additional results are needed to demonstrate that the above trend extends to a wider range of loading variables, the current results nevertheless demonstrate the importance of the residual stresses ahead of the crack tip to the growth of cracks subjected to variable-amplitude loading.

Considering the crack-tip strain field in greater detail indicates that the distribution of strain within the plastic zone is similar both before and after the overload, as shown in Figure 26. Thus, a major effect of the overload cycle is to alter the magnitude of the crack-tip strain field, Figure 24. Moreover, the crack growth rates were always found to correlate with the magnitude of the crack-tip strains -- before, during, and after the overload, Figure 38. These findings indicate that the mechanism of crack extension is the same for both the steady state and overload-affected regions of crack growth.

Thus, the problem of predicting crack growth rates under variable amplitude loading appears to be one of determining the correct "driving force" for crack growth rather than accounting for differences in the material response or intrinsic mechanism of crack extension. The similitude which appears to be maintained during variable-amplitude crack growth suggests the crack "driving force" can be properly characterized in terms

of crack closure concepts through ΔK_{eff} , provided that all of the physical processes contributing to this parameter are considered. Although the latter are generally and qualitatively known to include crack-tip residual stress, wake plasticity, oxide formation and accumulation, and asperity contact, the challenge which remains is to assess their relative importance for various growth rate regimes and formulate quantitative models capable of predicting ΔK_{eff} and crack growth rate responses.

6.0 CONCLUSIONS AND RECOMMENDATIONS

1. Under constant amplitude loading, the magnitude of the crack-tip opening load and ΔK_{eff} --as determined local to the crack tip by stereoimaging--depend on the applied values of both ΔK and K_{max} (or ΔK and R , or K_{max} and R) as described by the following simple relationship for 7091 aluminum:

$$\frac{\Delta K_{eff}}{\Delta K} = 1 - \frac{5}{K_{max}}$$

2. The relation between the extent of the crack which remains open and the applied load is highly nonlinear. For example, the load required to "peel" open the last 20 μm of the crack, near its tip, is two to three times higher than that required to open the crack to within 200 μm of the tip. Thus, the measurement of P_0 or ΔK_{eff} is highly dependent on the sensitivity of the measurement technique.
3. Local surface measurements of crack-tip opening load using the stereoimaging technique give higher values of P_0 , and correspondingly lower values of ΔK_{eff} , than do remote measurement techniques such as elastic compliance.
4. The magnitude of the overload/underload cycle controls the spacial extent of the compressive residual stress field both parallel and perpendicular to the direction of crack growth, whereas the magnitude of this compressive stress field is limited to the flow stress of the material. These results are consistent with the degree of crack growth retardation following the overload/underload cycle and thereby attest to the importance of crack-tip residual stress during variable-amplitude fatigue crack growth.

5. A correlation exists between the fatigue crack growth rate and the crack-tip strain measured before, during, and after the overload, thus indicating that the intrinsic mechanism of crack growth is strain controlled and is the same for constant-amplitude and variable-amplitude fatigue crack growth.
6. Similitude in crack-tip plasticity is maintained during variable-amplitude fatigue crack growth. This similitude is manifested by a uniqueness in (a) strain distribution within the crack-tip plastic zone, and (b) the relationship between crack-tip strain and crack-tip opening displacement.
7. It follows from Conclusions 5 and 6 that the problem of predicting variable-amplitude fatigue crack growth is one of determining the proper "driving force" for crack growth. Incorporating crack closure concepts into an effective stress intensity factor appears to be a viable approach to characterizing the crack "driving force," provided the contributions of all relevant physical processes are included.
8. The FAST-2 analytical model provides reasonable predictions of the crack growth rate trends following single overloads and overload/underload cycles. However, the sensitivity of predictions to the constant-amplitude fatigue crack growth rate properties, combined with the lot-to-lot variability in these properties, currently limits a rigorous assessment of this model. This limitation can be overcome by generating constant-amplitude crack growth rate data from the same 7091 extrusion used for the overload experiments.
9. The maximum and minimum growth rates predicted by the model during the overload-affected crack growth period are sensitive to the input growth rate properties, while the extent of the overload-affected region is sensitive to the constraint factor applied to tensile yielding since the latter affects the overload plastic zone size. The shape of the growth

rate versus crack extension curve following the overload is most accurately predicted by using the variable constraint feature of the model.

10. It is recommended that further assessments of the FAST-2 analytical model consider the following factors:

- (a) Sensitivity of results to crack-tip element size
- (b) Differences between displacement-based and K-based crack opening criterion
- (c) Limitations of applying the Dugdale solutions for the center-cracked-tension geometry to other geometries*; specifically, by defining the amount of crack extension which can be tolerated without introducing significant errors due to differences in K-gradient, dK/da .

* The current version of FAST-2 uses the Dugdale solution for a center-cracked-tension geometry. In order to properly apply this model to the analysis of the single-edge-notched specimens used in this study, the K values in the model and the experiment were initially matched and the extent of crack extension was limited to that corresponding to a single overload event. This restriction precluded analyzing a series of overload events to examine the possibility of interactions between events. Such analyses would provide useful guidance for the planning of experiments since multiple tests, performed on a single specimen, are often utilized to maximize the efficiency of data generation.

7.0 REFERENCES

1. S. J. Hudak, Jr., D. L. Davidson, and K. S. Chan, "Measurement and Analysis of Critical Crack Tip Processes Associated with Variable Amplitude Fatigue Crack Growth," NASA Contractor Report 172228, September 1983.
2. A. J. McEvily, "The Fatigue of Powder Metallurgy Alloys," Annual Report, AFOSR-TR-0111, U. S. Air Force, January 1984 (available from DTIC as AD 4138 714).
3. D. L. Davidson, "The Observation and Measurement of Displacements and Strain by Stereoimaging," Scanning Electron Microscopy/1979/II, pp. 79-86 (1979).
4. D. R. Williams, D. L. Davidson, and J. Lankford, "Fatigue-Crack-Tip Plastic Strains by the Stereoimaging Technique," Experimental Mechanics, Vol. 20, pp. 134-139 (1980).
5. D. L. Davidson and J. Lankford, "Fatigue Crack Tip Mechanics of a Powder Metallurgy Aluminum Alloy in Vacuum and Humid Air," Fatigue of Engineering Materials and Structures, Vol. 7, No. 1, pp. 29-39 (1984).
6. D. L. Davidson, D. R. Williams, and J. E. Buckingham, "Crack-Tip Stresses as Computed from Strains Determined by Stereoimaging," Experimental Mechanics, Vol. 23, No. 2, pp. 242-248 (1983).
7. J. C. Newman, Jr., "A Crack-Closure Model for Predicting Fatigue Crack Growth Under Aircraft Spectrum Loading," in Methods and Models for Predicting Fatigue Crack Growth Under Random Loading, ASTM STP 748, p. 53 (1981).
8. S. Ray and A. F. Grandt, Jr., "Three-Dimensional Measurements of Fatigue Crack Closure," NASA Contractor Report CR-173679, July 1984.
9. S. Ray, A. F. Grandt, Jr., and S. Andrew, "Three-Dimensional Measurements of Fatigue Crack Opening and Closure," ASTM Symposium on Fundamental Questions and Critical Experiments on Fatigue, Dallas, TX, October 1984.
10. N. A. Fleck and R. A. Smith, "Crack Closure-Is It Just a Surface Phenomenon?," Intl. J. of Fatigue, Vol. 4, No. 3, pp. 157-160 (July 1982); Also see correction in Intl. J. of Fatigue, p. 243 (October 1982).
11. N. A. Fleck, I.F.C. Smith, and R. A. Smith, "Closure Behavior of Surface Cracks," Fatigue of Engr. Matls. and Structs., Vol. 6, No. 3, pp. 225-239 (1983).

12. N. A. Fleck, "Influence of Stress State on Crack Growth Retardation," ASTM Workshop on Fundamental Questions and Critical Experiments on Fatigue, Arlington, TX, October 1984.
13. G. Marci, "Effect of Active Plastic Zone on Fatigue Crack Growth Rates," Fracture Mechanics, ASTM STP 677, pp. 168-186 (1979).
14. E.F.J. von Euw, R. W. Hertzberg, and R. Roberts, "Stress Analysis and Growth of Cracks, ASTM STP 513, p. 230 (1972).
15. R. P. Wei and T. T. Shih, "Delay in Fatigue Crack Growth," Int. J. Fract., Vol. 10, No. 1, pp. 77-85 (1974).
16. T. T. Shih and R. P. Wei, "A Study of Crack Closure in Fatigue," Engng. Fract. Mech., Vol. 6, pp. 19-32 (1974).
17. T. T. Shih and R. P. Wei, "Effect of Specimen Thickness on Delay in Fatigue Crack Growth," J. Testing and Evaluation, ASTM, Vol. 3, p. 46, (1975).
18. W. J. Mills and R. W. Hertzberg, "The Effect of Sheet Thickness on Fatigue Crack Retardation in 2024-T3 Aluminum Alloy," Engr. Fracture Mechanics, Vol. 17, p. 705 (1975).
19. T. T. Shih and R. P. Wei, "Influences of Chemical and Thermal Environments on Delay in a Ti-6Al-4V Alloy", Fatigue Crack Growth Under Spectrum Loads, ASTM STP 595, pp. 113-124 (1976).
20. G. R. Chanani, "Effect of Thickness on Retardation Behavior of 7075 and 2024 Aluminum Alloys," in Flaw Growth and Fracture, ASTM STP 631, p. 365 (1977).
21. S. Matsuoka and K. Tanaka, "The Influence of Sheet Thickness on Delayed Retardation Phenomena in Fatigue Crack Growth in HT80 Steel and A5083 Aluminum Alloy," Engr. Fracture Mechanics, Vol. 13, p. 293 (1980).
22. A. T. Stewart, "The Influence of Environment and Stress Ratio on Fatigue Crack Growth at Near Threshold Stress Intensities in Low Alloy Steels," Engineering Fracture Mechanics, Vol. 13, pp. 463-478 (1980).
23. R. O. Ritchie, S. Suresh, and C. M. Moss, "Near-Threshold Fatigue Crack Growth in 2-1/2 Cr-Mo Pressure Vessel Steel in Air and Hydrogen," Journal of Engineering and Materials Technology, Transactions ASME, Series H, Vol. 102, pp. 293-299 (1980).
24. S. Suresh, G. F. Zamiski, and R. O. Ritchie, "Oxidation and Crack Closure. An Explanation for Near-Threshold Corrosion Fatigue Crack Growth Behavior," Metallurgical Transaction, Vol. 12A, pp. 1435-1443 (1981).

25. A. K. Vansudevan and S. Suresh, "Influence of Corrosion Deposits on Near-Threshold Fatigue Crack Growth Behavior in 2XXX and 7XXX Series Aluminum Alloys," Metallurgical Transactions, Vol. 13A, pp. 2271-2280 (1982).
26. K. Minakawa and A. J. McEvily, "On Crack Closure in Near-Threshold Region," Scripta Metallurgica, Vol. 15, pp. 633-636 (1981).
27. K. Minakawa and A. J. McEvily, "On Near-Threshold Fatigue Crack Growth in Steels and Aluminum Alloys," Fatigue Threshold, Vol. 1, J. Backlund, A. F. Blom, and C. J. Beevers, EMAS Publication, Westerley, U.K., pp. 373-390 (1981).
28. R. O. Ritchie and S. Suresh, "Some Consideration on Fatigue Crack Closure Induced by Fracture Surface Morphology," Metallurgical Transactions, Vol. 13A, pp. 1627-1631 (1982).
29. S. Suresh and R. O. Ritchie, "A Geometric Model for Fatigue Crack Closure Induced by Fracture Surface Morphology," Metallurgical Transactions, Vol. 13A, pp. 1627-1631 (1982).
30. S. Suresh, "Micromechanisms of Fatigue Crack Growth Retardation Following Overloads," Engineering Fracture Mechanics, Vol. 18, No. 3, pp. 577-593 (1983).
31. J. Lankford and D. L. Davidson, "Wear Debris Due to Mode II Opening of Mode I Fatigue Cracks in an Aluminum Alloy," Met. Trans., Vol. 14A, pp. 1227-1230 (1983).

APPENDIX A

DEFINITION OF LOADING VARIABLES AND DELAY CYCLES FOR VARIABLE AMPLITUDE FATIGUE CRACK GROWTH

The quantities related to constant load-amplitude cycling of fatigue cracks are given in Fig. A1. Effective ΔK is computed from values of the load P_0 required to open the crack down to the tip and the R ratio, according to the equation in the figure.

Several different definitions have evolved to characterize the magnitude of the load excursions. Experiments are commonly conducted so that the mean stress of the baseline cycling is maintained constant during a given overload test by fixing the load ratio ($R = K_{\min}/K_{\max} = P_{\min}/P_{\max}$). The definition of the overload, or underloading ratio can be formulated in terms of either the ratio of the maximum values or the ranges of the stress intensity factor for the overload to base loading cycles, as shown in Fig. A2, giving

$$OLR = K_{OL}/K_{\max} = P_{OL}/P_{\max} \quad (A1)$$

$$OLR^* = \Delta K_{OL}/\Delta K = (P_{OL} - P_{\min})/(P_{\max} - P_{\min})$$

$$ULR^* = \frac{\Delta K_{UL}}{\Delta K} = \frac{P_{\max} - P_{UL}}{P_{\max} - P_{\min}} \quad (A2)$$

where P_{\min} and P_{\max} are the minimum and maximum load values in the base cycle, and P_{OL} is the maximum load in the overload cycle, and P_{UL} is the minimum load in the underload cycle. As indicated in Equations A1 and A2, OLR is referenced to zero load, while OLR^* and ULR^* are referenced to the minimum cyclic load. Thus, both definitions are identical when $P_{\min} = 0$ ($R = 0$). However, in general the relationship between OLR and OLR^* depends on R as follows:

$$OLR^* = \frac{OLR - R}{1 - R} \quad (A3)$$

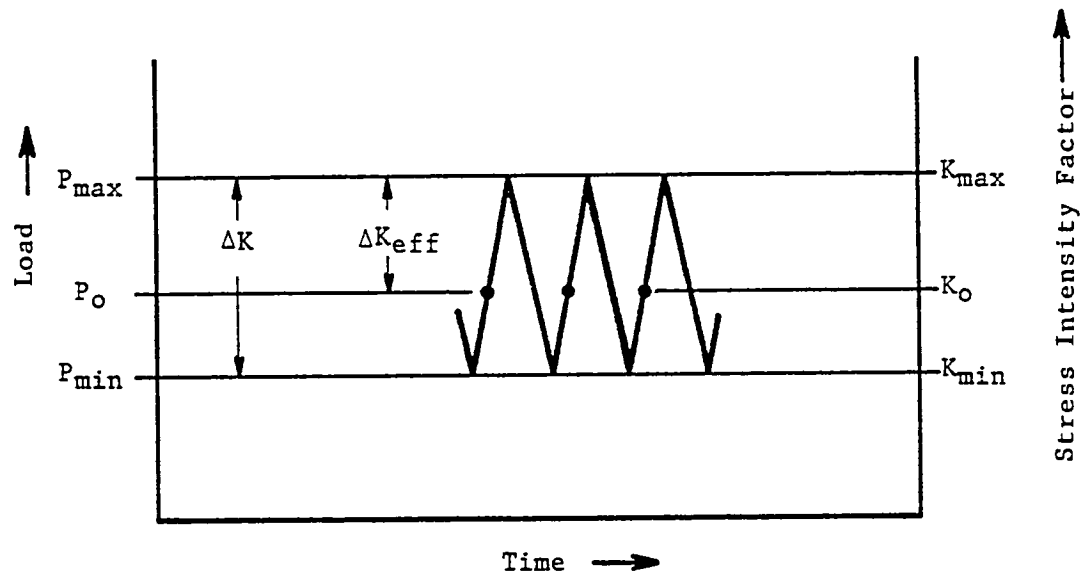
The current study uses OLR^* and ULR^* , since these definitions are more meaningful when comparing results at different R values.

The various definitions which have been used for the number of delay cycles are illustrated in Figure A3. A typical response of crack length versus number of cycles and corresponding crack growth rate versus number of cycles are shown in Figures 3(a) and 3(b), respectively. The response of the crack during a single overload experiment is as follows. Initially, steady state crack growth occurs in region a-b at stress intensity factor ΔK_1 immediately preceding the overload. The overload cycle corresponding to ΔK_{OL} may then cause a brief accelerated growth period in region b-c, followed by a precipitous decrease in growth rate to a minimum growth rate and eventual recovery in region c-e. Steady state growth is re-established in region e-f at ΔK_2 . Generally, ΔK_2 is nearly equal to ΔK_1 since growth has only occurred over a crack length interval which is on the order of the plastic zone size of the overload.

The "delay" caused by the load excursion can be operationally defined in terms of a period over which the effective crack growth is zero by constructing c-d and e-d to give N'_D as shown in Figure A3(a). Alternatively, delay may be simply defined as the number of cycles over which the crack growth rate is less than the preoverload value--this measure corresponds to b-e in Figures A3(a) and A3(b) and is labeled N_D .

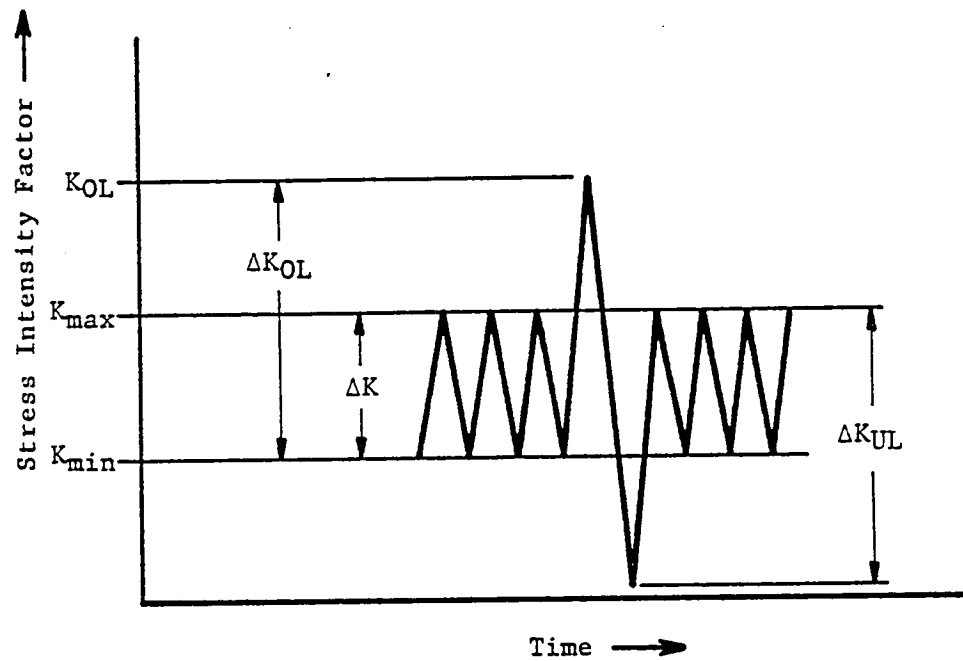
The above two definitions can differ significantly, particularly for low overload ratios where the delay period is relatively small. N_D will always be greater than N'_D since the latter is based on the extrapolation e-d and does not include the accelerated growth period b-c.

The current study uses N_D as the measure of delay primarily because it is a relatively straightforward operational definition which can be easily applied to both experimental data and model predictions by monitoring the post-overload crack growth rate.



$$\frac{\Delta K_{\text{eff}}}{\Delta K} = \frac{K_{\max} - K_o}{K_{\max} - K_{\min}} = \frac{1 - P_o/P_{\max}}{1 - R}$$

FIGURE A1. DEFINITION OF LOAD AND STRESS INTENSITY FACTOR VALUES RELATED TO THE MEASUREMENT OF CRACK OPENING LOAD.

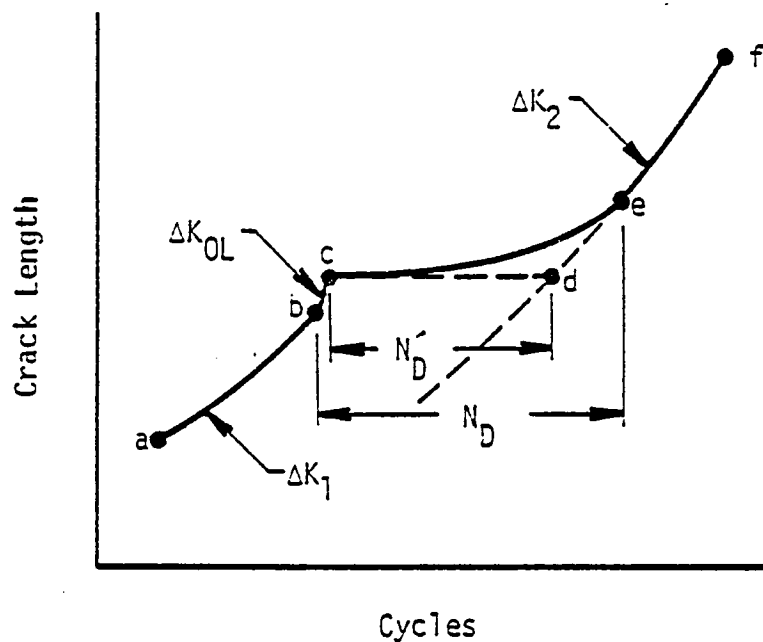


$$R = \frac{K_{\min}}{K_{\max}} = \frac{P_{\min}}{P_{\max}}$$

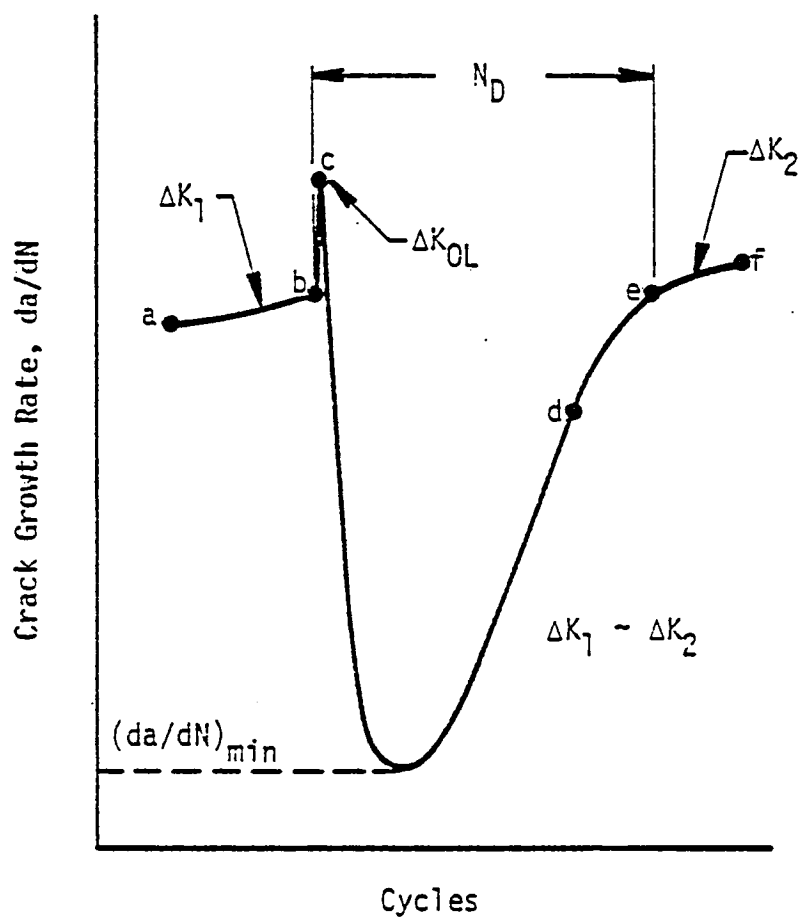
$$OLR^* = \frac{\Delta K_{OL}}{\Delta K} = \frac{P_{OL} - P_{\min}}{P_{\max} - P_{\min}}$$

$$ULR^* = \frac{\Delta K_{UL}}{\Delta K} = \frac{P_{\max} - P_{UL}}{P_{\max} - P_{\min}}$$

FIGURE A2. CHARACTERIZATION OF LOAD HISTORY AND DEFINITIONS OF OVERLOAD AND UNDERLOAD MAGNITUDES.



(a) Delay Cycles Defined Using Crack Length Versus Elapsed Cycles Data



(b) Delay Cycles Defined Using Crack Growth Rate Data

FIGURE A3. DEFINITIONS OF NUMBER OF DELAY CYCLES FOLLOWING A SINGLE OVERLOAD.

APPENDIX B

ADDITIONAL ANALYTICAL RESULTS OBTAINED USING THE FAST-2 MODEL

This appendix contains results which supplement those given in Section 4.0. First, a detailed summary of the comparisons of analytical predictions and experimental results is provided in tabular form. Then, the residual stresses at the maximum and minimum loads in the cycle are presented at various times before, during and after the overload/underload events.

B1. Detailed Comparison of Analytical and Experimental Results

The results for each case studied are presented in Tables B1 through B3. Information contained in these tables includes the predicted growth rate and effective load ratio (P_o/P_{max}) prior to the overload (initial) and during the overload (maximum). Also shown for the latter case is the increment of crack extension attributable to the overload cycle. The data labeled minimum correspond to the point of minimum crack growth rate following the overload. The minimum growth rate, R_{eff} at minimum, total crack extension from the beginning of the overload cycle, and the number of cycles applied between the overload and minimum are also shown. Finally, at recovery (i.e., the point when the crack growth rate recovers to the initial value), the total crack extension and number of cycles (N_D) are shown. In order to isolate the error in the predicted crack extension due to uncertainty in high growth rates associated with the overload cycle, the quantity $\Delta a - \Delta a_{OL}$ (i.e., the Δa recovery - Δa maximum) is shown.

The right-most column in each table reports the experimental data. These data are sometimes reported as a range to reflect the uncertainty in the experimental measurements.

Comparing experimental results and analytical predictions reveals that the constraint factor and growth rate curve which yields the best estimate of N_D does not always yield the best estimate of crack extension. Therefore, another criterion for comparison is offered in the last row, i.e., the average

TABLE B1

EXPERIMENT 1: OLR* = 2.15, R = 0.1

		GROWTH RATE CURVE C					GROWTH RATE CURVE A					GROWTH RATE CURVE B					Var. 4	EXPERIMENT	
CONSTRAINT FACTOR		1.5	1.7	1.9	2.3	2.5	1.7	1.9	2.1	2.3	2.5	1.5	1.7	1.9	2.1	2.3	2.5		
INITIAL	da/dN ($\times 10^{-8}$ m/cy)	3.16	4.03	5.04	6.94	7.06	5.99	8.83	12.0	15.7	19.5	3.95	5.99	8.83	12.0	15.7	19.6	30.8	6 - 8
	R _{eff}	0.46	0.43	0.40	0.35	0.33	0.43	0.40	0.30	0.35	0.34	0.47	0.43	0.40	0.30	0.35	0.34	0.30	0.55
HAxiUM	da/dN ($\times 10^{-6}$ m/cy)	-1	-	-	-	2.87	-	9.36	10.3	11.1	12.0	-	-	9.36	10.3	11.2	12.1	14.2	15 - 20
	R _{eff}	-	-	-	-	0.17	-	0.20	0.19	0.18	0.17	-	-	0.20	0.19	0.18	0.17	0.15	N/A
	A _a (mm)	-	-	-	-	0.0032	-	0.010	0.011	0.011	0.012	-	-	0.010	0.011	0.011	0.012	0.014	0.015 - 0.020
INITIAL UN	da/dN ($\times 10^{-9}$ m/cy)	(1.54) ²	(2.90)	(5.11)	(10.1)	12.8	(3.99)	(5.11)	4.84	5.58	6.03	3.63	(6.39)	(7.50)	7.33	7.90	8.39	9.27	10.0
	R _{eff}	(0.78)	(0.74)	(0.68)	(0.60)	0.58	(0.75)	(0.72)	0.73	0.71	0.69	0.83	(0.75)	(0.72)	0.73	0.71	0.69	0.67	0.78
	A _a (mm)	(0.042)	(0.035)	(0.025)	(0.019)	0.020	(0.036)	(0.040)	0.032	0.030	0.028	0.039	(0.036)	(0.040)	0.032	0.028	0.028	0.026	0.08
	N (kc)	(0.7)	(5.2)	(1.7)	(0.81)	0.63	(4.9)	(3.6)	2.9	2.2	1.8	6.2	(3.6)	(2.7)	2.1	1.5	1.5	1.0	4.5
RECOVERY	A _a (mm)	(>0.07) ³	(0.187)	(0.175)	(0.128)	0.117	(0.188)	(0.201)	0.197	0.146	0.146	0.227	(0.186)	(0.200)	0.189	0.145	0.150	0.143	0.20
	N _D (kc)	(>20.0)	(15.0)	(8.4)	(3.6)	2.7	(13.0)	(9.1)	8.1	5.4	4.3	19.0	(10.0)	(7.4)	6.5	4.4	3.6	2.5	0.5
	A _a -A _{a11} (mm)	-	(0.184)	(0.172)	(0.126)	0.114	(0.178)	(0.191)	0.186	0.135	0.134	0.218	(0.181)	(0.180)	0.178	0.134	0.138	0.129	0.18 - 0.19
	avg. da/dN following OL ($\times 10^{-8}$ m/cy)	-	(1.2)	(2.0)	(3.5)	4.2	(1.3)	(2.1)	2.3	2.5	3.1	1.1	(1.8)	(2.5)	2.7	3.0	3.8	5.1	1.8 - 2.3

1. In those cases where the dashes are shown, information on the maximum growth rate was not obtained.
2. In those cases where results are in parentheses, the number of elements used in the analysis changed during the computations and influences the results significantly, confounding comparisons with other cases where the number of elements was constant.
3. If results are presented as an inequality, the computation was stopped at a preset number of cycles (usually 90,000); i.e., the model effectively predicts crack arrest.
4. The constraint factor was 3.0 (plane strain) throughout the analysis.

TABLE B2

EXPERIMENT 3: OLR* = 3.0, ULR* = 2.0, R = 0.5

CONSTRAINT FACTOR→		GROWTH RATE CURVE C						GROWTH RATE CURVE A						GROWTH RATE CURVE B								EXPERIMENT
		1.5	1.7	1.9	2.3	2.5	2.7	1.7	1.9	2.1	2.3	2.5	2.7	1.5	1.7	1.9	2.1	2.3	2.5	2.7	Var. ²	
INITIAL	da/dN (x 10 ⁻⁷ m/cy)	1.01	1.22	1.39	1.67	1.75	1.89	4.13	5.01	5.46	6.54	6.93	6.94	3.04	4.13	5.01	5.47	6.54	6.93	6.94	6.94	1.1-1.5
	R _{eff}	0.60	0.58	0.57	0.55	0.54	0.54	0.59	0.57	0.56	0.55	0.55	0.55	0.60	0.59	0.57	0.56	0.55	0.55	0.55	0.55	0.59
MAXIMUM	da/dN (x 10 ⁻⁵ m/cy)	-1	1.47	1.54	1.65	1.67	1.72	7.36	8.07	8.41	9.18	9.47	9.48	6.64	7.36	8.07	8.41	9.18	9.47	9.48	9.48	3.0-7.0
	R _{eff}	-	0.29	0.28	0.27	0.27	0.27	0.29	0.29	0.28	0.28	0.27	0.27	0.30	0.29	0.29	0.28	0.28	0.27	0.27	0.27	0.30-0.32
	Δa (mm)	-	0.015	0.015	0.017	0.017	0.017	0.074	0.081	0.084	0.092	0.095	0.095	0.067	0.074	0.081	0.084	0.092	0.095	0.095	0.095	0.03-0.07
MINIMUM	da/dN (x 10 ⁻¹⁰ m/cy)	7.18	10.9	17.7	35.7	45.5	56.6	7.56	7.84	7.94	7.87	7.97	10.2	9.21	9.65	9.50	9.67	9.92	9.99	12.1	44.1	15.0-20.0
	R _{eff}	0.80	0.78	0.75	0.70	0.68	0.66	0.81	0.81	0.80	0.81	0.81	0.79	0.81	0.81	0.81	0.81	0.81	0.81	0.79	0.72	0.76
	Δa (mm)	0.159	0.105	0.093	0.065	0.064	0.060	0.173	0.159	0.151	0.135	0.131	0.126	0.145	0.173	0.158	0.140	0.139	0.132	0.125	0.231	0.175
	N (kc)	12.0	4.7	2.7	0.89	0.74	0.57	9.3	6.8	5.8	3.2	2.5	1.6	5.6	7.6	5.5	3.7	3.1	2.2	1.4	1.9	2.6
RECOVERY	Δa (mm)	0.332	0.242	0.200	0.147	0.145	0.150	0.370	0.328	0.282	0.260	0.240	0.220	0.443	0.370	0.325	0.282	0.260	0.239	0.219	0.363	0.29-0.40
	N _D (kc)	19.0	9.7	5.2	2.1	1.6	1.3	16.0	12.0	8.8	7.1	5.4	3.7	19.0	13.0	9.9	7.6	6.1	4.7	3.3	2.6	3.5-5.0
	Δa-Δa _{OL} (mm)	0.317	0.227	0.185	0.130	0.128	0.133	0.296	0.247	0.198	0.168	0.145	0.125	0.376	0.296	0.244	0.198	0.168	0.144	0.124	0.268	0.22-0.37
	avg. da/dN following OL (x 10 ⁻⁸ m/cy)	1.7	2.3	3.6	6.2	8.0	10.2	1.9	2.1	2.2	2.4	2.7	3.4	2.0	2.3	2.4	2.6	2.8	3.1	3.8	10.3	4.4-10.6

1. In those cases where the dashes are shown, information on the maximum growth rate was not obtained.
2. The constraint factor for this case was 3.0 (plain strain) for all cycles except the overload cycle where the constraint factor was computed to be 1.75.

TABLE B3

EXPERIMENT 4: OLR* = 3.0, R = 0.5

CONSTRAINT FACTOR	GROWTH RATE CURVE C				GROWTH RATE CURVE A					GROWTH RATE CURVE B					Var. 2	EXPERIMENT
	1.9	2.3	2.5	2.7	1.9	2.1	2.3	2.5	2.7	1.9	2.1	2.3	2.5	2.7		
I N I T I A L	da/dN ($\times 10^{-7}$ m/cy)	1.40	1.67	1.75	1.89	5.04	5.50	6.53	6.98	7.00	5.05	5.51	6.53	6.97	6.98	1.5 - 1.7
	R _{eff}	0.57	0.55	0.54	0.54	0.57	0.56	0.55	0.55	0.55	0.57	0.56	0.55	0.55	0.55	0.70
H A X I M U M	da/dN ($\times 10^{-5}$ m/cy)	1.55	1.65	1.69	1.74	8.16	8.50	9.21	9.57	9.58	8.16	8.50	9.21	9.57	9.58	5.0 - 8.0
	R _{eff}	0.28	0.27	0.27	0.27	0.29	0.28	0.28	0.27	0.27	0.29	0.28	0.28	0.27	0.27	0.25
	Δa (mm)	0.016	0.017	0.017	0.017	0.082	0.085	0.092	0.096	0.096	0.082	0.089	0.092	0.096	0.096	0.05 - 0.08
H I J N I M U M	da/dN ($\times 10^{-10}$ m/cy)	<3.871	5.07	8.75	12.9	<0.52	<1.35	7.68	24.9	37.7	<0.71	4.42	25.7	44.9	61.4	1.0 - 100.0
	R _{eff}	>.92	0.91	0.90	0.89	>0.96	>0.95	0.92	0.90	0.88	>0.97	0.96	0.93	0.90	0.88	0.96
	Δa (mm)	>0.042	0.045	0.043	0.041	>0.115	>0.125	0.126	0.126	0.123	>0.121	0.123	0.125	0.127	0.123	0.10 - 0.14
	N (kc)	>20.0	21.0	14.0	9.4	>90.0	>90.0	17.0	6.9	4.5	>90.0	24.0	6.9	4.5	3.1	3.0 - 7.0
R E C O V E R Y	Δa (mm)	>0.042	0.180	0.143	0.147	>0.115	>0.125	0.336	0.310	0.277	>0.121	0.319	0.336	0.310	0.276	>0.3
	N _D (kc)	>20.0	42.0	25.0	24.0	>90.0	>90.0	49.0	20.0	13.0	>90.0	65.0	22.0	13.0	9.3	>16.0
	$\Delta a - \Delta a_{OL}$ (mm)	-	0.171	0.126	0.130	-	-	0.244	0.214	0.181	-	0.230	0.244	0.214	0.180	0.22 - 0.35
	avg. da/dN following OL ($\times 10^{-8}$ m/cy)	-	0.41	0.50	0.54	-	-	0.50	1.1	1.4	-	0.35	1.1	1.6	1.9	1.1 - 2.1

1. If results are presented as an inequality, the computation was stopped at a preset number of cycles (usually 90,000); i.e., the model effectively predicts crack arrest.
2. The constraint factor for this case was 3.0 (plain strain) for all cycles except the overload cycle where the constraint factor was computed to be 1.68.

crack growth rate following the overload which is the quantity $\Delta a - \Delta a_{OL}$ divided by N_D .

B2. Residual Stresses Predicted Before, During and After the Overload/Underload Event

B2.1 Experimental 1: OLR* = 2.15, R = 0.1

Stresses computed by the model are shown before, during and after the overload cycle in Fig. B1. These results are independent of the crack growth rate curve used (except for the number of cycles), but depend on ΔK and the overload ratio used, as well as the constraint factor ($\alpha = 1.9$).

The magnitude of stress at maximum load (solid line) is equal to the constraint factor times the flow stress, while the magnitude of residual stress at minimum load (broken line) is limited to the unconstrained flow stress. Elastic stresses are not plotted, but return to average applied stress in a manner proportional to the square root of the distance from the crack tip. The stair step appearance of the stress is due to the division of distance into discrete elements. Stress is shown as constant for the width of each element.

Prior to the overload, Fig. B1a, the extent of the residual stresses at minimum load is small compared to that on the overload cycle, Fig. B1b. Ten cycles after overload, Fig. B1c, the residual stress fields at both maximum and minimum load have been modified considerably, as compared to the zone prior to overload, in that there is now a region of minimum tensile stress within the plastic zone at maximum load. Also, the extent of residual stress in the crack wake at minimum load has been diminished, compared to that prior to the overload.

The crack is seen to have grown into the plastic zone of the overload 3513 cycles later, Fig. B1d. This is near the point of minimum growth rate. Stress at both maximum and minimum load has been considerably altered, and there is again residual stress in the crack wake at minimum load. Residual stress ahead of the crack at minimum load is seen to be tensile, as compared to compressive before the overload.

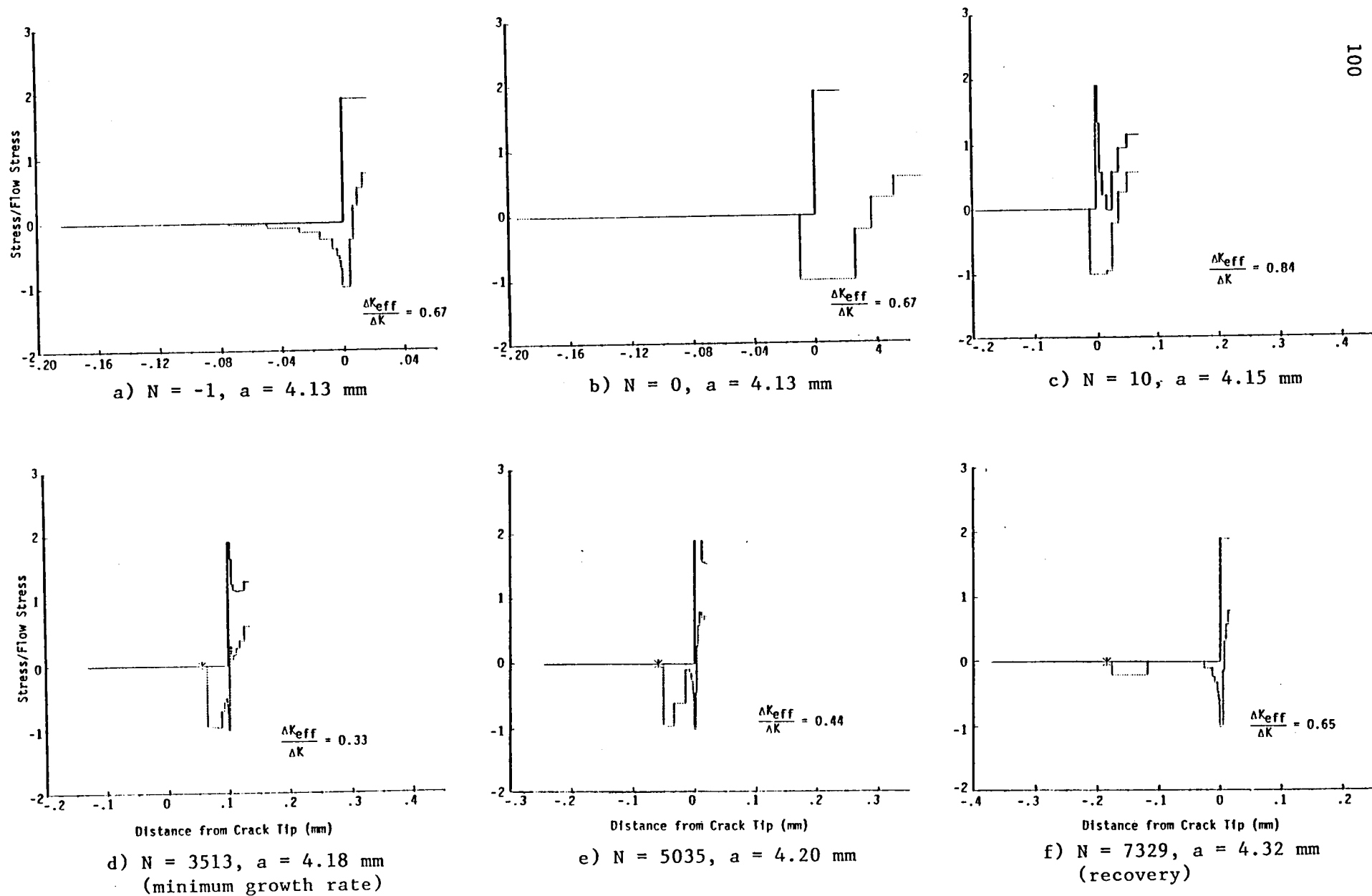


Figure B1. Predicted crack-tip stress distributions and crack closure levels for cycles (N) before, during ($N=0$), and after the overload in Experiment 1 at $\Delta K = 7 \text{ MPa}\sqrt{\text{m}}$, $R = 0.1$, $OLR^* = 2.15$. Curves correspond to maximum (—) and minimum (---) applied load. Predictions for $\alpha = 1.9$ for all cycles.

At 5035 cycles, the condition is altered, Fig. B1e, but not appreciably, over that at 3513 cycles, but the crack has grown only about 0.1 mm. However, after 7329 cycles, Fig. B1f, considerable crack growth has occurred, and the residual stress patterns at both maximum and minimum loads have come to look more like those before application of the overload. In addition, there is now a small region of compressive residual stress in the crack wake just ahead of the spot where the overload was applied.

B2.2 Experiment 3: OLR* = 3.0, ULR* = 2.0, R = 0.5

Comparison of Fig. B2a, one cycle prior to overload, with the same condition at $R = 0.1$, Fig. B1a, shows that there is significantly less residual stress in the crack wake at minimum load for this high R . Note that a constraint factor of 3 is being used in this case, as compared to the 1.9 used for Experiment 1.

The overload followed by underload results in a large zone of residual stress at minimum load which extends both ahead and behind the crack tip. The residual stress zone is much larger for this experiment than for Experiment 1, even though the maximum load is about the same, because the crack is over twice as long. Note that the constraint factor has also changed for this cycle from 3 to 1 (see Fig. B2b).

Two cycles after the overload/underload, the crack has advanced approximately 0.1 mm, Fig. B2c. Although the residual stresses are similar to those of Experiment 1, Fig. B1c, their extent is considerably greater.

After 1940 cycles, Fig. B2d, near the point of minimum growth rate, a considerable wake of residual stress has developed and only a small region of compressive residual stresses has developed at the crack tip at minimum load, in clear contrast with the result of Fig. B1d.

After 2600 cycles, the growth rate has nearly recovered to that prior to the overload and the residual stress field is also similar, Fig. B2f.

B2.3 Experiment 4: OLR* = 3.0, R = 0.5

Computed residual stress distributions for this case are shown in Fig. B3. Prior to application of the overload, the residual stress distribution is

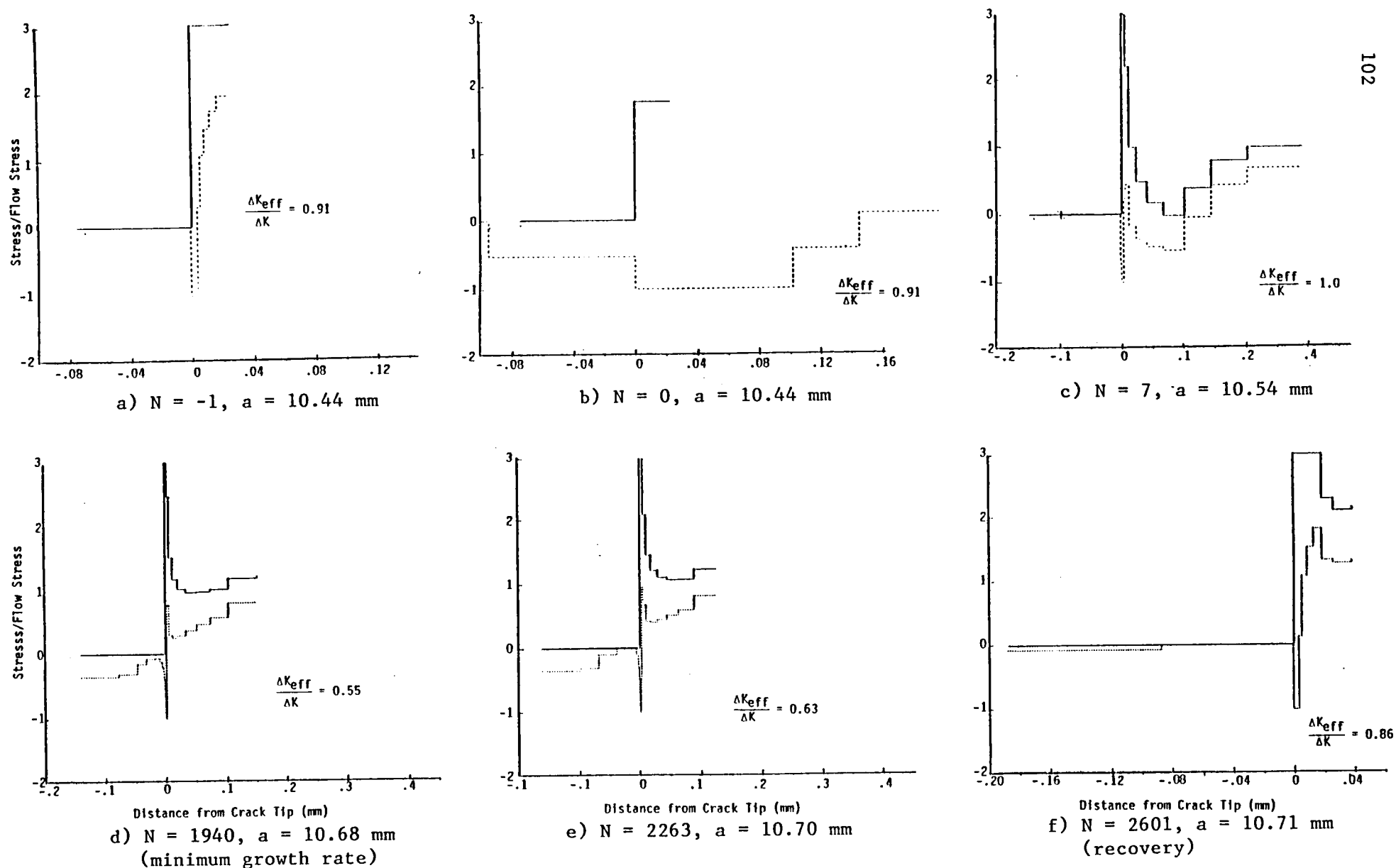


Figure B2. Predicted crack-tip stress distributions and crack closure levels for cycles (N) before, during ($N=0$), and after the overload and underload in Experiment 3 at $\Delta K = 7 \text{ MPa}\sqrt{\text{m}}$, $R = 0.5$, $OLR^* = 3.0$, $ULR^* = 2.0$. Curves correspond to maximum (—) and minimum (---) applied load. Predictions for $\alpha = 3$, except during the overload where $\alpha = 1.75$.

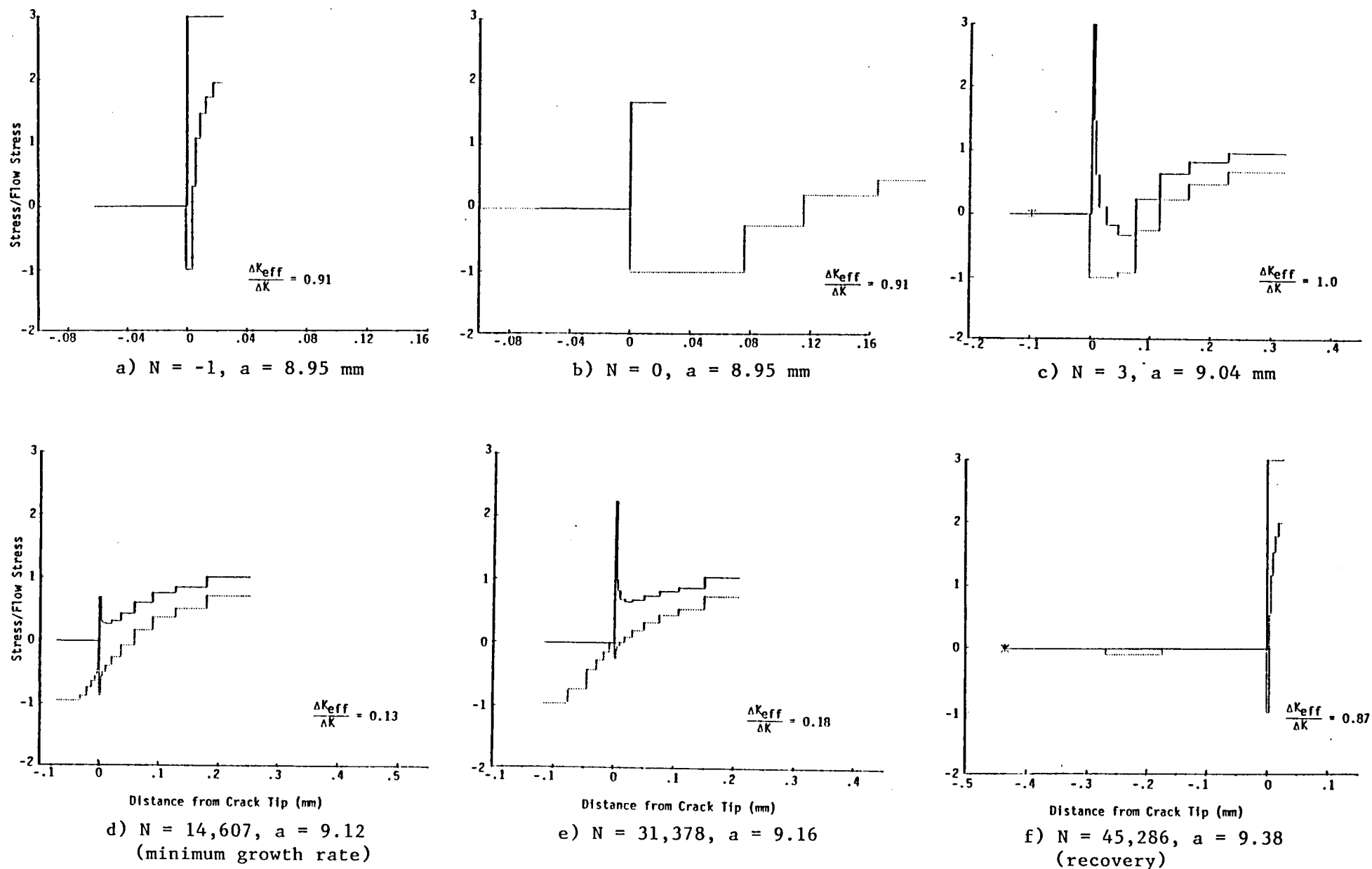


Figure B3. Predicted crack-tip stress distributions and crack closure levels for cycles (N) before, during ($N=0$), and after the overload in Experiment 4 at $\Delta K = 7 \text{ MPa}\sqrt{\text{m}}$, $R = 0.5$, $OLR^* = 3.0$. Curves correspond to maximum (—) and minimum (---) applied load. Predictions are for $\alpha = 3$, except during the overload where $\alpha = 1.68$.

similar to those for Experiment 3, which was at the same R. Residual stress after the overload cycle is also similar to that of Experiment 3, Fig. B2b, but the extent of the stresses is greater and there is no residual stress in the wake as there was when the overload was followed by an underload.

Three cycles after the overload, the residual stress distribution is as shown in Fig. B3c, which is considerably different than that shown in Fig. B2c, in that the residual stress is always negative ahead of the crack tip, rather than having a positive component.

After 14,600 cycles, the crack has grown well into the zone of residual stress and residual stress in the wake has developed, Fig. B3d. This is near the point of minimum growth rate. At 31,378 cycles after the overload, Fig. B3e, the maximum stress has increased considerably, compared to that in Fig. B3d. At 45,286 cycles, the growth rate has nearly returned to that previous to the overload, and so has the stress distribution, Fig. B3f.

NASA Contractor Report 172597
Distribution List
NAS1-17641

	<u>No.</u> <u>Copies</u>
NASA Langley Research Center Hampton, VA 23665 Attn: 151A/Research Information Office 188E/Dr. J. C. Newman, Jr.	2 15
NASA Ames Research Center Attn: Library, Mail Stop 202-3 Moffett Field, CA 94035	1
NASA Dryden Flight Research Facility Attn: Library P. O. Box 273 Edwards, CA 93523	1
NASA Goddard Space Flight Center Attn: Library Greenbelt, MD 20771	1
NASA Lyndon B. Johnson Space Center Attn: JM2/Technical Library 2101 Webster Seabrook Road Houston, TX 77058	1
NASA Marshall Space Flight Center Attn: Library, Mail Stop AS24L Marshall Space Flight Center, AL 35812	1
Jet Propulsion Laboratory Attn: 111-113/Library 4800 Oak Grove Drive Pasadena, CA 91103	1
NASA Lewis Research Center Attn: Library, Mail Stop 60-3 21000 Brookpark Road Cleveland, OH 44135	1
NASA John F. Kennedy Space Center Attn: Library, NWSI-D Kennedy Space Center, FL 32899	1
National Aeronautics and Space Administration Attn: RM Washington, DC 20546	1
NASA Scientific and Technical Information Facility 6571 Elkridge Landing Road Linthicum Heights, MD 21090	

24 plus original

1. Report No. NASA CR-172597		2. Government Accession No.		3. Recipient's Catalog No.	
4. Title and Subtitle Measurement and Analysis of Critical Crack Tip Processes During Fatigue Crack Growth				5. Report Date June 1985	
				6. Performing Organization Code	
7. Author(s) D. L. Davidson, S. J. Hudak, Jr: and R. J. Dexter				8. Performing Organization Report No.	
9. Performing Organization Name and Address Southwest Research Institute 6220 Culebra Road San Antonio, TX 78284				10. Work Unit No.	
				11. Contract or Grant No. NAS1-17641	
12. Sponsoring Agency Name and Address National Aeronautics and Space Administration Washington, DC. 20546				13. Type of Report and Period Covered Contractor Report	
				14. Sponsoring Agency Code 505-33-23-02	
15. Supplementary Notes Langley Technical Monitor: J. C. Newman, Jr. Final Report					
16. Abstract This report summarizes work conducted over the past year designed to examine the mechanics of fatigue crack growth under constant-amplitude and variable-amplitude loading. In the latter case, critical loading histories involving relatively simple overload and overload/underload cycles were studied in order to provide a basic understanding of the underlying physical processes controlling crack growth. The material used for this study was 7091-T7E69, a powder metallurgy aluminum alloy. Extensive measurements of local crack-tip parameters have been made at various times before, during, and after the overloads--these include crack-tip opening loads and displacements, as well as crack-tip strain fields. The latter were used, in combination with the materials cyclic and monotonic stress-strain properties, to compute crack-tip residual stresses. The experimental results were also compared with analytical predictions obtained using the FAST-2 computer code. A study of the sensitivity of the analytical model to constant-amplitude fatigue crack growth rate properties and to through-thickness constraint was also conducted.					
17. Key Words (Suggested by Author(s)) variable amplitude fatigue, overload effects, crack closure, residual stress, aluminum alloys			18. Distribution Statement Unclassified - Unlimited Subject Category 39		
19. Security Classif. (of this report) Unclassified		20. Security Classif. (of this page) Unclassified		21. No. of Pages 112	
22. Price*					

